SYNTHESIS OF LAYERED NANOSHEETS AND THEIR APPLICATION IN FLEXIBLE NANOGENERATORS

YANG FUMEI

PhD

The Hong Kong Polytechnic University

2025

The Hong Kong Polytechnic University

The Department of Applied Physics

Synthesis of Layered Nanosheets and Their Application in Flexible Nanogenerators

YANG Fumei

A thesis submitted in partial fulfilment of the requirements for the degree of Doctor of Philosophy

August 2024

CERTIFICATE OF ORIGINALITY

I hereby declare that this thesis is my own work and that, to the best of my knowledge and belief, it reproduces no material previously published or written, nor material that has been accepted for the award of any other degree or diploma, except where due acknowledgement has been made in the text.

_____(Signed)

YANG Fumei (Name of Student)

Life is short and Art is long;

opportunity fleeting,

experiment treacherous,

judgment difficult.

—— *Hippocrates*

Abstract

Flexible nanogenerators capable of efficiently converting mechanical energy into electricity have diverse applications in communication, healthcare, environmental monitoring and beyond. Since the first discovery of piezoelectricity in quartz, conventional piezoelectric crystals such as lead zirconate titanate (PZT) and barium titanate (BTO) have attracted great interest due to their exceptional electromechanical conversion efficiency. Unfortunately, these ceramics suffer from vulnerability in flexibility and biocompatibility for advanced consumer electronics such as wearable and bio-implantable devices. Recently, layered materials have emerged as the promising candidates for flexible electronics due to their ultrathin nature, desirable electrical and mechanical properties, and attractive biocompatibility. To date, various layered materials, including hexagonal boron nitride (h-BN), transition metal chalcogenides (TMDs), and group III-IV metal chalcogenides, have been applied in developing flexible nanogenerators, but the intrinsic piezoelectricity generally only exists in the monolayer or few-odd layers due to the polarization cancellation between adjacent layers, leading to low output signals and poor mechanical stability. While extensive designs like Janus structures were proposed to enhance the performance by inducing higher symmetry breaking, the complexity and uncontrollability of these designs limit their broad practical applications. In contrast, novel multi-layer piezoelectric materials show great potential in achieving considerable output

performance and long-term durability for practical applications. Furthermore, the scalability of these layered materials is highly desired for facilitating the widespread practical applications.

This thesis delves into the synthesis of novel multi-layer nanosheets, including strong-piezoresponse layered SnSe and high-entropy MXene, and their application in advanced flexible nanogenerators. Firstly, SnSe nanosheets were synthesized using bottom-up vapor transport deposition (VTD). By fine-tailoring the specific growth parameters, such as the growth temperature, growth duration, carrier gas and so on, the resulting SnSe nanosheets on mica substrates exhibit large area, homogeneous surface and high crystalline quality, confirmed by systematically morphological and structural characterization. In addition, the enhanced in-plane piezoelectric properties of SnSe nanosheets with varying thickness is evidenced through piezoresponse force microscope (PFM), which attributes to their unique puckered C_{2v} symmetry. Specifically, effective piezoelectric coefficient in 10 nm SnSe nanosheet (d_{11} = ~ 45.82 pm/V) surpassed those in most investigated TMDs with odd-even effects, showing great potential for practical flexible-nanogenerator applications. The electrical properties of SnSe nanosheets were also investigated by fabricating field-effect-gating devices, displaying the clear p-type transfer behavior with a considerable hole mobility of 19.35 $cm^2\ V^{-1}\ s^{-1}$. On these bases, the SnSe nanosheets were further developed into flexible PENG device, exhibiting distinct piezotronic effect, high energy conversion efficiency and sensibility in energy harvesting and human-motion monitoring, suggesting their

capability for smart wearable electronics and healthcare applications. In addition to VTD technique, top-down electrochemical etching approach is also employed for high-yield synthesis of layered nanosheets, and the target material here is the high-entropy MXene ($TiVCrMoC_3T_x$). Different from the commonly used hydrofluoric acid (HF)-etching method, electrochemical etching can produce MXene with low bio-toxicity, which is very suitable for the future development of biocompatible devices. Flexible nanogenerators were further fabricated based on a composite structure of high-entropy MXene nanosheets with PVA polymer relying on a direct self-assembly path. The output performance of MXene/PVA self-powered flexible nanogenerators reaches up to 500 mV in voltage and 790 pA in current at 3.47 N, with stable working over 1,500 cycles, indicating the desirable mechanical durability and potential for practical applications in wearable and bio-implantable electronics.

In summary, this thesis explores the synthesis of high-quality SnSe and MXene layered nanosheets with high yield and further develops their applications in innovative flexible nanogenerators and sensors. These findings drive the exploration of novel multi-layer materials for the advancement of next-generation electronic devices with attractive high-performance, satisfying energy-efficiency, and desirable flexibility and functionality across diverse applications and industries.

Acknowledgements

My deepest gratitude to my supervisor, Prof. Jianhua Hao, for his generous guidance, continuous encouragement and positive support throughout my PhD study at PolyU. His mentorship has not only enriched my research pursuits but has also nurtured my personal growth. I deeply admired his great enthusiasm and insightful thinking in scientific research, which enrich my research journey and will continue to resonate in my future pursuits.

I would like to express my appreciation to my groupmates and friends: Dr. WONG Man Chung, Dr. WU Zehan, Dr. MAO Jianfeng, Ms. ZHAO Fangqing, Dr. PANG Sin Yi, Dr. DING Ran, Dr. WEI Yi, Dr. GUO Feng, Dr. SONG Menglin, Dr. HAN Xiao, Dr. HAN Xun, Ms. IO Weng Fu, Mr. CHAN Kam Lin, Dr. LI Lihua, Ms. MA Yingjin, Mr. ZHAO Yifei, Dr. ZHAO Di, Dr. BAI Qianqian, Ms. LAO Xinyue, Mr. LIU Yuan, Ms. DANG Zhaoying, Ms. LI Liuting, Dr. CUI Qilong, Dr. LIAO Fuyou, Ms. PENG Zifang, Dr. WU Qing, Ms. CHEN Hongye, Mr. YAN Jianming, Dr. LIU Hong, Ms. LIU Yuhui, Mr. XIAO Yiping, Ms. WANG Cong, Mr. CHEN Ziling, Mr. CHEN Haiquan, Mr. WANG Fei, Ms. DONG Dan, Ms. WANG Jing, Ms. TIAN Hui, Ms. XU Shiyao, Ms. FENG Lu, for their helpful assistance, sincere company and close support in my study and life.

Finally, my heartfelt gratitude extends to my beloved family for continuous backing, careful attention, and devoted encouragement in all aspects of my life.

Publication

Fumei Yang, Man-Chung Wong, Jianfeng Mao, Zehan Wu, and Jianhua Hao*. Synthesis and enhanced piezoelectric response of CVD-grown SnSe layered nanosheets for flexible nanogenerators. Nano Research 2023, 16(9): 11839-11845.

Fumei Yang, Kam Lin Chan, Zehan Wu, Fangqing Zhao, Man Chung Wong, Sin-Yi Pang, and Jianhua Hao*. HF-free synthesis of high-entropy MXene-PVA composite film and its flexible nanogenerator. Submitted to Science China Materials, under revision, 2025.

Zehan Wu, Ke Yang, Wanqing Meng, Weizhen Wang, Yifei Zhao, **Fumei Yang**, Ran Ding, Hui Li, Songhua Cai, Ming Yang, Jiannong Wang, Lain-Jong Li*, and Jianhua Hao*. High-performance tunnel FETs exhibiting boosted sub-Boltzmann-limit ON-current up to 10 μA/μm. Under revision, 2025.

Zehan Wu, Yifei Zhao, **Fumei Yang**, and Jianhua Hao*. Device physics and architecture advance in tunnel field-effect transistors. Submitted to Interdisciplinary Materials, 2025.

Fangqing Zhao, Guanding Mei, Fankai Zheng, **Fumei Yang**, Weixiong Peng, Depeng Li, Yangzhi Tan, Jingrui Ma, Xiangwei Qu, Xiao Wei Sun*, Jianhua Hao*, and Kai Wang*. Optical tunneling scheme under low SPP microcavities for eco-friendly blue ZnSe QLEDs. To be submitted.

Table of Contents

List of Figures

List of Tables

List of abbreviations

2D Two-dimensional

AC Alternating current

AFM Atomic force microscopy

BTO Barium titanate

CCD Charge-coupled device

CVD Chemical vapor deposition

DI water deionized water

DMSO Dimethylsulfoxide

EDX Energy-dispersive X-ray spectroscopy

FET Field-effect transistors

h-BN Hexagonal boron nitride

HF Hydrofluoric acid

HRTEM High-resolution transmission electron microscopy

MBE Molecular beam epitaxy

MXene Transition metal carbide/nitride

-OH Hydroxyl

PENG Piezoelectric nanogenerator

PFM Piezoresponse force microscopy

PI Polyimide

PMMA Poly(methyl methacrylate)

PMT Photo multiplier tube spectrometer

PVA Polyvinyl alcohol

PVD Physical vapor deposition

PZT Lead zirconate titanate

SAED Selected area electron diffraction

sccm Standard cubic centimeters per minute

SEM Scanning electron microscope

SHG Second harmonic generation

TEM Transmission electron microscopy

TMAOH Tetramethylammonium hydroxide

TMDs Transition metal dichalcogenides

vDW Van der Waals

VTD Vapor transport deposition

XRD X-ray diffraction

Chapter 1 Introduction

1.1 Background of layered materials

1.1.1 Graphene and h-BN

The discovery of graphene by mechanically exfoliation from graphite two decades ago blooms the exploration of 2D layered materials.[1] They consist of atomically-thin nanosheets with robust in-plane bonding and weak coupling between interlayer and layer-substrate. Attributable to the intriguing electrical, optical, thermal and mechanical characteristics, many layered materials, such as graphene, hexagonal boron nitride (h-BN), transition-metal dichalcogenides (TMDs) and beyond, have been widely studied for various applications.

Graphene is a single layer of carbon atoms structured within a honeycomb matrix. As shown in Figure 1.1, various other-dimensional graphite materials can be constructed based on this building block, including zero-dimensional fullerenes, one-dimensional nanotubes, or three-dimensional layers-stacked graphite.[2] The carbon atoms of graphene form strong in-plane σ bonds and out-of-plane delocalized π bonds due to sp^2 hybridization. Notably, graphene possesses an extremely unique electronic structure, which is characterized by Dirac cones at the corners of the Brillouin zone. As a result, this characteristic leads to massless Dirac fermions, which indicates that the delocalized π electrons in graphene can move freely without scattering across the entire structure.[3] As depicted in Figure 1.2, the Brillouin zone has six vertices (known as Dirac

points or **K** points), with the conduction as well as valence bands symmetrically centered around the Dirac points, where the band structure and wave vector exhibit a linear relationship.[4] This unique band structure results in remarkable properties, such as giant carrier mobility of more than 10^4 cm^2 V^{-1} s^{-1},[1, 5] outstanding thermal conductivity (with a thermal conductivity coefficient of up to 5300 W/mK),[6] excellent optical characteristics (with an broadband absorption rate of ~2.3%, and ~80% transparency in appearance);[7-9] and exceptionally high mechanical strength (with an elastic modulus of up to 1 TPa).[10] Moreover, the weak van der Waals (vdWs) interaction between two neighboring graphene nanosheets is facilitated by π-bonds, enabling for layer exfoliation and reconstruction for fundamental research and further nanotechnology applications.

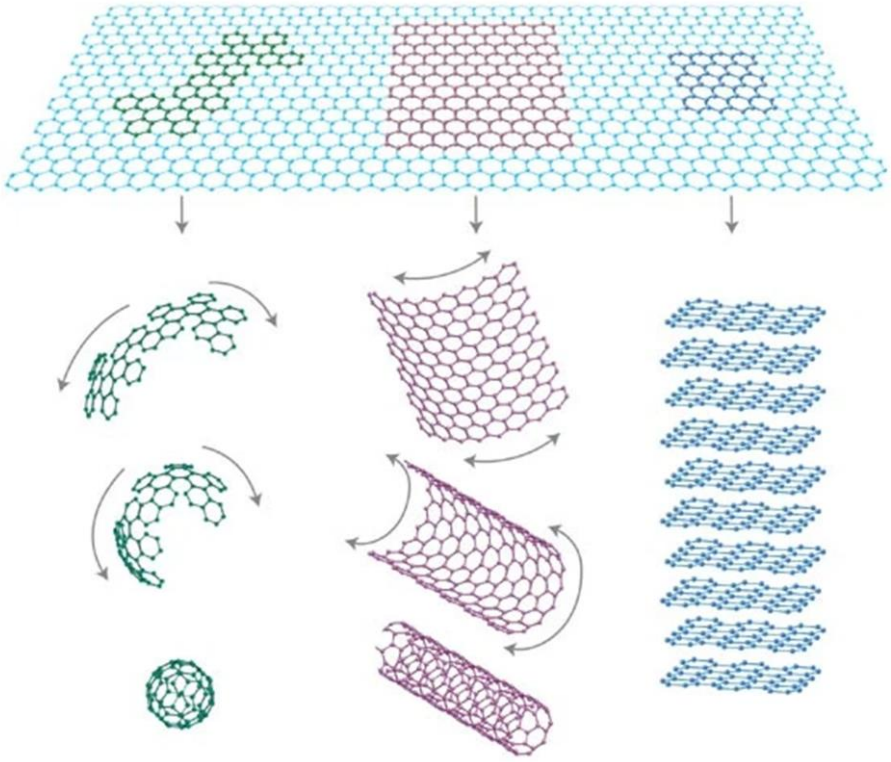

Figure 1.1 Different graphitic forms: fullerenes, nanotubes and graphite.[2]

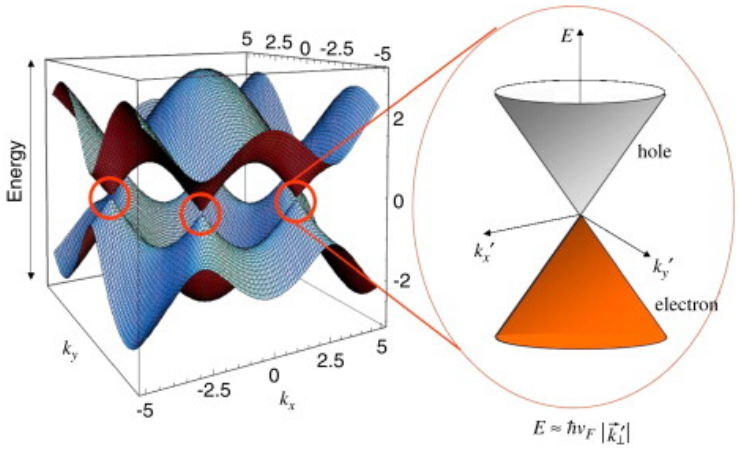

Figure 1.2 Band structure of graphene. The energy E is shown as a function of the Bloch wavevector (k_x, k_y), as demonstrated in the zoom of the energy band close to a Dirac point **K′**. There is a linear dispersion relation: $E \approx \hbar v_F \left|\vec{k}_\perp'\right|$, where $\hbar$ denotes the reduced Planck constant, v_F is Fermi velocity (1/300 of light velocity), and k represents the wave vector, respectively.[4, 11]

Although graphene exhibits numerous exceptional properties and offers the potential for discovering low-dimensional physics and fabricating next-generation electronic devices, its intrinsic zero-bandgap electronic structure significantly limits its practical applications. In addition to engineering the electronic properties of graphene (such as strain, defect and stacking configuration),[12] various emerging layered materials have been explored to address the shortcomings of graphene, such as h-BN, the bandgap-tunable elemental semiconductor materials (e.g. black phosphorus (BP) and TMDs), as shown in Figure 1.3. The h-BN, consisting of alternating boron and nitrogen atoms analog to the structure of graphene, has a wide bandgap of ~6.0 eV, making it an excellent electrical insulator.[13, 14] Its dielectric constant shifts from 3.29 for monolayer

to 3.76 for bulk h-BN (comparable to that of SiO_2). This property makes it suitable for use as substrate material and gate dielectric, potentially replacing SiO_2. It facilitates high carrier mobility in layered channel materials owing to its smooth surface devoid of dangling bonds and charge traps.[15] Moreover, h-BN can function as a tunneling barrier and can be incorporated into tunneling devices such as tunnel diodes or tunnel field-effect transistors (FETs) to control electron transport through the barrier via quantum tunneling effects.[16]

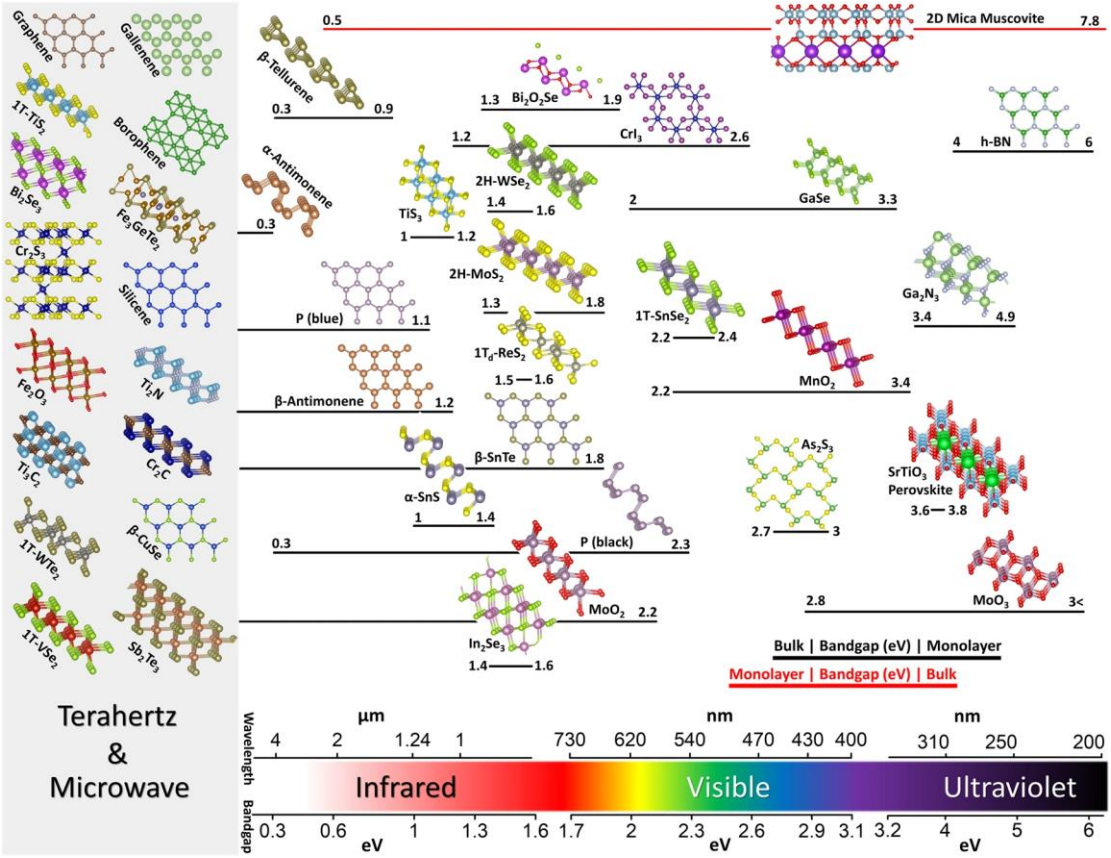

Figure 1.3 Bandgaps in layered materials family.[17]

1.1.2 Elemental layered materials in group VA and transition metal dichalcogenides

In the VA group, except for nitrogen, all other elements exhibit layered crystal structures, such as black phosphorus, gray arsenene, antimonene and bismuthene. As

depicted in Figure 1.4, two typical structures of elemental semiconductor materials in this group are demonstrated. The α-phase (Figure 1.4a) exhibits distinctive puckered interlayer, resulting in a low symmetry in an orthorhombic crystal system. On the other hand, the crystal structure of β-phase (Figure 1.4b) resembles the buckled structure similar to graphene. In the bulk material of group VA, black phosphorus stabilizes in the α phase, while other elements are stable in the β-phase structure. Among them, BP has garnered significant attention as an outstanding layered material since the first few-layer BP based p-type FET with a high mobility of up to 10^3 cm^2 V^{-1} s^{-1} and a drain current modulation of 10^5.[18] Its direct bandgap shows layer-dependent characteristic, from~2 eV for a monolayer, gradually down to ~0.3eV for bulk BP.[18, 19] Additionally, its highly in-plane anisotropy has led to widespread applications.[20] However, BP suffers from a vulnerability limitation: it is highly susceptible to oxidation in ambient conditions, leading to performance degradation, which restricts the practical optoelectronic applications in long-term working.[21]

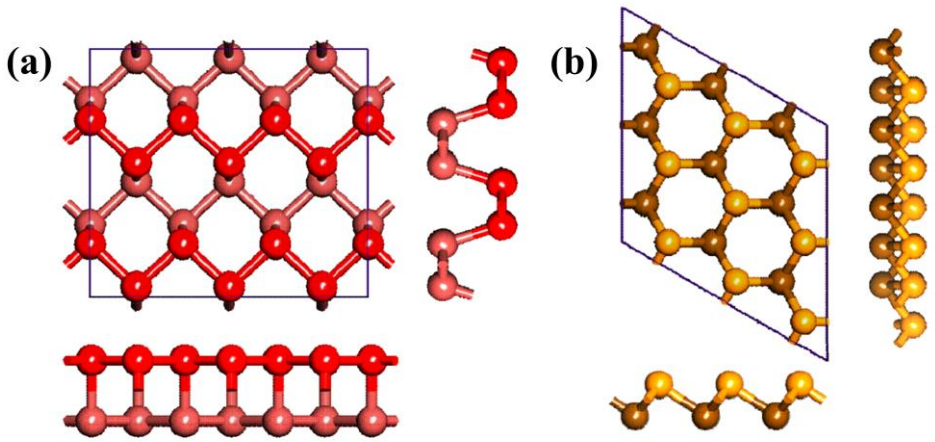

Figure 1.4 Two typical crystal structures of elemental semiconductors in Group VA.[22] (a) α-phase (orthorhombic). (b) β-phase (rhombohedral).

Another typical class of bandgap-tunable materials is transition metal dichalcogenides (TMDs) with the chemical composition of MX_2, where M represents transition metal elements from Group IV (such as Ti, Zr, or Hf), Group V (such as V, Nb, or Ta), or Group VI (such as Mo or W); and X denotes chalcogen elements (S, Se, or Te). The monolayer consists of three stacked layers (X-M-X), involving double layers of hexagonal chalcogen atoms covalently bonded with one layer of metal atoms. Few-layer or bulk TMDs are arranged by weak vdWs. There are three common crystal structures in TMDs: 2H, 1T, and 1T′ (Figure 1.5a). In the 2H crystal structure, transition metals coordinate in a trigonal prismatic manner, with two layered units rotated by 60°, resulting in a hexagonal symmetry within a unit cell containing two layered units (ABA stacking). In contrast, the 1T structure features transition metals coordinating in an octahedral manner, with one layered unit per unit cell, exhibiting trigonal symmetry (ABC stacking). Besides, 1T′ could be achieved by the distortion of 1T phase structure.[23] Different structures typically lead to distinct properties: The physical properties of this group varies from metallic, semi-metallic, semiconducting to even insulating characteristics according to their electronic band structures; The bandgap of MoS_2 shift from 1 eV for bulk to ~2 eV for the monolayer, with a transition from indirect to direct bandgap (Figure 1.5b); Compared to the anisotropic 2H MoS_2, the 1T ReS_2 and $ReSe_2$ displays significant in-plane anisotropy.[24-26] The rich electronic properties of TMDs offer opportunities for various applications such as optoelectronics, sensing and beyond. The different stacking patterns also increase the flexibility for

exploring more unique properties of TMDs.

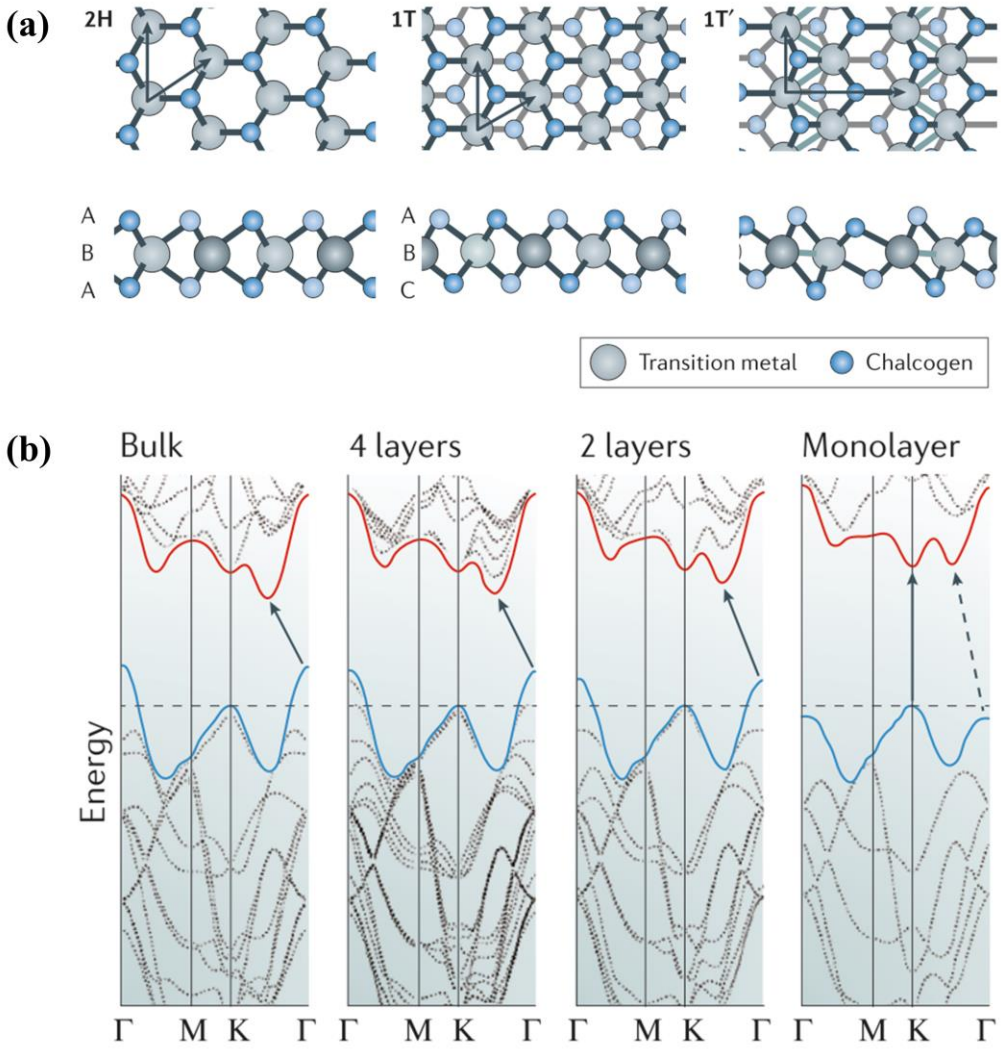

Figure 1.5 crystal structures and band structures of TMDs. (a) Lattice structures of TMDs in the trigonal prismatic (2H), octahedral (1T), and distorted (1T′) phases. The different stacking configurations lead to different lattice structures. Here, A, C denotes chalcogen elements and B denotes transition metal. (b) Band structures of MoS_2 from bulk to monolayer.[23, 25]

1.1.3 MXenes, group III-VI and group IV-VI metal chalcogenides

In recent years, many other classes of layered materials have been investigated to

widen the horizon in the 2D family, including metal carbides and nitrides (MXenes), Group III-VI and Group IV-VI metal chalcogenides.

MXenes are generally etched from their counterpart MAX phases. They could be expressed as $M_{n+1}X_nT_x$, where M represents a transition metal component from groups IV, V, or VI, X is carbon and/or nitrogen, T_x denotes the surface functional groups or terminations (such as hydroxyl (-OH), fluoride (-F), or oxygen (-O)), n is the number of transition metal layers sandwiched between double X layers. Figure 1.6 depicts the structure of MXene, showing that the M atoms are sandwiched between two layers of X atoms and the outer layer is terminated with the surface groups.[27] MXene materials exhibit exceptional electrical properties, mechanical superiority, as well as chemical stability, which are key factors in their utility for various technological advancements. Furthermore, layered MXenes possess a high surface area, facilitating for energy-storage applications like super capacitors and batteries.[28, 29] Their catalytic properties have shown promise in reactions like water splitting and CO_2 reduction.[30] Additionally, MXenes are being explored in flexible electronics and sensing applications owing to their unique mechanical and electrical properties.[31]

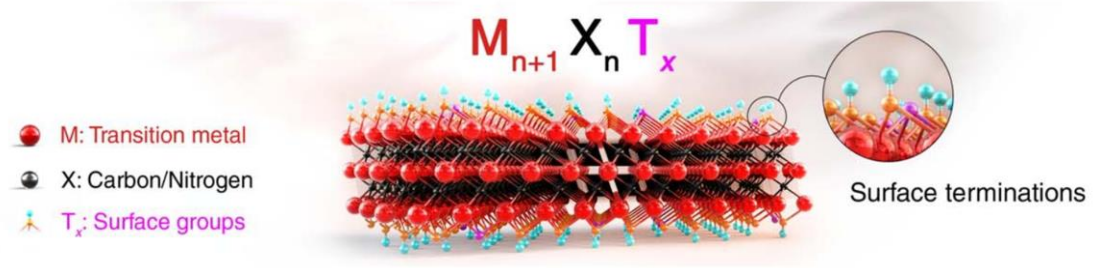

Figure 1.6 The atomic structure of MXene.[27]

In group III-VI, indium and gallium chalcogenides have used for broad applications in electronics and optoelectronics by virtue of unique exceptional properties, including direct band gap, high carrier mobility and robust light-matter interactions.[29, 32] They have two common formulas: MX and M_2X_3, where M is In or Ga, X is S, Se or Te. The typical structure in this group is depicted in Figure 1.7a-b, showing a hexagonal (such as GaS and InSe) and monoclinic lattice (such as GaTe and InTe). There are diverse polymorphs in the multilayer hexagonal structure, as demonstrated in Figure 1.7c, including β, γ, δ, and ε phases with 2H, 3R, 4H and 2H stacking, respectively. The various configurations contribute to different symmetry properties, which will exhibit intriguing electrical properties and nonlinear optical properties for piezoelectric, ferroelectric and photonic applications.[33, 34] On the other hand, the diversity in structure also makes it complicate to synthesize the pure phase materials.[35] Moreover, the layered structure in group III-IV exhibit anisotropic properties, with different behaviors along the different directions.[36] The tunable nature of the interlayer interactions and the ability to manipulate the stacking sequence contribute to the rich variety of electronic, optical, and mechanical properties.

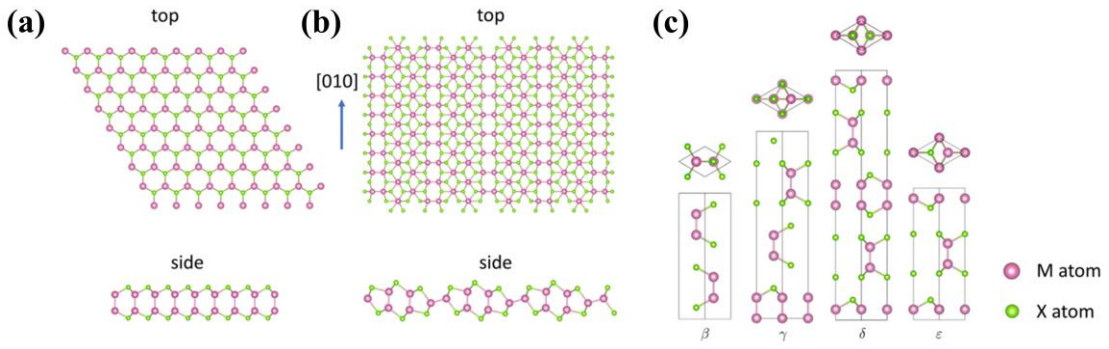

Figure 1.7 The Structure of group III–VI metal chalcogenides. (a) Hexagonal structure.

(b) Monoclinic structure. (c) The β, γ, δ, and ε phases of hexagonal structure.[37]

As an important class of layered materials, group IV-VI metal chalcogenides have also garnered much attention in recent years. These materials consist of stacked atomic layers where atoms from group IV elements (Ge or Sn) are bonded to atoms from group VI elements (S, Se or Te) in different lattice, typically including orthorhombic, hexagonal and monoclinic phases, as shown in Figure 1.8a-c. Their formula is MX or MX_2. In this group, MX compounds are p-type semiconductors, with both indirect and direct band gaps that are closely spaced in energy (Figure 1.8d-f, taking SnSe as an example). Specifically, the energy between the indirect and direct bandgaps of GeS is close, making it recognized as a direct bandgap material, while the others exhibit indirect bandgap. Due to their similar orbital composition and structural to that of BP, the orbitals forming the valence band maximum in MX are primarily non-bonding orbitals of the lone pair electrons under sp^3 hybridization of the two atoms. The electrons occupy the outmost orbital with a higher energy level compared to other bonding orbitals, facilitating hole doping and exhibiting p-type semiconductor characteristics in these materials.[38] Among layered materials family, few layered materials (such as WSe_2, BP and GaSe) and MX in this group IV-VI demonstrate intrinsic p-type behavior, while the other materials typically require complicate strategies to achieve n-p transition, such as interface engineering or chemical doping.[39, 40] Furthermore, similar to group III-VI materials, group IV-VI metal chalcogenides also exhibit unique anisotropic properties, allowing for exploring the diverse possibilities in

different orientations.[41]

Here, we will focus on SnSe in group IV-VI metal chalcogenides in this thesis. The structure of SnSe adopts an orthorhombic crystal system similar to BP (*Pnma* symmetry), and will experience phase transition to the higher asymmetry NaCl structure (*Cmcm* symmetry). The lower symmetry and lack of inversion center make it available for piezoelectric applications.[42] The electrical properties of SnSe will also investigated in this thesis.

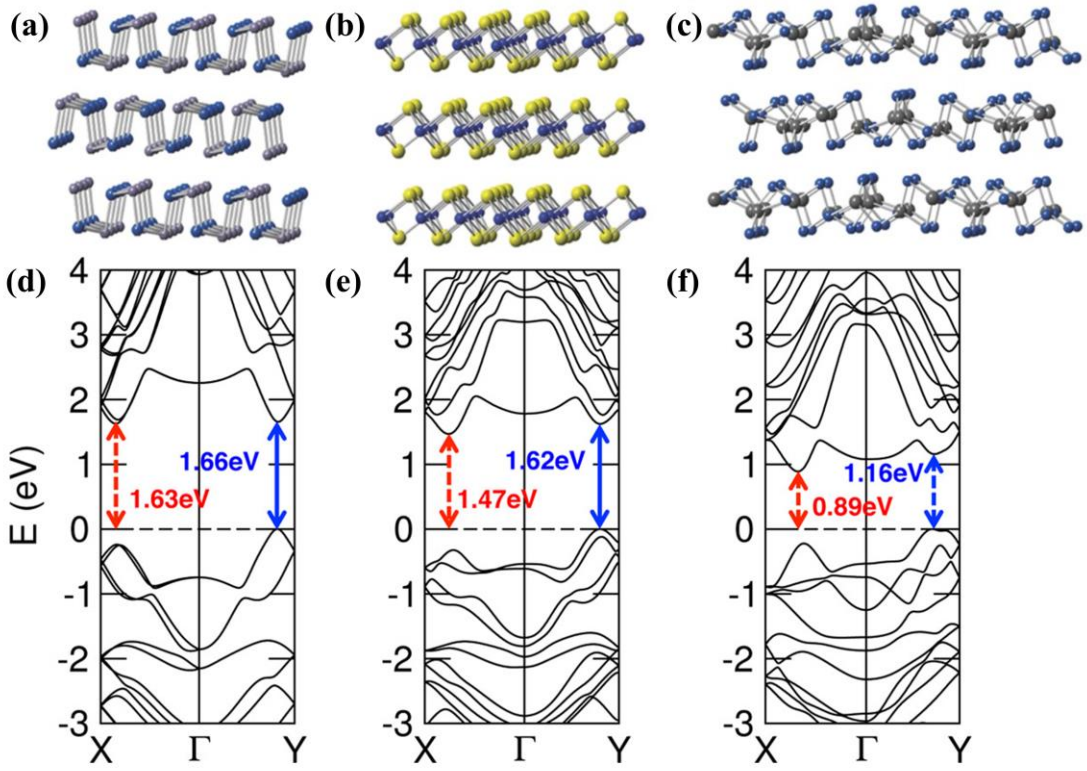

Figure 1.8 The layered structure and band structure of group IV-VI. They have three kinds of typical structures: (a) Orthorhombic, (b) hexagonal and (c) monoclinic phases. The band structures of monolayer (d), bilayer (e), and bulk (f) SnSe is demonstrated. The solid (blue) and dashed (red) arrows represents direct transitions and indirect transitions, respectively, with a small energy difference.[43]

1.2 Piezoelectric in layered materials

layered materials are required to meet some requirements to exhibit potential piezoelectricity. It was found that piezoelectricity only has the possibility in materials with non-centrosymmetric structure or a bandgap.[44, 45] Figure 1.9 demonstrates the two-dimensional monolayer structures that could exhibit piezoelectricity. These structures have a hexagonal or slightly distorted hexagonal lattice, resulting to the piezoelectric in the in-plane 11 direction, whereas the piezoelectric along the other directions could also exist based on their layered structure. For instant, the planer layer hexagonal and 2H hexagonal lattice structures only exhibit the non-zero d_{11}, while the buckled AB type layer has both non-zero d_{11} and d_{31}.[46] Piezoelectricity was investigated in different hexagonal structures, such as planar layer hexagonal lattice for semiconductor group III-VI and III-V in Figure 1.9a,[47] 2H hexagonal lattice for TMDs in Figure 1.9b[48] and buckled hexagonal lattice for some SC group (III-V) and (IV-MC) in Figure 1.9c.[49] The 2H hexagonal TMDs is stable in layered structure and bulk. However, their bulk is non-piezoelectric as the polarization between the adjacent is opposite and screened by each other, which indicates the piezoelectric effect is negligible for even multilayers.[44] As for zigzag edges nanoribbon layer hexagonal structure in SC group III-MC (Figure 1.9d), its intricate construction and the formation energy for each atom make it flexible in modifying the combination with X-M-M-X' or X-M-M'-X configuration, which can contribute to the enhancement for d_{11} or the appearance of the non-zero d_{31}.[50] In addition, the puckered hexagonal and rectangular lattice are also studied, as shown in

Figure 1.9e-f. Different phases with different formation energies could result in significant piezoelectric properties with different magnitude.[42, 51]

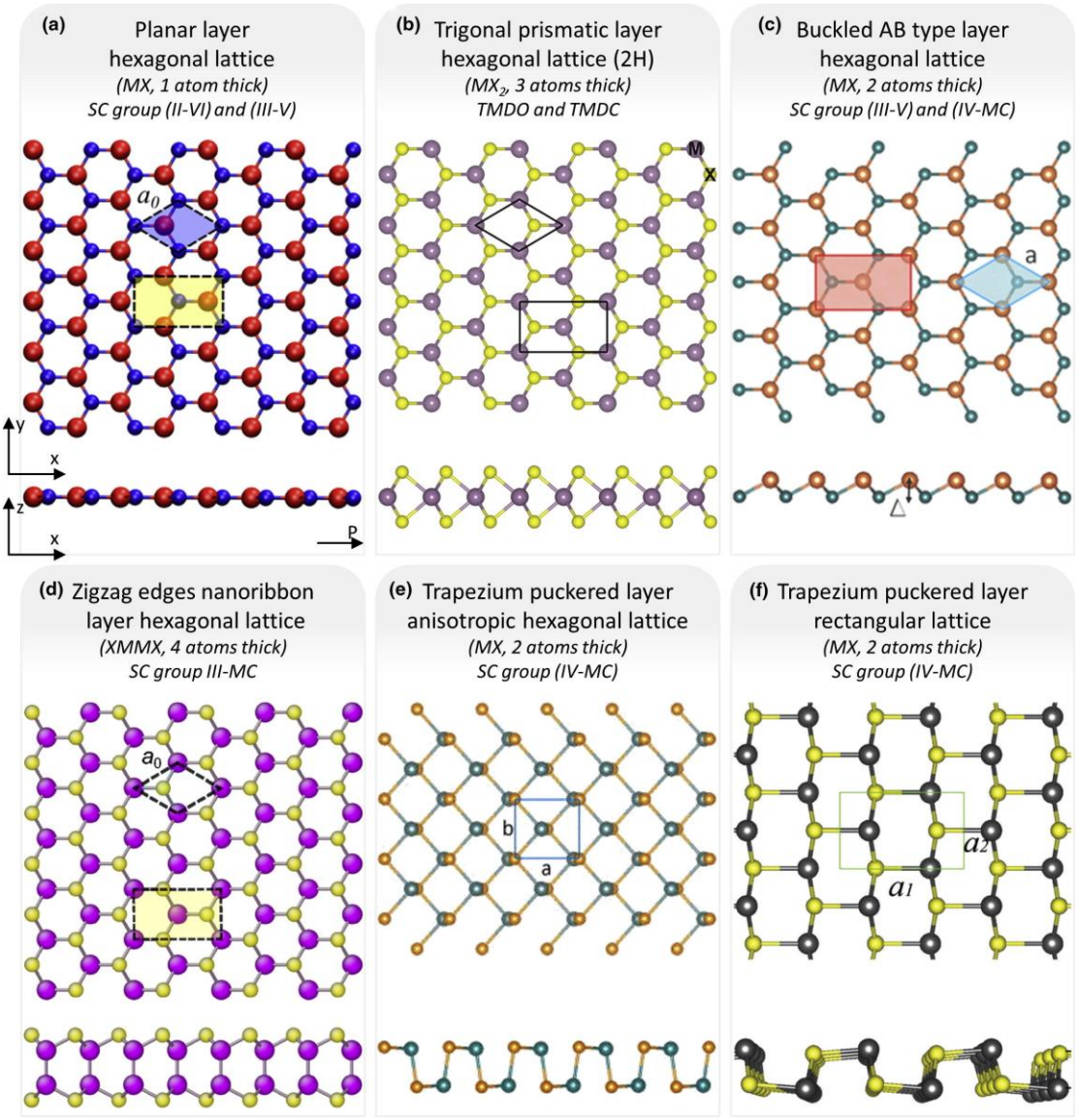

Figure 1.9 Several kinds of piezoelectric monolayer. (a) Planar hexagonal lattice. (b) Trigonal prismatic hexagonal lattice. (c) Buckled hexagonal lattice. (d) Nanoribbon hexagonal lattice. (e) Puckered anisotropic hexagonal lattice. (f) Puckered rectangular lattice.[52]

1.2.1 Intrinsic piezoelectricity

Since Wang and Zhang first demonstrated the piezoelectricity in single-layer MoS_2,[44, 53] various layered materials have been reported to exhibit piezoelectricity, including hBN, TMDs, group III-IV metal monochalcogenides. Different kinds of layered materials are also predicted to possess strong piezoelectric effects. The piezoelectric coefficient d_{11} of different groups of layered materials are predicted in Figure 1.10 and their piezoelectric properties follow some trends.[46] Taking the 2H-TMDs as an example (Figure 1.10a), their d_{11} are in direct proportion to the ratio between the polarizabilities of the isolated anion and cations, which indicates that the TMDs with larger anionic and smaller cationic polarizability could exhibit larger piezoelectric coefficients. Surprisingly, this similar relationship is appropriate for TMDs from the group V and VI. It was also found that the contributions from anionic and cationic polarization were opposite, which suggests that the former dominates the piezoelectric effect while the latter counteracts it.[46] This relationship also holds for most hexagonal group III-V materials except AlN, GaN and InN, as shown in Figure 1.10b. The d_{11} in this group is related to the ratio of the anion and cation polarizabilities, as well as the product of the Bader charge and lattice parameter, indicating both the change of the polarizabilities in two ions in response to the mechanical stimuli and the dislocation in the ions contribute to their piezoelectricity. Compared to the others, the high electronegativity and small dimension of N element may make those three different from others in this group.[46] The group IV monochalcogenides also has the similar periodic trends in TMDs and group III-V, as shown in Figure 1.10c. Within this

group, GeS exhibits the smallest d_{11} value, which increases when moving up in group 14 and group 16. On the other hand, SnSe showcases the highest coefficient at 250.58 pm/V, marking it as the anticipated highest in-plane piezoelectric coefficient to date.[42]

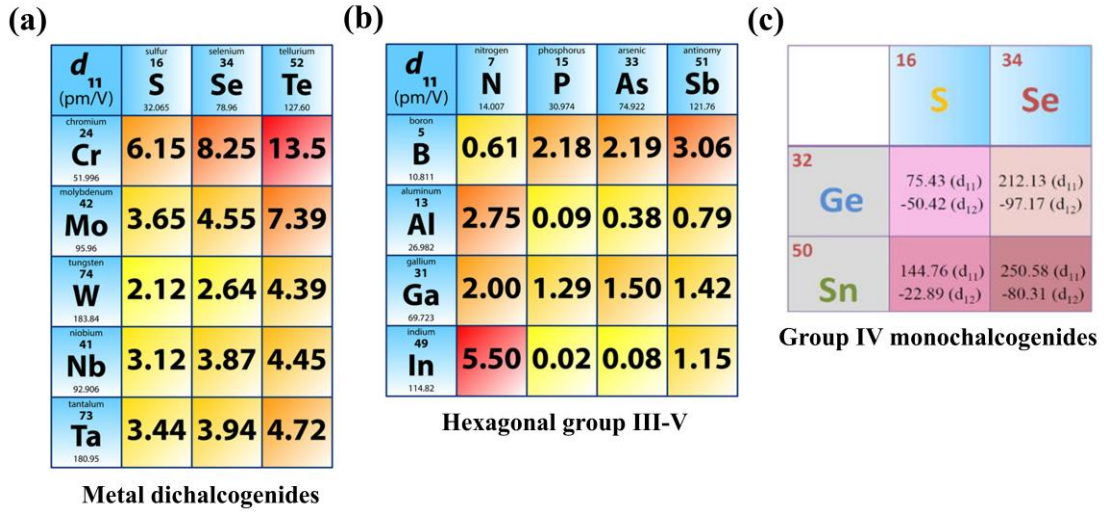

Figure 1.10 Predicted periodic trends for d_{11} in TMDs (a), group III–V (b) as well as group IV monochalcogenides (c).[42, 46]

The mechanism of piezoelectricity in layered nanosheets is illustrated in Figure 1.11, taking MoS_2 as an example. When subjected to an in-plane electric field directed from the S site towards the Mo site (as illustrated in Figure 1.11a), the MoS_2 lattice would elongate owing to the extending of the Mo-S bond.[44] Under external strain, their output current at the opposite drain biases is asymmetric. By constructing the piezoelectric device with metal electrodes, piezoelectric output could be measured by applying strain. The strain polarization contributes to a change to Schottky barrier height, thus leading to the piezotronic behaviour as demonstrated in Figure 1.11b. When the device is stretched, strain-induced negative and positive piezo-charges are at the

drain and source terminals, respectively. The electrons gathering at the interface contributes to an increased Schottky barrier height, while the holes gathering results in a decreased Schottky barrier, which leading to an asymmetrical current. When a compressive strain is applied to the device, the behaviour of the ionic polarization charges would be reversed. By contrast, piezoresistive effect with symmetrical current output could be found in the bilayer and bulk MoS_2.[53]

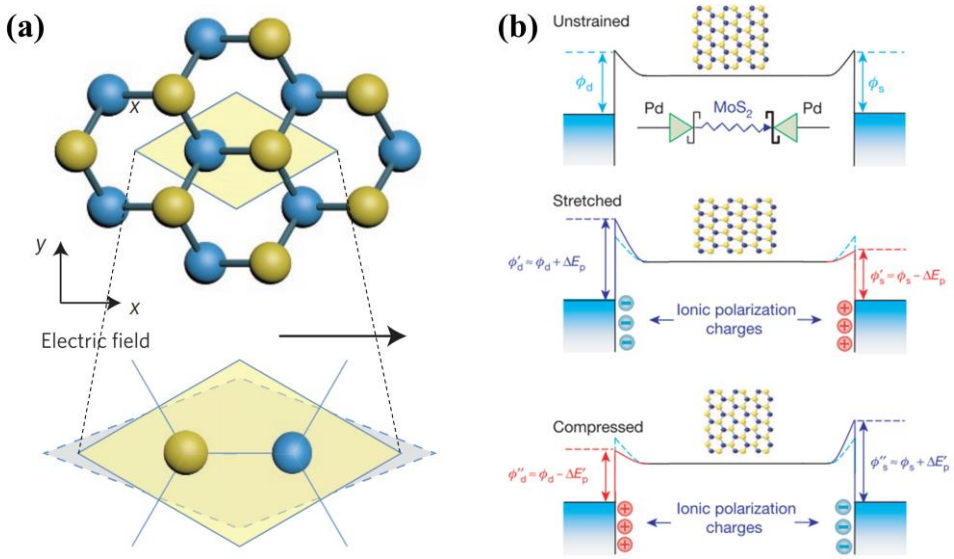

Figure 1.11 (a) Elongation of the MoS_2 under an in-plane electric field applied from the S site (yellow) to the Mo site (blue).[44] (b) Band diagram of piezotronic behaviour in single-layer MoS_2.[53] ϕ_d and ϕ_s is the Schottky barrier heights at drain and source contacts, respectively. E_p is the variation in Schottky barrier height resulting from the ionic polarization charges.[53]

1.2.2 Piezoelectric engineering

However, the limited intrinsic piezoelectric constants could impede their broader utilization. Since the influence of the surface of layered materials is significant with

various intriguing physical phenomena, a series of works have been done to engineer their piezoelectric response by introducing new atoms, defects or proposing novel stacking configuration, as shown in Figure 1.12. The surface S vacancies in MoS_2 were passivated by S treatment (Figure 1.12a) by reducing free charge carriers, thus significantly preventing the screening effect of piezoelectric polarization charges resulted from the free carriers.[54] This S treatment was also consistent to an increased responsivity of a MoS_2-based phototransistor by defect repair to suppress free-carrier screening effect.[55] It was also found that the defects at the grain boundaries (Figure 1.12b) could significantly improve its piezoelectric response by changing the symmetry of its crystal structures and inducing spontaneous piezoelectric polarization along various directions.[56] The pristine bilayer WSe_2 with very weak piezoelectricity could be non-centrosymmetric by turbostratic stacking (Figure 1.12c), which increases the degrees of freedom and thus induces strong piezoelectricity.[57] Similarly, the special stacking structure of 3R-MoS_2 endows it promising piezoelectricity regardless of the stacking thickness.[58] By replacing the top-layer S with Se atoms in MoS_2, monolayer Janus MoSSe (Figure 1.12d) was synthesized to break the out-of-plane symmetry.[59] Besides, the enhanced piezoelectric response of some other TMDs are also investigated, such as WS_2 by a unique solvent-vapour annealing process[60] and by applying in-plane deformation,[61] and by fabricating WSe_2/MoS_2 heterostructure,[62] and $MoTe_2$ by creating surface corrugation[63] and thermal annealing process.[64]

Inspired by above engineering strategies, it is feasible to explore the enhanced

piezoelectric response of promising TMDs or other layered materials. For example, engineered piezoelectricity is also explored in graphene, which does not exhibit intrinsic piezoelectricity because of the inversion centre-symmetry. Various methods were employed to break the inversion symmetry and result in possible piezoresponse, such as stacking control in graphene bilayers, applying inhomogeneous strain, and chemical doping.[65] Although the engineered graphene and TMDs enables to realize better properties in nanogenerators, the piezoelectric responses are not strong enough to realize nanogenerators with better performance.

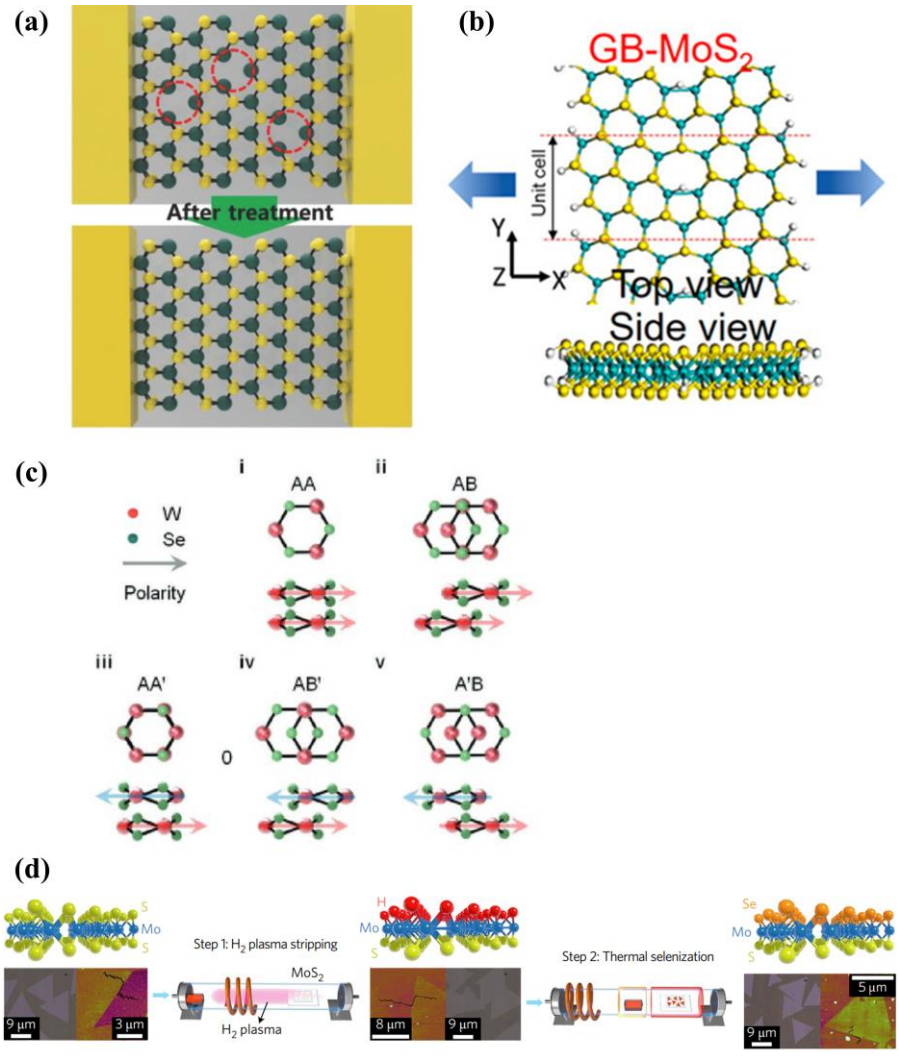

Figure 1.12 Several piezoelectric engineering methods. (a) Point-defect-passivated

MoS_2.[54] (b) Grain boundary in MoS_2.[56] (c) Turbostratic stacking in bilayer WSe_2.[57] (d) Janus MoSSe monolayer.[59]

Apart from extensively-explored TMDs and graphene, different groups of layered materials are explored with high piezoelectric constant and facile fabrication method, which is also anther solution to achieve high-performance piezoelectric devices. A class of layered van der Waals materials like α-In_2Se_3 and γ-InSe were discovered to exhibit piezoelectric effects regardless of odd- or even-layer numbers, which is different from intrinsic TMDs.[66] It is worth mentioned that In_2Se_3 intrinsically inter-correlated in-plane and out-of-plane polarization for applications in ferroelectric switching and piezoelectric nanogenerator devices. The SnS_2 nanosheets were also investigated to exhibit intrinsic piezoelectricity and then fabricated a piezoelectric nanogenerator to display the energy harvesting and active sensing capabilities.[67] In addition, the giant piezoelectric coefficient of liquid metal produced monolayer SnS was confirmed and it was applied it into a piezoelectric nanogenerator with high conversion efficiency.[68] These studies provide different promising piezoelectric materials for practical nanogenerator application. The experimentally confirmed piezoelectric coefficients of layered nanosheets are outlined in Table 1.1. From these results, it could be found that the experimentally measured piezoelectric coefficients were relatively lower than that obtained from simulations in Figure 1.10, which is also related to the synthesis method and quality of the obtained samples. Therefore, the high-quality non-centrosymmetric layered materials are highly desired for practical piezoelectric applications.

Table 1.1 Overview of experimentally validated piezoelectric layered materials.

Layered nanosheets	**Experimental results (Notes)**
Monolayer MoS_2	$e_{11} = 2.9 \times 10^{-10}$ C/m[44] d_{11} = 3.06 ± 0.6 (pristine) and 3.73 ± 0.2 pm/V (Defect-Passivated)[54] d_{11} = 3.78 (armchair) and 1.38 (zigzag) pm/V[69]
Monolayer WS_2	$d_{33,\,eff}$ = 11.33 pm/V (originating from flexoelectricity, sulfur vacancies or the deformation of the nanosheets)[70]
WSe_2	d_{11} = 3.26 ± 0.3 pm/V (monolayer-WSe_2) and 1.5 pm/V (turbostratic-stacking-WSe_2)[57]
2H-$MoTe_2$	$d_{33,eff}$ = 1.31 pm/V (125 nm thick, introduce out of plane piezoelectricity by creating surface corrugation)[63]
Monolayer $MoSe_2$	e_{11} = 435 pC/m[71]
SnS	d_{33} = ~5 pm/V (4 nm, ~ 6 layers, originating from strain gradient-induced flexoelectricity)[67] $d_{11,\,eff}$ = 26.1 ± 0.3 pm/V (mono-layer)[68]

Layered nanosheets	**Experimental results (Notes)**
α-In_2Se_3	d_{33} = 0.34 pm/V (monolayer), 0.6 pm/V (bilayer) and 5.6 pm/V (exceeding 90 nm)[72]
MoO_2	d_{33} = 0.56 pm/V (~8.7 nm)[73]
α-Tellurene	d_{33} = 1 pm/V (1 nm)[74]
Monolayer Janus MoSSe	d_{33} = 0.1 pm/V[59]

1.3 Significance of research

Layered materials offer a plethora of advantages stemming from their unique atomic structure and exceptional properties. One of the standout characteristics of layered nanosheets is their extraordinary mechanical properties. Despite being atomically thin, these materials exhibit remarkable strength, stiffness, and flexibility. The mechanical robustness, coupled with flexibility, enables the integration of layered materials into a widespread array of applications, such as flexible electronics and integration systems. Another key advantage of layered materials lies in their tunable electronic properties. By manipulating different factors, such as strain, doping, and layer stacking, the electronic characteristics of these materials can be precisely controlled. This tunability allows for the customization of band structures, carrier

mobility, and bandgaps, making layered materials versatile candidates for advanced electronic devices. The ability to tailor electronic properties to specific requirements is crucial for applications ranging from high-speed transistors to quantum devices, showcasing the adaptability and potential of layered materials in the electronics industry. Furthermore, the high surface-to-volume ratio of layered nanosheets is also the significant advantage that underpins their diverse applications. This unique feature provides an extensive surface area for interactions with different materials, enhancing their effectiveness in catalysis, sensing, and energy storage applications. The large surface area enables enhanced reactivity, increased adsorption capacities, and improved sensitivity in sensors. By leveraging this exceptional surface characteristic, layered materials offer innovative solutions for a wide range of cutting-edge technologies. In summary, the outstanding mechanical properties, tailorable electronic characteristics, and exceptional surface-to-volume ratio of layered materials collectively underscore their immense potential for revolutionizing various industries, from electronics and energy storage to catalysis and beyond. These advantages not only showcase the versatility and adaptability of layered materials but also highlight their role as key enablers of future technological advancements and innovations.

In the 2D layered material family, SnSe excels in thermoelectric applications and offers tailored electronic capabilities, waiting for in-depth study for practical applications. However, the ability to realize large-scale controllable growth of high-quality layered SnSe materials has become a crucial requirement for its broad

application. The high bonding energy makes it hard for obtaining ultrathin SnSe layers by simple mechanical exfoliation. Besides, there are some contaminants in the as-prepared SnSe by the solution-phase methods. By comparison, vapor deposition method with controllability and the potential for large-scale production would be a good choice. So far, the growth of SnSe using vapor deposition techniques faces challenges such as small dimensions, mixed phases, and a rapid increase in thickness with increasing size. These issues will significantly influence the subsequent device fabrication processes of SnSe and its practical applications. In this thesis, vapor transport deposition method is employed to synthesize SnSe layered nanosheets with high quality and large scale. Research into the improved piezoelectric characteristics of SnSe nanosheets is also being explored. Moreover, self-powered piezoelectric nanogenerators and electronic devices are well developed, presenting the potential for applications in next-generation flexible electronics and hybrid device applications.

1.4 Thesis outline

The background of layered materials is first literature-reviewed about their structure, basic properties and intriguing applications. The group IV-VI monochalcogenides will be discussed more explicitly in this chapter. Next, the experimental methods employed in this thesis and their corresponding mechanism are introduced, including synthesis method, Raman, XRD, SEM, EDX, SHG, TEM, PFM, the device fabrication process as well as the electrical measurements. The following chapter demonstrates the growth process and the relevant characterization of SnSe

nanosheets in detail. In the next chapter, the developed SnSe-PENG will be discussed in terms of the in-plane piezoelectric properties of SnSe, the piezotronic effect, electrical properties and the self-powered performance of the nanogenerators. Subsequently, the next chapter features the synthesis of high-entropy MXene nanosheets and flexible nanogenerators based on MXene-PVA composite film. The thesis ends with a brief summary of overall results and a discussion about the promising prospects of the research.

Chapter 2 Experimental Methodology

2.1 Synthesis of layered SnSe nanosheets via vapor transport deposition

In previously reported synthesis of layered SnSe nanosheets, mechanical exfoliation, solution-phase methods (i.e. liquid-phase exfoliation and one-pot method), and vapor transport deposition have been proposed.[75-78] In order to obtain large-scale and high-crystalline SnSe nanosheets in a controllable way, here, we employed vapor transport deposition (VTD) technique for synthesis.

Vapor transport deposition encompasses both chemical vapor deposition (CVD) and physical vapor deposition (PVD). The difference between them is that the former involves chemical reaction, while the latter does not. This method is a bottom-up growth technique for layered materials. To date, the vapor transport deposition technique has successfully enabled the synthesis of a diverse range of layered nanomaterials, such as graphene, h-BN, and TMDCs. These advancements highlight the versatility and efficacy of vapor transport deposition as a method for fabricating various layered materials with diverse properties and potential for electronics, optoelectronics, and beyond. During the vapor transport deposition process (Figure 2.1), the precursor reactants first flow into the reaction chamber by carrier gases as the growth temperature is achieved, as the route a shown in Figure 2.1. They could diffuse through boundary layers or attach to target substrates (route b or c). Alternatively, they could directly achieve the formation of reaction intermediate and byproducts through

gas-phase reaction (route d), which are then deposited onto the substrate by diffusion or adsorption (route b or c). Finally, the thin film will be formed on the substrate after the heterogeneous reaction (route e), while the by-products and unreacted substances will be released from the surface and drained out of the chamber (route f).[79]

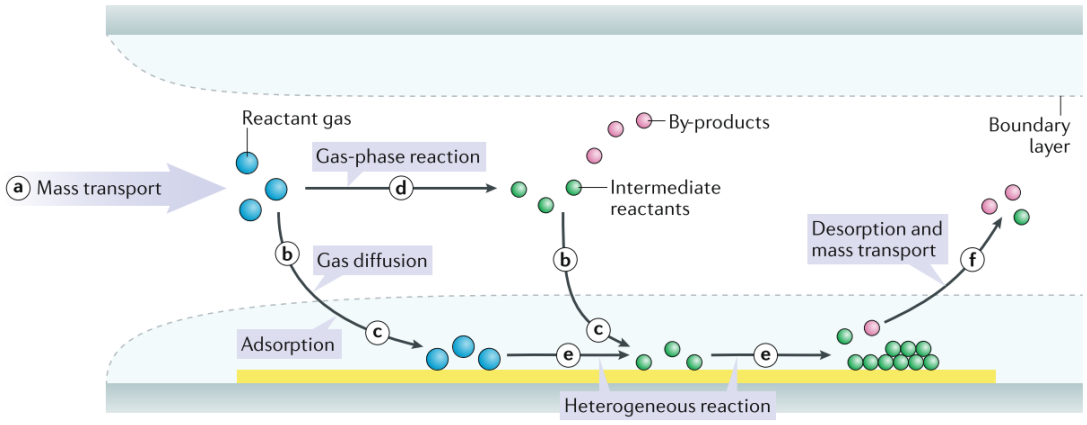

Figure 2.1 The deposition routes for vapor transport deposition process.[79]

The vapor transport deposition growth process is subject to control through various influential aspects. Among these factors, the temperature of substrate emerges as a key parameter, determining both the reaction rate and the mobility of atoms or molecules. Elevated temperatures generally facilitate higher growth rates, albeit at the potential expense of defects and impurities. Conversely, lower temperatures yield slower growth rates but hold promises for higher-quality films. Another significant factor is the pressure within the reaction chamber, exerting influence on precursor gas transport and reaction kinetics. Higher pressures enhance precursor gas transport to the substrate surface, thereby fostering accelerated growth rates. However, excessively high pressures may lead to non-uniform deposition and undesired effects. The selection of

appropriate precursors is also pivotal in governing the growth process. Reactivity and compatibility with the desired material guide the choice of precursors. Modulating the composition and flow rate of precursors allows control over the stoichiometry and the thickness of nanosheets. Additionally, the utilization of catalysts as well as substrates with specific crystal orientations can exert notable influence on the growth process. Suitable catalysts expedite nucleation and growth of the desired material, while crystal-oriented substrates promote alignment and epitaxial growth of the film. Furthermore, external energy sources (such as plasma or laser irradiation) can be harnessed to augment the growth process. These energy sources furnish supplementary activation energy, thereby enhancing sample quality and imparting unique material properties.[79, 80]

2.2 Synthesis of layered MXene nanosheets

Generally, central to the synthesis of MXene nanosheets is the selective etching process of the A-group element from MAX phases, typically achieved through the use of potent acids or specialized etchants, leading to the exposure of MXene layers and the formation of layered nanosheets with tailored surface functionalities. Figure 2.2 describes the MXene synthesis process, including synthesis of precursors, selective A-atom layers etching and delamination of MXene multilayers.[81] Various top-down synthesis approaches are employed in the preparation of layered MXene nanosheets, consisting of HF-related etching, electrochemical etching, alkali-related etching, and molten salt etching, as well as the delamination techniques. The traditional chemical

etching method stands out as a prevalent technique, involving the immersion of MAX phase precursors in etchants, such as HF and HCl, resulting in the delamination of layers and the production of MXene nanosheets. As shown in Figure 2.2, during the etching process, the A layers are first etched due to the relatively weak M-A bonds, and then the freshly etched MXene multilayers are further exfoliated to achieve monolayer or few layers, with surface terminated by the functional groups from the etchant, while the A layers are bonded with ligands and dissolved away in the solution. Taking the synthesis of Ti_3C_2 nanosheets by HF etching as an example, the etching process begins with the attachment of H and F atoms to Ti, which will relax the Ti-Al bonds, eventually exfoliating the Al layers in the form of soluble AlF_3, and offering some interlayer spaces for the subsequent infiltration and etching of HF and H_2O. The following reactions describe the chemical process:[81]

$$Ti_3AlC_2\ (s) + 3H^+\ (aq) \rightarrow Ti_3C_2\ (s) + Al^{3+}\ (aq) + 3/2H_2\ (g) \quad (2\text{-}1)$$

$$Al^{3+}\ (aq) + 3F^-\ (aq) \rightarrow AlF_3\ (aq) \text{ and } Al^{3+}(aq) + 6F^-\ (aq) \rightarrow AlF_6^{3-}\ (aq) \quad (2\text{-}2)$$

$$Ti_3AlC_2\ (s) \rightarrow Ti_3C_2\ (s) + 3e^- + Al^{3+}\ (aq) \quad (2\text{-}3)$$

In general, the etching process does not occur simultaneously in all MAX layers but rather proceeds layer by layer. The surface layer is etched first, while the middle layers remain intact, which may be due to the strain and deformation generated by the etching process, limiting the etching efficiency for the simultaneous-etch in MAX layers. The strength of the M-A bonds in the precursor and the number of MXene layers

(n value) also affect the etching conditions. Generally, the stronger the M-A bonds, the longer the time or the more intense the etching conditions required; and the larger the n value, the thicker the MXene layers, the more stringent the etching conditions required. In contrast, in situ HF-forming etching strategy using HCl and LiF as etchants facilitates safer control during the etching process.[82] Besides, alkaline etching concentrated alkaline solutions (such as NaOH or KOH) under hydrothermal conditions to etch the MAX phase, obtaining fluorine-free MXene and enabling the formation of well-defined nanosheets under specific temperature and pressure conditions.[83, 84] In addition, the molten salt etching method uses fluoride or non-fluoride molten salt systems to etch the MAX phase with higher energy barrier at high temperatures.[85]

Furthermore, electrochemical etching utilizes a mild electrochemical process to selectively remove the metal layers from the MAX phase, which is simple to operate, well-controlled, and does not require the use of HF. As a result, this method is employed for MXene synthesis in this thesis. In the electrochemical system, the MAX phase serves as the working electrode, and under a certain voltage, the metal atomic layer is selectively removed to form MXene by breaking the M-A bonds. As the voltage is further increased, the M layer will also be removed, ultimately forming an amorphous carbon material. Therefore, by controlling the etching voltage range and time, the selective removal of the metal layer can be achieved, thereby precisely controlling the synthesis of MXene layers. To improve the contact between the MAX phase and the electrolyte, an electrolyte containing chloride ions (such as HCl) can be used to enhance

the interaction between the metal layer and Cl-containing electrolytes, thereby improving the etching efficiency.[86] At the same time, the addition of substances such as Tetramethylammonium hydroxide (TMAOH), which can expand the interlayer spacing of the MAX phase, also helps to improve the etching efficiency.[83] In addition, a thermally assisted electrochemical etching method can also be adopted, where under certain temperature and time conditions, the HCl electrolyte can effectively etch different types of MAX phases to obtain MXene layers.[87]

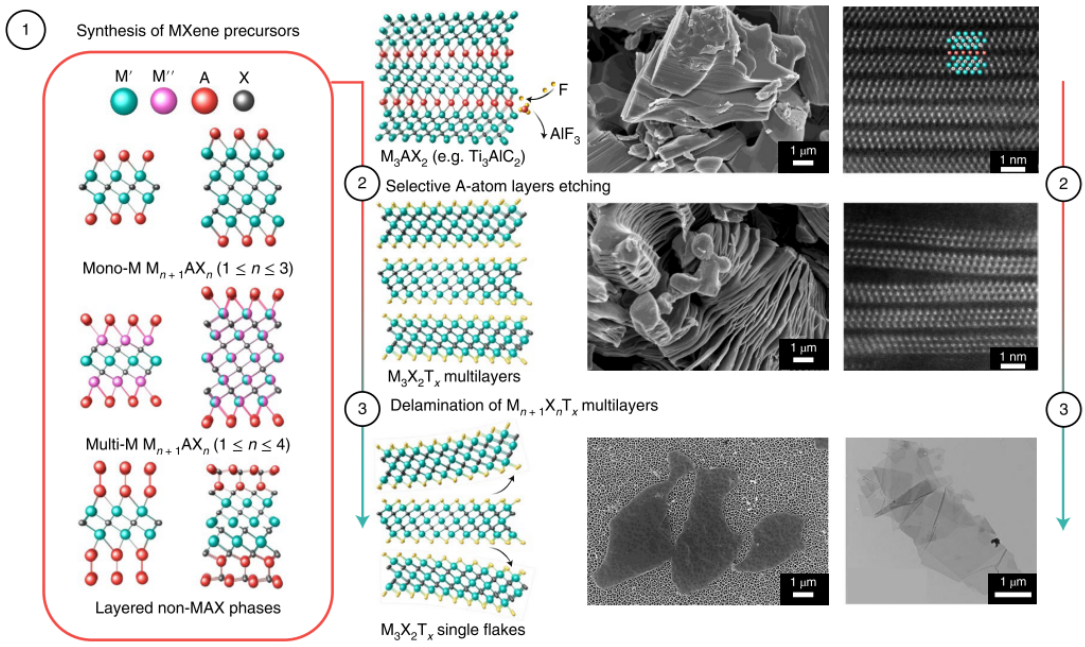

Figure 2.2 Schematic diagram of MXene synthesis by top-down etching: ① precursor synthesis, ② selective A-atom layers etching and ③ delamination of multilayers.[81]

On the other hand, instead of delamination of the MAX compound, MXene nanosheets could be fabricated by bottom-up CVD growth.[88-91] Compared to selective etching, MXene nanosheets synthesized by CVD have higher crystal quality. Furthermore, the CVD method can also synthesize certain stoichiometry of transition

metal carbides and nitrides, such as WC, TaC, TaN, MoN, and heterojunction structures, which cannot be obtained by selective etching.[88] Although it is currently not possible to directly grow monolayer transition metal carbides and nitrides, the obtained ultrathin films still exhibit layered characteristics, such as superconducting transitions.

In comparing these methods, chemical etching emerges as a straightforward and widely adopted approach, while intercalation and delamination offer precision in synthesis and modification of MXene properties. On the other hand, hydrothermal synthesis, although allowing for precise morphological control, is constrained by specific environmental conditions and longer synthesis times. Understanding the nuances and intricacies of these synthesis techniques is paramount for advancing MXene materials research and exploiting their full potential across diverse applications. Continued research and development in MXene synthesis methodologies are crucial for unlocking the vast capabilities of these versatile layered materials and propelling innovations in diverse fields of science and technology.

2.3 Material characterization

2.3.1 Raman spectroscopy

Raman spectroscopy offers comprehensive qualitative and quantitative analysis in a non-destructive way, providing valuable insights into the chemical compositions and structural characteristics of target materials. The underlying principle of Raman spectroscopy is illustrated in Figure 2.3. As the light interacts with the target samples, the majority of photons are scattered with the identical energy as the incident light ($\hbar\omega_0$),

i.e. elastic scattering or Rayleigh scattering (Figure 2.3a). However, a minute fraction of the scattered light exhibits a distinct wavelength from the incident light, with the magnitude of this wavelength shift determined by the chemical compositions of the target sample. This phenomenon is recognized as Raman scattering and encompasses Stokes and anti-Stokes scattering. In case of Stokes scattering (Figure 2.3b), energy is transferred from the incident light to the molecule, resulting in the molecule reaching an excited quantum state and the Stokes scattered photon possessing a lower frequency than the incident photon. Conversely, anti-Stokes scattering arises when the target material is initially located in an excited quantum state and returns to ground state after Raman scattering. Here, the energy of molecular vibrations is transferred to the scattered photon, causing the frequency of the anti-Stokes photon to exceed that of the incident photon.[92]

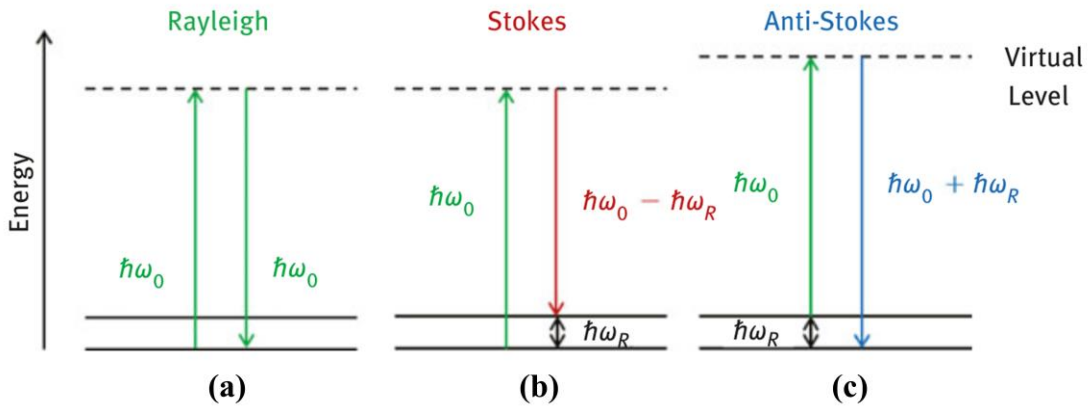

Figure 2.3 Schematic energy diagrams of Rayleigh (a), Stokes (b), and anti-Stokes (c) Raman scattering.[92]

A Raman spectrum exhibits multiple peaks that signify the wavelength position and intensity of the scattered light, serving as indicators of specific molecular bond

vibrations. According to the displacement of atoms in lattice vibrations, Raman modes in layered nanomaterials are generally divided into intralayer and interlayer modes. The intralayer modes arising from chemical bonds within a single layer provide information about composition and structural phase. On the other hand, the interlayer modes involve the movements between layers (i.e. layer-layer vdW interaction), which is highly influenced by the layer numbers and stacking order of layered nanosheets. Consequently, the Raman scattering process facilitates comprehensive characterization of chemical structure, crystallinity, and molecular interactions within layered nanosheets, enabling a nuanced understanding of their properties.

2.3.2 X-ray diffraction

X-ray diffraction (XRD) stands as an essential technique for examining the physical attributes encompassing phase, structure, and orientation of target samples. By generating unique diffraction patterns, XRD plays a pivotal role in the identification of distinct crystalline phases, enabling researchers to compare these patterns with established reference databases for comprehensive analysis. The resulting constructive interference yields characteristic diffraction patterns, which are essential for the precise determination of crystal structures. Rooted in the pioneering work of W.L. Bragg, XRD delves deeper into the atomic arrangements and electron density within crystals, offering detailed insights into chemical bonds, structural properties, and disorder phenomena.[93]

The principle of XRD is shown in Figure 2.4. Due to their high energy, X-rays

induce periodic movements of atoms within a crystal upon entry, leading to the emission of secondary waves in atomic spheres (known as X-ray scattering). These emitted waves align in frequency with the incident beam. Given the organized atomic arrangement in the sample, a consistent phase relationship exists among these scattered waves, causing spatial interference effects. Consequently, in specific scattering directions, spherical waves reinforce each other, while in others, they will be offset, resulting in diffraction phenomena. In essence, XRD within a crystal emerges from the spatial interference of numerous atomic scattering waves, illustrating the complex interplay of waves within the crystal lattice. This method harnesses the power of X-rays to discern molecular geometry through the process of elastic scattering from structures characterized by long-range order, capitalizing on the wavelength resonance with inter-atomic spacing within crystals to induce diffraction. The geometrical interpretation in this process could be described by Bragg's law:[93]

$$sin\,\theta = \frac{n\lambda}{2d_{hkl}} \tag{2-4}$$

Where θ, λ and d_{hkl} denotes the angle between the incident X-ray beam and the lattice plane, wavelength of the incident/diffracted beam and the lattice spacing, respectively.

A diffraction pattern can be viewed as comprising two key elements: one is the spatial arrangement of diffraction lines, influenced by the dimensions, geometry, and alignment of the unit cell; the other one is the strength of the diffracted signal, which correlates with the atomic nature and placement within the unit cell. Through discerning

the spatial distribution and intensity of diffraction patterns, a detailed relationship can be established between XRD and the underlying crystal structure, enabling qualitative and quantitative analyses of crystal properties. In this thesis, XRD analysis was performed in Rigaku SmartLab 9Kw (Advance mode).

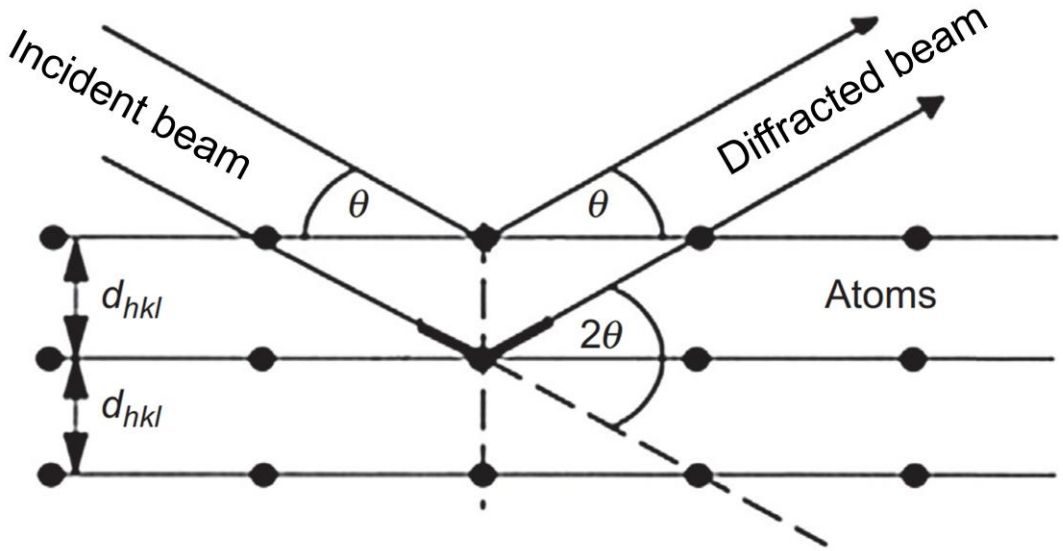

Figure 2.4 Principle of X-ray diffraction.[94]

2.3.3 Scanning electron microscopy and energy dispersive X-ray mapping

Scanning electron microscopy (SEM) serves as a highly effective technique for analyzing the topography and morphology of nanomaterials. The key components of an SEM system are depicted in Figure 2.5. High-energy electrons are generated by an electron gun and subsequently traverse electromagnetic lenses, ultimately converging on the surface of the target samples, as shown in Figure 2.5a. During the electron-matter interactions, various signals are generated, including backscattered electrons, auger electrons, cathodoluminescence, secondary electrons, and characteristic X-ray radiation, as shown in Figure 2.5b. These distinct signals convey information regarding different

depths within the target samples and are detected by corresponding detectors operating in different modes. By employing scan coils to trace a predetermined trajectory, SEM captures topological information in a point-by-point manner across the sample surface, ultimately producing a comprehensive SEM image.[95, 96]

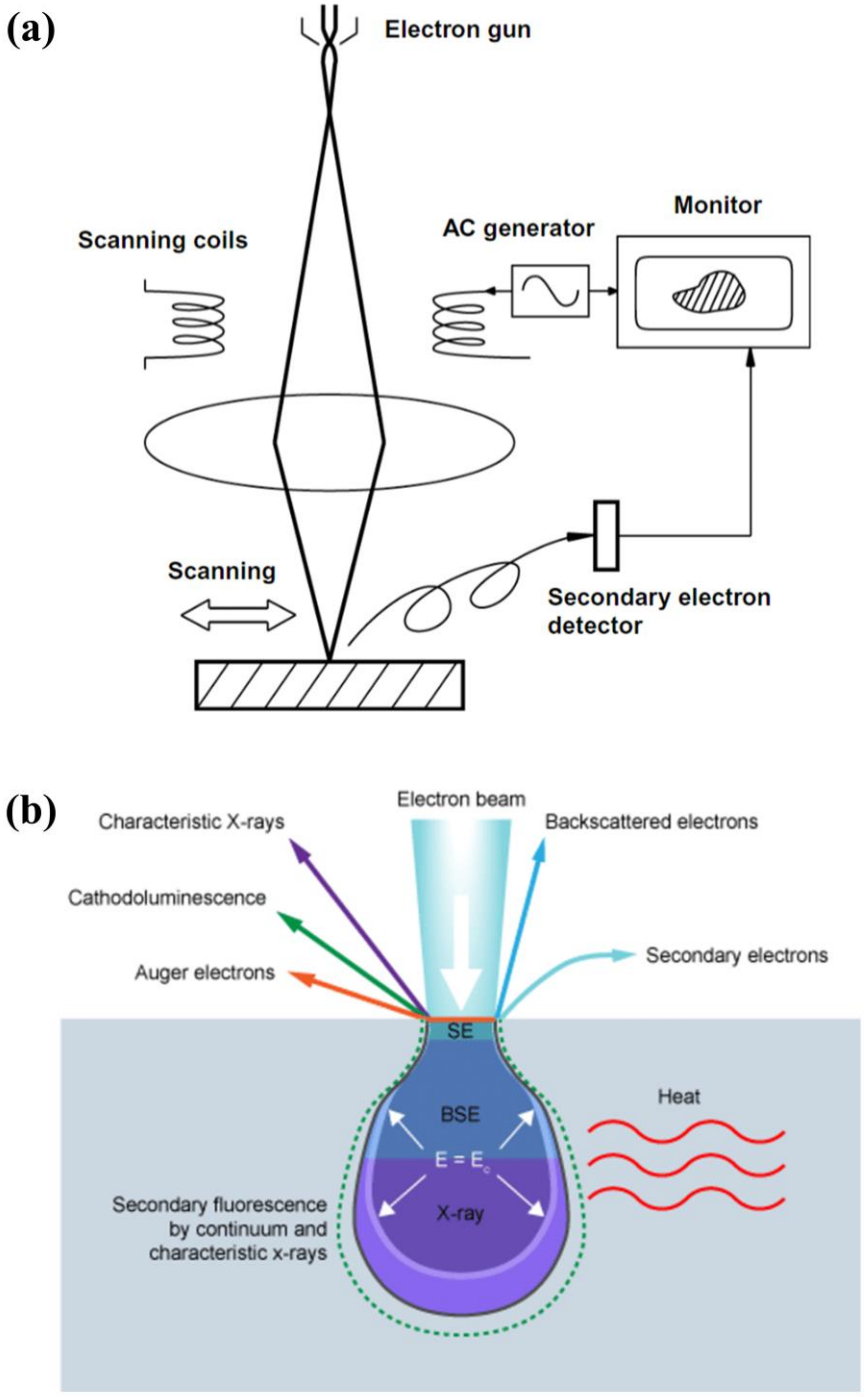

Figure 2.5 (a) Basic SEM layout.[96] (b) Electron beam interaction diagram.[97]

The integration of an Energy Dispersive X-ray (EDX) detector within the basic framework of SEM facilitates the segregation of X-ray characteristics produced by different elements into an energy spectrum. By analyzing the detailed information contained within the energy spectrum and chemical composition maps, we could determine the specific elements present in the scanned materials, along with their respective concentrations. In this thesis, SEM images and EDX measurements were acquired using the Tescan VEGA3 SEM instrument. In order to enhance conduction on the sample surface, the layered nanosheets were sputter-coated with gold.

2.3.4 Second harmonic generation

The second harmonic generation (SHG) technique has garnered significant interest in the analysis of nanomaterial structures due to its high sensitivity and versatility, complemented by full-optical detection capabilities. The SHG signal encompasses multiple types of polarization, including electric dipoles, electric quadrupoles, as well as magnetic dipoles. These polarization components carry vital details about the structural, electronic, as well as magnetic properties of the target nanosheets. The SHG phenomena can be describe as[98]

$$\boldsymbol{E}(2\omega) \propto \boldsymbol{P}(2\omega = \omega + \omega) = \chi^{(2)}(\omega, \boldsymbol{q}) : \boldsymbol{E}(\omega)\boldsymbol{E}(\omega) \qquad (2\text{-}5)$$

where ω and $\mathbf{q}$ represent the incident frequency and photon wave vector, respectively. $\chi^{(2)}(\omega, \mathbf{q})$ is the nonlinear susceptibility tensor. It is observed that the output signal frequency is twice that of incident electric field, i.e. $\mathbf{E}(\omega)$, as shown in Figure 2.6a. Since the magnitude of $\mathbf{q}$ is generally small,

$$\chi^{(2)}(\omega, \mathbf{q}) \approx \chi^{(2)}_{\mathrm{ED}}(\omega) + \chi^{(3)}_{\mathrm{EQ}}(\omega)\mathbf{q} + o(\mathbf{q}^2) \quad (2\text{-}6)$$

where $\chi^{(3)}_{EQ}(\omega)$ represents a term related to the electric quadrupole and magnetic dipole. $\chi^{(2)}_{ED}(\omega)$ tensor contributes to electric dipole, which is dominant in $\chi^{(2)}$ and extremely sensitive to variations in symmetry. Furthermore, it is exclusively allowed in non-centrosymmetric materials, highlighting the crucial role of material symmetry in determining the presence and magnitude of electric dipole-induced effects.[98]

The appearance of SHG signal typically indicates the break of central inversion symmetry within the material and suggests that the material has non-zero second-order polarizability ($\chi^{(2)}$). As a result, SHG can effectively characterize the structural symmetry of two-dimensional materials. For instance, in a few layers of MoS_2, odd-numbered layers lack central inversion symmetry, resulting in strong SHG response; on the other hand, negligible SHG signal could be detected in even-numbered layers with central inversion symmetry.[99] This property also enables the identification of layer numbers and stack structures. In this thesis, SHG measurements were performed in Leica TCS SP8 MP multiphoton/confocal microscope under 900 nm laser excitation. The typical experimental setup for SHG measurements is demonstrated in Figure 2.6b. The input polarization was adjusted by the rotation of a half waveplate. The generated SHG signals were collected using a CCD and measured in reflected geometry with a photo multiplier tube (PMT) spectrometer.

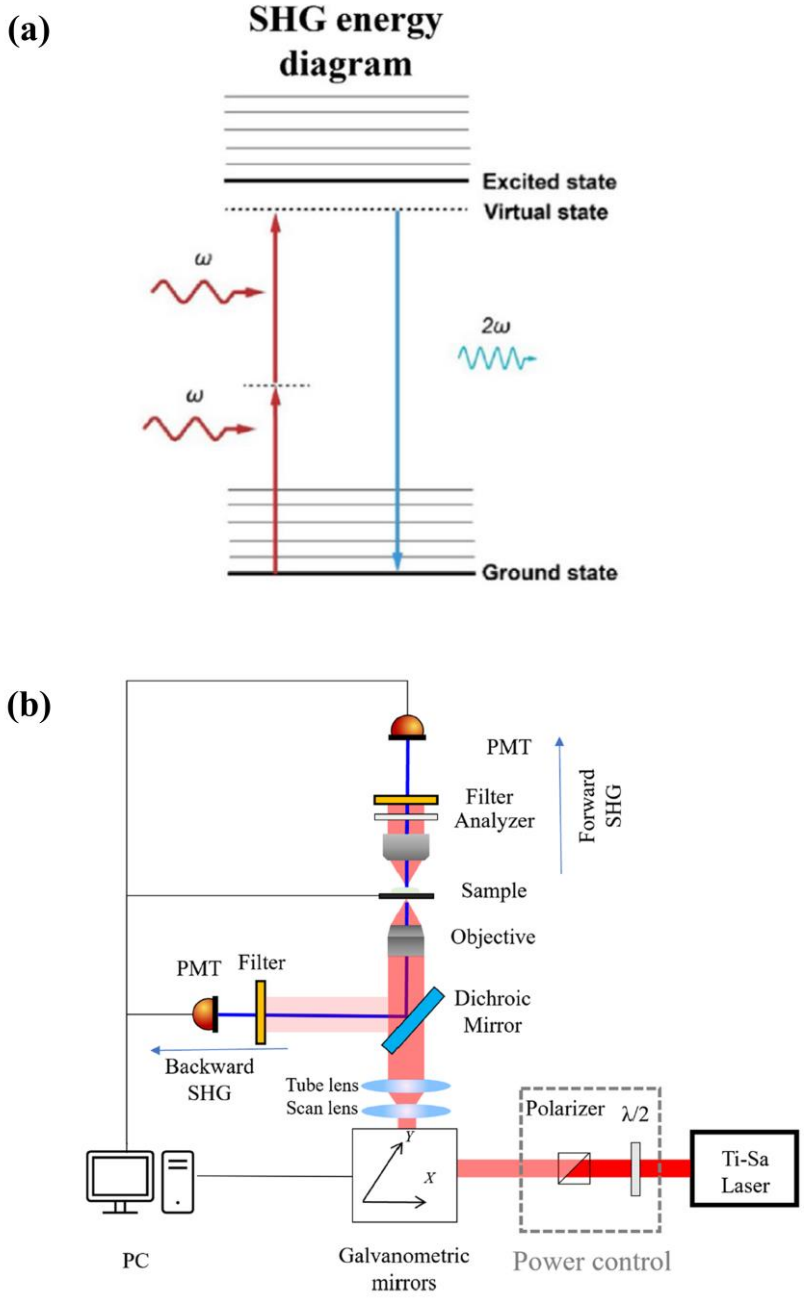

Figure 2.6 (a) Energy level diagram of SHG. (b) SHG microscopy setup.[100]

2.3.5 Transmission electron microscopy and selected area electron diffraction

The transmission electron microscopy (TEM) technique offers atomic-level understandings into morphology, composition, as well as crystal structure of ultrathin nanosheets. The configuration of TEM system is illustrated in Figure 2.7a. Initially, the

electrons are focused into a parallel electron beam through the utilization of two condenser lenses. Subsequently, they penetrate the sample along the objective lens system. In the imaging mode, TEM imaging involves Fourier transformation utilizing a convex objective lens, followed by intermediate lenses and projector lenses to imaging magnification. On the other hand, in the diffraction mode, the parallel electron beam illuminates the sample, resulting in the formation of an electron diffraction pattern at objective back focal plane due to the constructive interference from a specific lattice plane (hkl), as demonstrated in Figure 2.7b.[101] The selected-area electron diffraction (SAED) patterns are visualized via a fluorescent viewing screen and transmitted to a computer via a charged-coupled device (CCD) camera. Due to the nearly parallel alignment of the reflecting lattice planes with the primary beam, the diffraction angle in this system is extremely small (typically $\theta < 1°$). For small angles, we could know the approximation $\sin\theta \approx \theta$, then Bragg's Law can be expressed as

$$\lambda = 2d\theta \tag{2-7}$$

Taking into account the geometric relationship among θ, ring radius R, and equivalent camera length L (Figure 2.7b), we have

$$\lambda L = Rd \tag{2-8}$$

Here, λL denotes the camera constant specific to the TEM and could be determined for instrument configuration and diffraction-lens setting. Equation 2-8 constitutes the fundamental equation for SAED, enabling the determination of the spacing of lattice planes by deducing R (i.e. the distance from the central spot of the transmitted light to

a diffraction spot).[101] In this thesis, high-resolution TEM (HRTEM) imaging and SAED patterns were acquired using the JEOL Model JEM 2100F instrument.

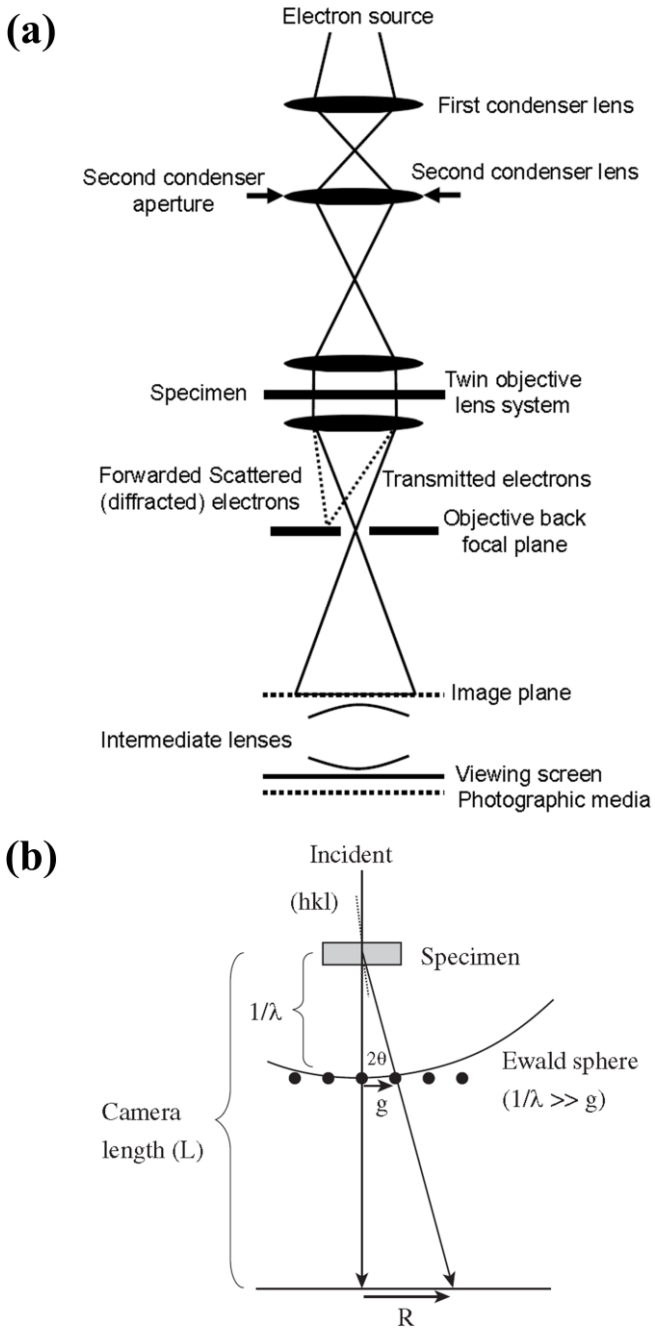

Figure 2.7 (a) A schematic diagram of a TEM instrument.[102] (b) Diffraction pattern imaging.[101]

2.3.6 Piezoresponse force microscopy

Piezoresponse force microscopy (PFM) has been demonstrated as a useful and indispensable technique for characterizing the electromechanical response of piezoelectric and ferroelectric materials. This technique capitalizes on the inverse piezoelectric effect, wherein the mechanical deformations within the target sample are in response to the application of the external electric field. These deformations are subsequently probed and detected by a tip. This mechanical-electrical coupling mechanism of the piezoelectric materials can be elucidated by the equation

$$S_j = d_{ij}E_i \tag{2-9}$$

where *S*, *d*, and *E* denote the field-induced strain tensor, piezoelectric coefficient and electric field, respectively.[103] The experimental setup of a PFM system is illustrated in Figure 2.8. A conductive tip, subject to an alternating current (AC) signal, interacts with the sample during scanning imaging. The scanning process operates in contact mode, enabling real-time monitoring through a laser beam tracked by a sensitive photodetector. This tracking captures the motion of the tip in both the vertical and lateral directions, encompassing deflection, buckling, and torsion. The detected deflection variations of the tip are further sensitively analyzed using a lock-in amplifier at the same frequency.[104] The quantitative estimation of piezoelectric coefficient could be achieved from the slope of the amplitude-drive voltage curve accordingly:

$$A_{piezo} = d_{eff}V_{AC} \tag{2-10}$$

where A_{piezo}, d_{eff} and V_{AC} denote the piezoresponse amplitude, the effective piezoelectric coefficient and the applied AC voltages, respectively. The PFM technique facilitates the

simultaneous acquisition of high-resolution topographic maps and domain maps. This capability allows for detailed investigations of sample morphology, domain structures and switching behavior, providing valuable insights into the intrinsic electromechanical properties of piezoelectric and ferroelectric materials. In this thesis, the in-plane piezoelectricity was examined in lateral PFM (Vector PFM) mode. It is a two-pass technique, where the vertical (out-of-plane) PFM signal is collected in the first pass and then another two orthogonal lateral (in-plane) PFM responses are acquired from the same area by 90° rotations in the second pass. A Pt/Ir-coated tip (Bruker, SCMPIC-V2) with a spring constant of 0.1–0.2 N/m was used.

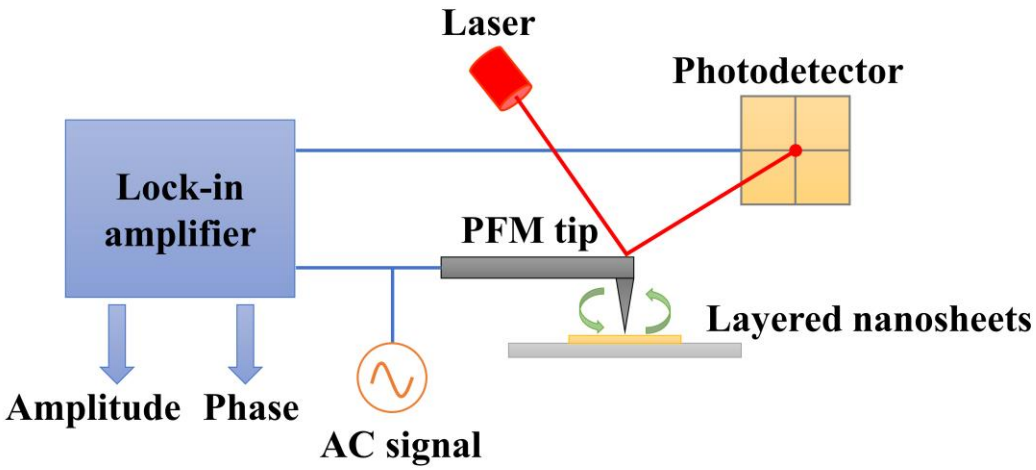

Figure 2.8 Schematic for PFM system.

2.4 Device fabrication and electrical measurements

2.4.1 Device fabrication

In this thesis, the process of device fabrication encompasses several key steps, including material transfer, photolithography, electron-beam (e-beam) evaporation.

Photolithography technique has been extensively used in semiconductor manufacture for generating different patterns on the substrate with high efficiency and precision. A typical UV-lithography process is presented in Figure 2.9. Initially, the photoresist is spin-coated onto a pre-cleaned substrate (step ii in Figure 2.9) and subsequently subjected to baking on a hot plate at 105 ℃ to eliminate the additional solvent from photoresist. A mask with pre-designed pattern is inserted into the photolithography machine for precise alignment with the substrate. The substrate with cured photoresist will experience exposure under UV light under soft contact. After the exposure, the substrate is removed and placed in the developer for full development, so that the photoresist in the exposure area is completely dissolved (step iii in Figure 2.9). Finally, the substrate is washed by deionized (DI) water and dried with dry nitrogen. After completing the photolithography process, the substrate can be examined under an optical microscope to determine whether the process has overexposure, underexposure, pattern drift and other problems. In this thesis, AZ5214E photoresist was used in the photolithography. This positive photoresist is capable of image reversal, leading to a negative pattern of the mask. The spin coater was set to work at 3500 rpm for 30 seconds for uniform spin coating of the photoresist on 300 nm SiO_2/Si and flexible polyimide (PI). The substrate went through soft-baking at 105 ℃ for 3 min following spin-coating. Alternatively, PMGI resists, with superb lift-off properties and good thermal stability, would be spin-coated under the same parameters prior to the photoresist coating. During the photolithography, the exposure time was set to be 7 seconds, and the exposure gap

was 20 μm with soft contact. After that, the substrate was immersed in the AZ300MIF developer for 30 seconds. The pre-designed patterns would be carefully checked for several times after the development to prevent the occurrence of any aforementioned issues.

Subsequent to the photolithography step, the electrodes would be patterned onto substrates by e-beam evaporation (step iv in Figure 2.9), which is a physical vapor deposition technique. The e-beam evaporation instrument is illustrated in Figure 2.10. During the evaporation, the metal source is bombarded by the high-energy electrons emitted from a filament and then accelerated by an accelerator. The electrons are then focused into a unified beam by a powerful magnetic field and directed 270° into the source material crucible. The deposition metal will be evaporated by the transfer of the high energy into thermal energy upon reaching its melting point.[105] To ensure uniform deposition of the electrodes, a rotator is employed during the evaporation process. Fine control over the e-beam evaporation process is achieved by adjusting the voltage of the electron gun and the magnetic field, which govern the energy emission and the focus of output electron beam. Once the desired thickness is attained, the deposition process is halted using a shutter. In this thesis, the current energy and evaporation rate for Ti and Au were 7 % and 0.6 Å/s, and 9 % and 0.5 Å/s, respectively. Finally, 5/50 nm Ti/Au (or 50 nm Au) electrodes were evaporated onto the PI film (or 300 nm SiO_2/Si). The work pressure of e-beam evaporation was around 8×10^{-7} Torr.

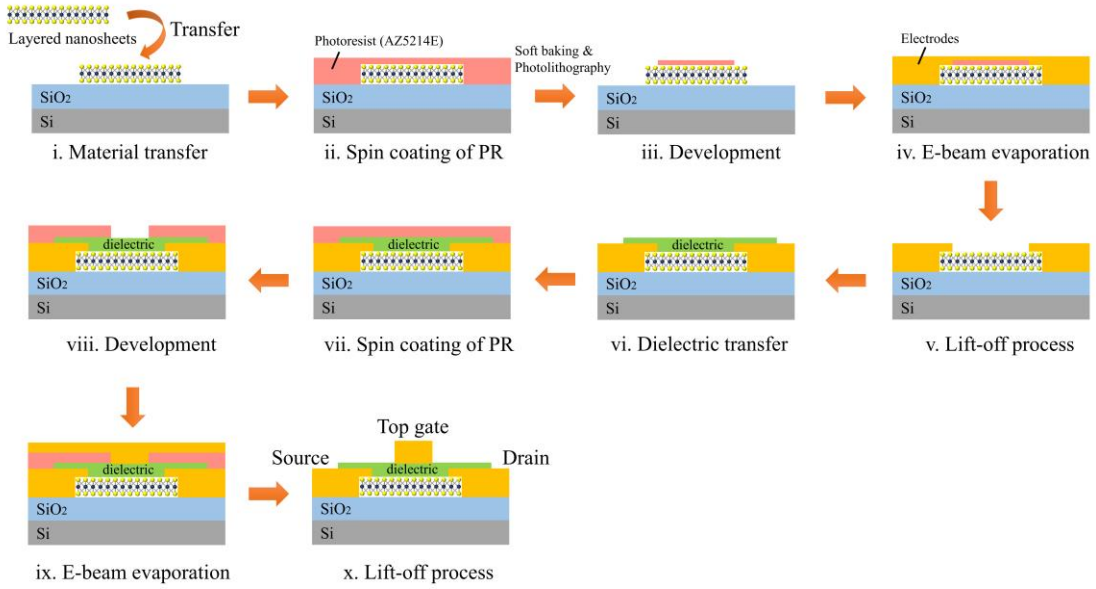

Figure 2.9 The flowchart of device fabrication. i-v: back-gate FET. vi-x: top-gate FET.

Following the e-beam evaporation process, a lift-off technique is employed using acetone to selectively remove the unwanted photoresist (step v in Figure 2.9. This process ensures that the metal remains exclusively in the desired patterned region, resulting in well-defined and precisely positioned electrodes. The acetone or dimethylsulfoxide (DMSO) acts as a solvent, dissolving the photoresist material, while the metal remains intact, adhering to the substrate surface within the designated areas. This lift-off step is crucial for achieving clean and accurate electrode patterns, facilitating optimal electrical performance and device functionality. Alternatively, the top-gate FET could be fabricated by the corresponding step vi-x, including dielectric transfer and metallization of top gate. For convenience and clean surfaces, the top gate electrodes could also be transferred by dry-transfer process, which will be introduced in section 2.4.2.

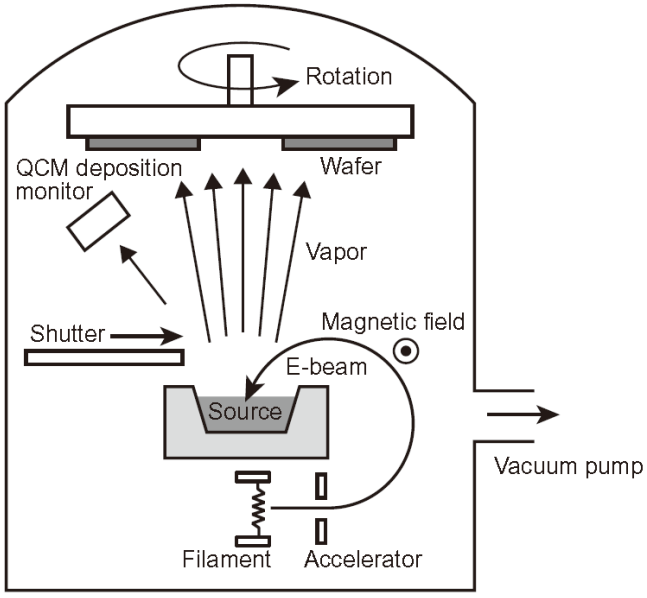

Figure 2.10 Schematic of electron-beam evaporation process.[105]

2.4.2 Transfer process

The transfer process of layered materials typically involves two methods: wet transfer and dry transfer. In case of wet transfer method, polymethyl methacrylate (PMMA) used as the supportive layer is spin-coated on substrates (step ii in Figure 2.11), and then removed by acetone after transfer process (step v in Figure 2.11), so that the samples could be left onto the target substrate. In this procedure, the PMMA layer with samples could be separated by water infiltration (step iii-iv in Figure 2.11), facilitated by the surface energy difference between PMMA and the substrate. Besides, acid or base solution (such as HF-HNO_3 mixture and KOH) could etch away the PMMA layer on SiO_2/Si substrates by chemical reaction with Si.[106] This method allows for transfer materials with relatively strong bonding to the donor substrate, such as those grown by vapor transport deposition method. In this thesis, the PMMA layer was baked at 120 °C for 2 min following spin-coating. The donor substrate 1 would be immersed

in deionized (DI) water

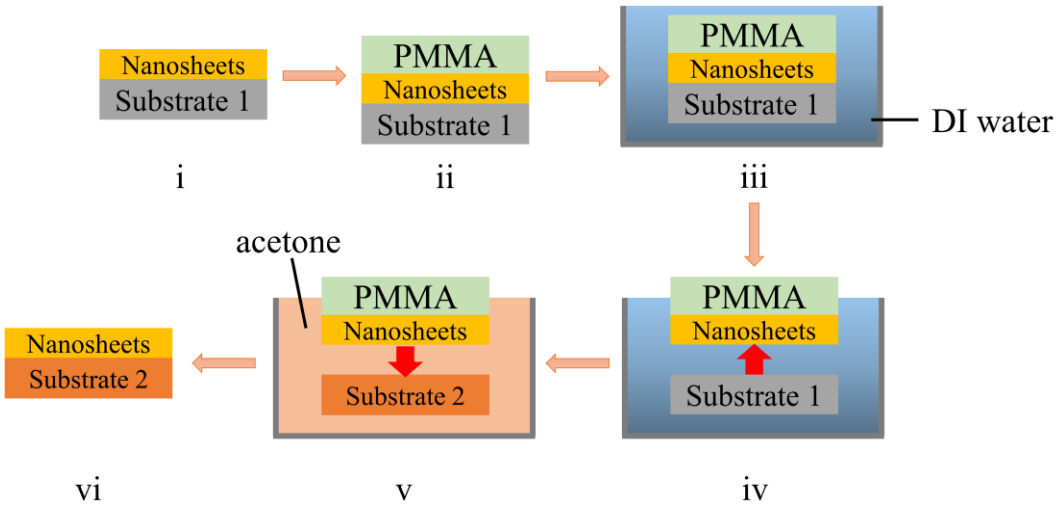

Figure 2.11 Schematic of wet transfer process.

The dry transfer process is illustrated in Figure 2.12. For the dry-transfer technique, a transfer platform (Figure 2.13) is employed to achieve the alignment and transfer in this thesis. The samples to be transferred are clamped on the sample stage by a vacuum bump. A film composed of a layer of polyvinyl alcohol (PVA) and a layer of polydimethylsiloxane (PDMS) is attached onto a glass slide, which is fixed on the moving stage (step i in Figure 2.12). The PVA/PDMS film would be contacted completely on to the substrate after the alignment by the adjustment of the knobs on the moving stage (step ii in Figure 2.12). Subsequently, the sample stage is heated to enhance the bonding between the samples and PVA film. Once the desired temperature is reached, the glass slide is gently lifted, leaving the PVA film adhered to the surface of the substrate. The PVA film is then carefully picked up from the substrate, available for the subsequent transfer onto target substrate (step iii-iv in Figure 2.12). Finally, the

PVA film could be removed by DI water or anhydrous solvent, such as DMSO (step v-vi in Figure 2.12).[107] This dry-transfer method offers a reliable means of transferring samples while maintaining their integrity and preserving their desired alignment.

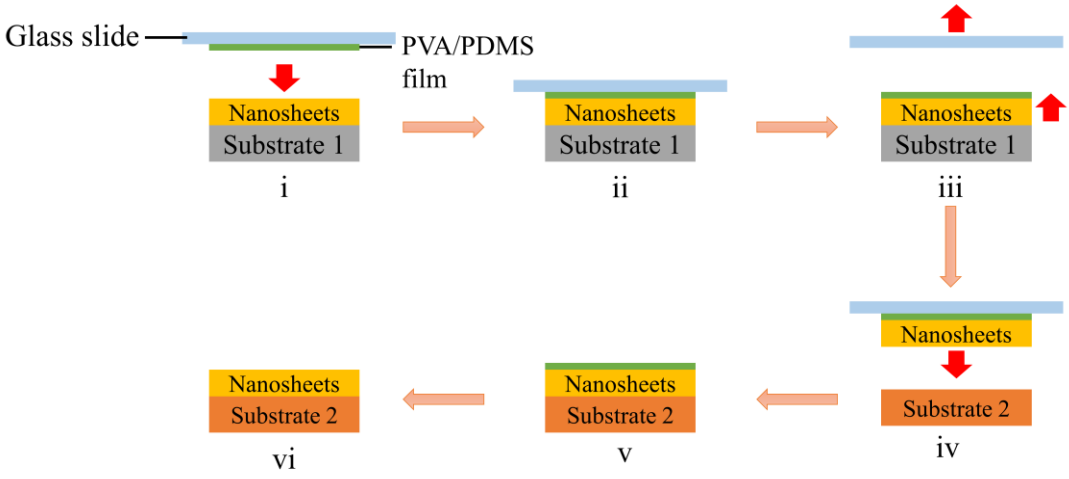

Figure 2.12 Schematic of dry transfer process.

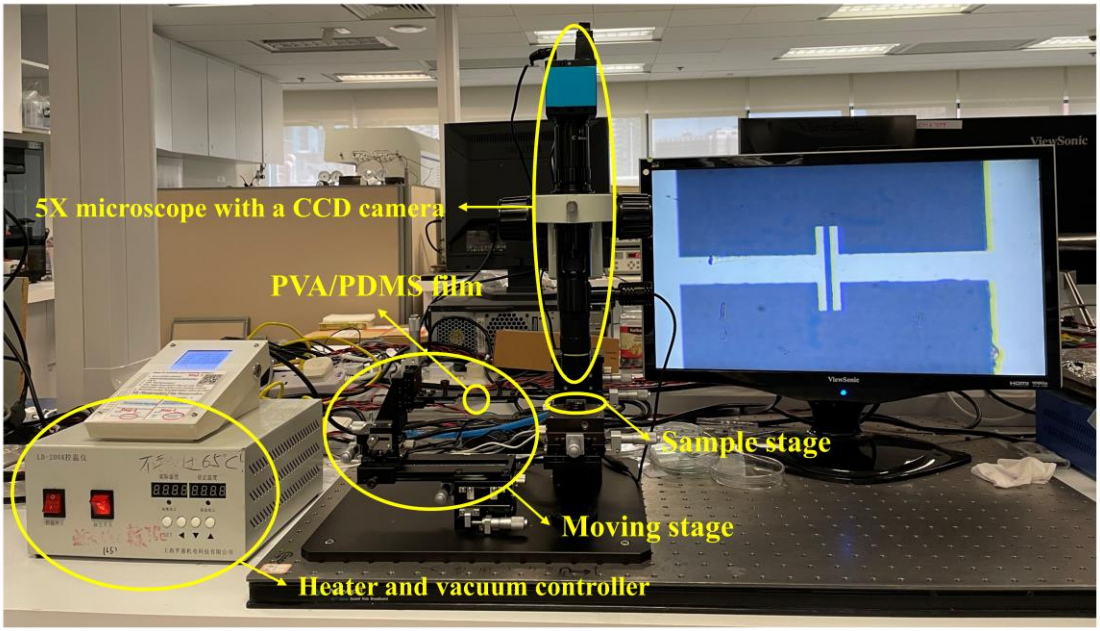

Figure 2.13 2D transfer platform system.

2.4.3 Electrical measurement

Electrical measurements were performed by a probe station with a Keithley 4200-

SCS semiconductor parameter analyzer. In order to investigate the piezotronic effect, uniaxial strains were applied onto the flexible piezoelectric nanogenerator (PENG) device by a custom-made fixing stage (Figure 2.14a).

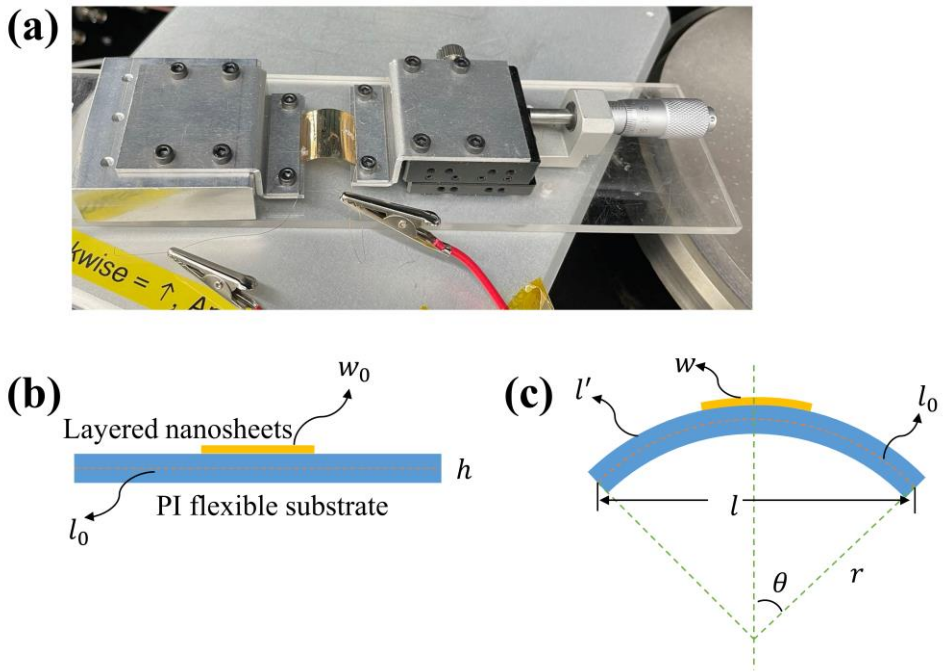

Figure 2.14 (a) The flexible piezoelectric device bent under a uniaxial strain by a fixed holder. (b) Initial state of nanogenerator. (c) Bending state of nanogenerator under mechanical stimuli.

The flexible device could be bent into an arc shape. The original length of the device is expressed as

$$l_0 = r \times 2\theta \tag{2-11}$$

Where r and θ are the radius and the angle of the initial arc, respectively. Then the length of the upper surface of the nanogenerator is given by

$$l' = \left(r + \frac{h}{2}\right) \times 2\theta \tag{2-12}$$

Since

$$sin\theta = \sin\left(\frac{l_0}{2r}\right) = \frac{l}{2r} \tag{2-13}$$

the applied strain could be

$$\varepsilon = \frac{(l' - l_0)}{l_0} = \frac{h}{2r} \tag{2-14}$$

A bending system was designed to facilitate periodic bending deformation of the flexible nanogenerators (as shown in the Figure 2.15). An oscillator (LeCroy WaveSurfer 62Xs) as well as a low-noise current preamplifier (Stanford Research Systems Model SR570), were utilized to analysis of the piezoresponse generated by the flexible device during the bending process. Due to the low-frequency and high-impedance signal sources, the input impedance is chosen to be 1 MΩ for impedance matching. A 10:1 high-impedance probe (standard oscilloscope probe) is used for probing output signals. To exclude the influence of the triboelectric effect on the observed piezoelectric behavior, a series of meticulously controlled experiments were conducted. The electrodes were maintained in stable and continuous contact with the sample to minimize interfacial friction, and mechanical deformation was applied through a uniaxial compressive force to prevent any relative sliding between the film and the electrodes. Additionally, polarity-switching tests and control experiments using pure PVA and pure PET films further confirmed that the output signals originated from the intrinsic piezoelectric response of samples themselves, rather than from triboelectric artifacts. The switched polarity test could be performed by exchanging the connection direction of the flexible nanogenerators.

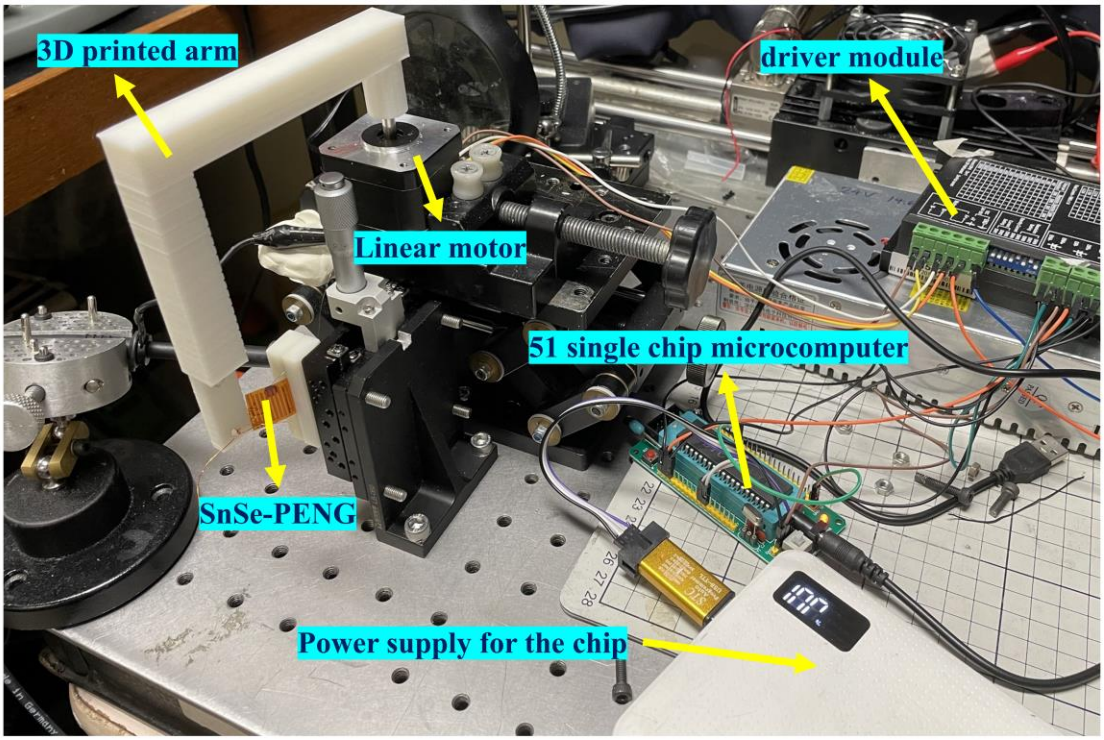

Figure 2.15 The setup for piezoelectric output measurement.

Chapter 3 Growth and characterization of SnSe nanosheets

3.1 Introduction

SnSe belongs to the family of IV-VI semiconductors and has gained considerable attention in materials science and solid-state physics due to its unique properties.[108] SnSe displays two distinct phases, including α-SnSe and β-SnSe. The atomic structure of α-SnSe is illustrated in Figure 3.1a, with two Sn-Se bilayers structured in orthorhombic lattice. SnSe exhibit varied behavior upon temperature fluctuations: As SnSe cools from its high-temperature phase (β-SnSe, Figure 3.1e) characterized by a higher symmetry space group *Cmcm* (No. 63), it undergoes a transformative displacive (shear) phase transition at approximately 750-800 K. This transition leads to the emergence of a lower symmetry phase represented by space group *Pnma* (No. 62) with lower symmetry.

The phase transition process involves the mode softening of the low-energy acoustic branch. This softening arises from the anharmonicity of the lattice, primarily driven by the orbital instability in SnSe. The $5s^2$ lone pairs of Sn are located in the non-bonding orbitals of the *Pnma* phase, resulting from hybridization with chalcogen *p*-states (Figure 3.1b). The lone pair is active and interacts with the *d* electrons of the surrounding Se atoms in the plane (bond d_3 in Figure 3.1b), pointing opposite d_1 in *Cmcm* and towards d_5 in *Pnma* (see the red "caps" in Figure 3.1c & g, respectively). As the temperature gradually rises, the equilibrium position of Sn gradually shifts towards

the center of the four Se atoms (Figure 3.1d). Upon reaching the phase transition temperature (T_c), SnSe undergoes a transformation into the *Cmcm* phase, wherein Sn locates itself at the midpoint of the four Se atoms with higher symmetry, as depicted in Figure 3.1h. However, the lone pair of $5s^2$ electrons of Sn causes a significant non-parabolic deviation in the potential distribution of Sn from the midpoint, giving rise to anharmonicity and phonon scattering. Therefore, the combination of the Sn lone-pair activity and the resonant Se *p*-bonding results in soft mode and Sn off-centering in the low temperature phase (Figure 3.1d). Conversely, at higher temperatures, the softening of lattice vibrations causes Sn to gradually approach the central position.[109] In this thesis, α-SnSe phase will be elaborated here due to its more stable feature than β-SnSe phase.

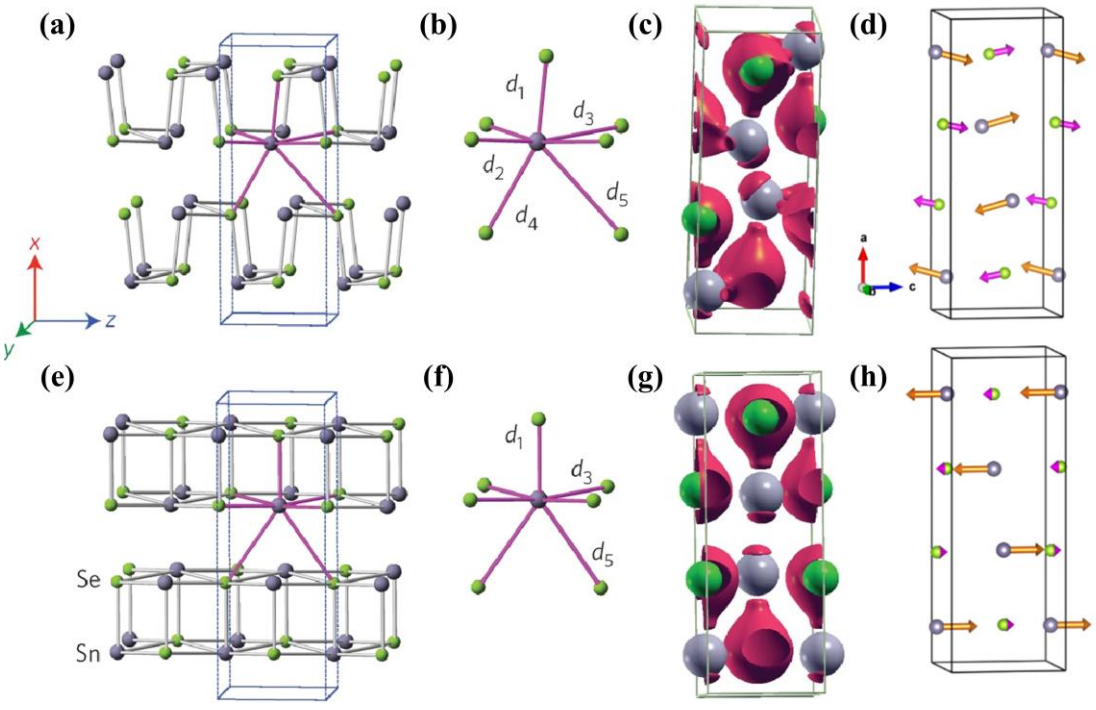

Figure 3.1 Schematic of structural distortion across the *Cmcm–Pnma* transition in SnSe and their corresponding electronic densities and atomic displacements. Layered α-SnSe

in *Pnma* phase (a) and β-SnSe in *Cmcm* phase (e). (b, f) The corresponding Sn coordination polyhedron in two phases. (c, g) Computational valence electron density for α-SnSe and β-SnSe, respectively. The atomic displacements during the phase transition between *Pnma* phase (d) and *Cmcm* phase (h).[109]

In addition to the extensive research conducted on the thermoelectric properties of bulk SnSe, researchers have delved into the exploration of SnSe thin films and nanosheets using various synthesis methods. These methods include molecular beam epitaxy (MBE),[110] magnetron sputtering,[111] liquid exfoliation,[76] one-pot method[112] and chemical vapor deposition.[113] However, it is worth noting that certain techniques necessitate special growth conditions and complex equipment. For instance, MBE requires a specialized system to grow materials under specific pressure and temperature conditions. Similarly, one-pot method requires multiple purification steps to obtain high-quality samples. Moreover, mechanical exfoliation has proven inadequate for obtaining large-size SnSe samples due to the relative high exfoliation energy of 151.8 meV/atom.[78] To enhance the crystallization of SnSe thin films, post-growth annealing processes are often employed to increase the structural integrity and film quality grown by magnetron sputtering. In contrast, chemical vapor deposition offers the advantage of scalability and controllability in the growth process, making it a promising technique for growing SnSe nanosheets.

In order to design appropriate growth parameters for the synthesis of crystalline SnSe, a thorough understanding of the fundamental thermodynamics of SnSe is

essential. Figure 3.2 displays the Sn-Se binary phase diagram, which offers useful information of the growth system and aids in parameter selection such as temperature, precursors, and pressure. The phase diagram reveals the formation of two intermediate phases, SnSe and $SnSe_2$, within the Sn-Se system. Notably, the melting point of SnSe (873.7 °C) is higher than that of $SnSe_2$ (646.6 °C), indicating that SnSe exhibits better thermal stability compared to $SnSe_2$. During the growth of single crystals, if the atomic percentage of Se ranges between 60 at. % and 66 at. %, $SnSe_2$ begins to precipitate as the temperature decreases below 646.6 °C. As the temperature continues slowly cooling down to 613 °C, this system reaches a eutectic point (60 at. %), resulting in simultaneous precipitation of SnSe and SnSe2. These two phases interlace with each other, forming layered structures. In the case where the atomic percentage of Se is between 50 at. % and 60 at. %, SnSe is formed prior to reaching the eutectic point. Subsequently, SnSe and $SnSe_2$ eutectics precipitate at 629°C. It should be noted that the SnSe formed at this temperature is in the high-temperature *Cmcm* phase. As the temperature further decreases to 520.2 °C, a phase transition occurs in the crystalline structure, leading to the transformation into the low-temperature *Pnma* phase. As the atomic ratio of Se is between 44 at. % and 50 at. %, SnSe precipitates as the temperature decreases from the melting point. The peritectic point is encountered when the temperature reaches 832 °C. As the system continues to cool down, SnSe also precipitates gradually, leading to an increase percentage of excess Sn in the melt. As the cooling process continues, the Se component will be fully consumed, and Sn will

precipitate on the surface of SnSe once the temperature falls below the melting point. Similarly, SnSe will experience the phase transition into α phase at temperature below 526.3 °C. It should be noted that α-SnSe exhibits stoichiometric composition, whereas β-SnSe could dissolves excess Se. Based on the Sn-Se phase diagram, it is advisable to maintain the Sn content slightly higher than 50 at. % during the SnSe growth. This ensures the avoidance of the $SnSe_2$ eutectoid phase. Additionally, careful control of the substrate temperature is necessary to prevent the formation of a mixture of $SnSe_2$ and SnSe phases. It is important to approach the synthesis of crystalline SnSe with careful consideration of these thermodynamic aspects. Understanding the precipitation behavior and phase transitions allows for precise control over the growth parameters, ensuring the desired crystal composition and structure are achieved.

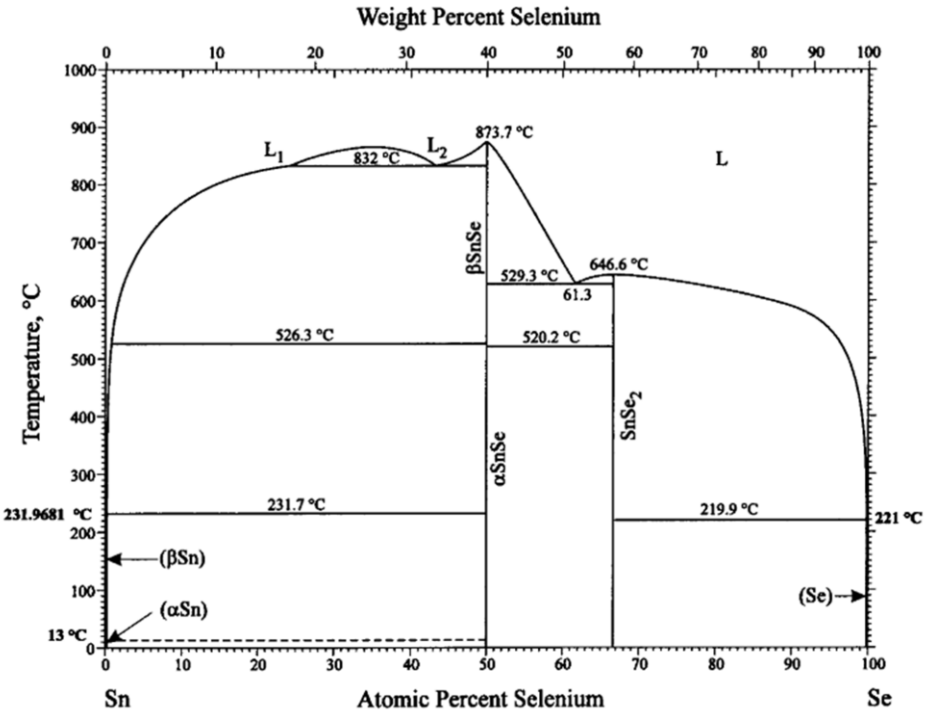

Figure 3.2 The phase diagram of Sn–Se.[114]

3.2 Growth process

In this thesis, the SnSe nanosheets were synthesized by vapor transport deposition method. The experimental setup for the deposition system is depicted in Figure 3.3. SnSe powders (99.999%, Alfa Aesar) were used as precursors, and N_2 served as the carrier gas. Mica substrates (12 × 12 mm^2) were freshly cleaved. The reason for choosing mica for substrate is its dangling-bond-free and atomically smooth surface, facilitating uniform growth. According to the growth temperature of SnSe nanosheets, the substrates were facing-up positioned at the downstream of the furnace, with a distance of 10–12.4 cm to the center of the furnace. The SnSe powders were first ground thoroughly and put into a quartz boat at the center of the chamber.

Prior to the deposition process, the pressure inside the furnace was initially reduced to approximately 1×10^{-2} Pa. Subsequently, N_2 was introduced to the quartz tube to purge any residual air or contaminants, continuing purging until to reach the atmospheric pressure. This meticulous flushing procedure ensured a clean and controlled growth environment conducive to the synthesis of high-quality layered SnSe. During the growth, the temperature of the furnace was steadily increased to 670-750 °C over a period of 30 minutes. Once the desired temperature was reached, it was maintained for 3-10 minutes to facilitate the growth of layered SnSe nanosheets. The growth environment was maintained with a N_2 flow rate of 50 standard cubic centimeters per minute (sccm). Subsequent to the designated time, the chamber was left to cool down naturally to room temperature.

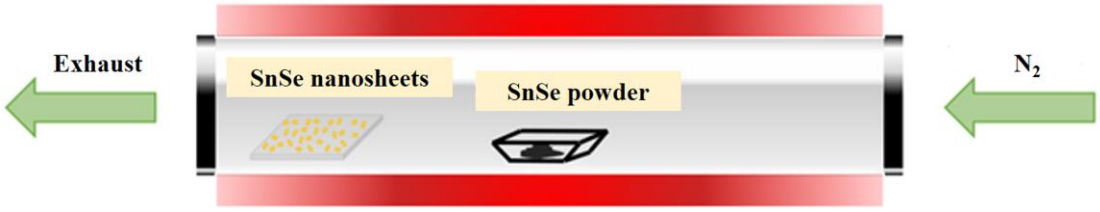

Figure 3.3 The vapor transport deposition setup for SnSe nanosheets growth.

The lateral dimensions and thickness in SnSe nanosheets could be optimized by cautiously adjusting the growth parameters. Here the influence of growth temperature, growth time, distance between the precursor and substrates, and the introduction of H_2 gas on the lateral size and thickness were investigated. During the deposition process, a controlled distance was maintained between the furnace center and the mica substrates. An electric thermometer was employed to record the temperature variation across different positions of the substrates positioned downstream of the chamber. The measurements indicated a temperature gradient of approximately 5 °C/cm. From the previous results, the temperature needs to be controlled ranging from 540 to 570 °C.[115]

As demonstrated in Figure 3.4, as the growth time increased, the as-prepared samples became thicker due to the accumulation of nuclei on the surface of the SnSe nanosheet. Higher growth temperature resulted in increased growth rates, leading to the formation of thicker SnSe nanosheets. The thickness would exceed 100 nm when the growth temperature is higher than 700 °C. Furthermore, the introduction of H_2 gas had an additional impact on the thickness of the SnSe nanosheets. A mixed gas of 10 sccm H_2/Ar (5%/95%) was introduced into the quartz tube during the growth time when the desired growth temperature was reached (Figure 3.4a). The strong binding energies

between the edge structures of the SnSe nanosheets and H_2 promoted vertical growth.[78] Consequently, thin SnSe nanosheets were favored to form at relatively short growth times and low temperatures without the introduction of H_2.

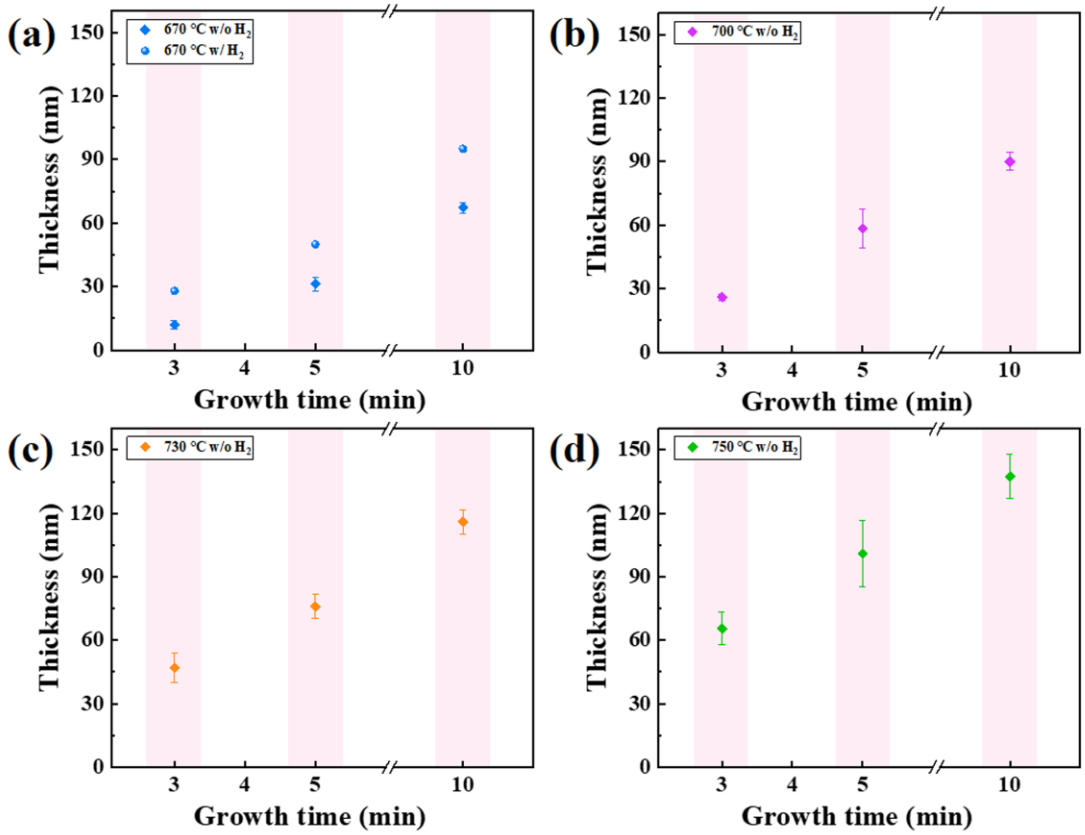

Figure 3.4 Thickness control of SnSe nanosheets under different growth conditions. The thickness results of SnSe nanosheets are collected at the mica substrates located at 11.2 cm away from the center of the furnace with 50 sccm N_2.

As for the lateral size, it could reach up to 50 μm as the deposition temperature was increased, suggesting a positive correlation with the growth temperature, as demonstrated in Figure 3.5a. This observation is consistent with the previously reported results.[113, 116] Positioning the substrate further from the center of the furnace resulted in smaller lateral dimensions and thicknesses of the SnSe nanosheets. However, according

to the Sn-Se phase diagram, the $SnSe_2$ would be also synthesized during the cooling stage. It could be found that the hexagonal $SnSe_2$ nanosheets would be obtained at the distance is further than 12.4 cm (Figure 3.5b). As shown in Figure 3.5c, two extra blue-marked Raman peaks correspond to E_g and A_{1g} mode of $SnSe_2$, which indicates the formation of a mixed phase of $SnSe_2$ at further distance. To avoid the appearance of SnSe-$SnSe_2$ mixture, the distance of the substrate and precursor would be controlled within 12.4 cm.

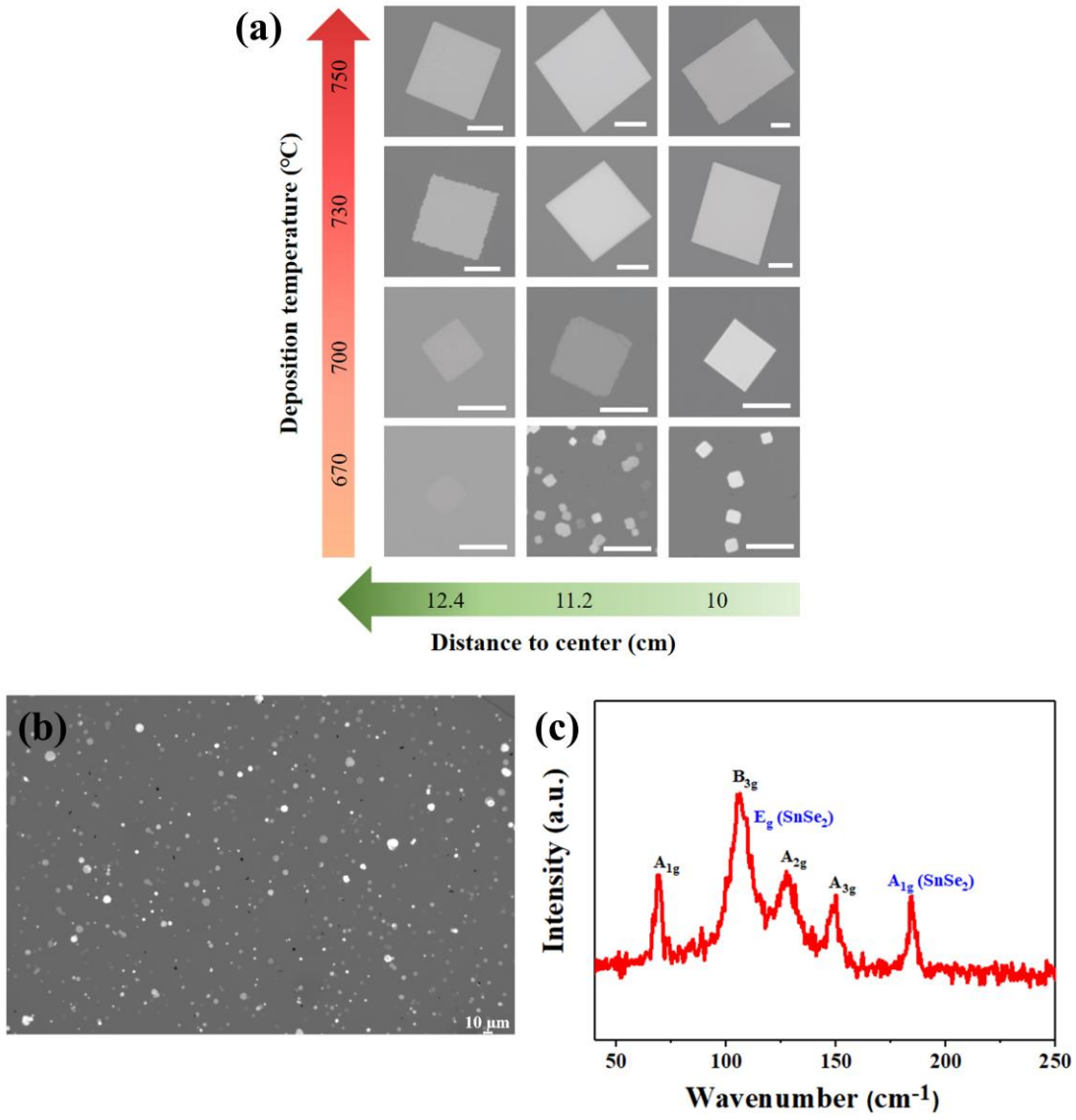

Figure 3.5 (a) Typical images of the as-prepared layered SnSe nanosheets with different

lateral size under different deposition temperature and positions. Scale bar: 10 μm. The distance refers to the separation between the center of the quartz tube and the mica substrates utilized for SnSe growth. A more pronounced contrast between the substrate and nanosheets suggests the presence of thicker SnSe nanosheets. (b) A typical image of the mixture of $SnSe_2$ and SnSe phases obtained at a distance further than 12.4 cm under 700 ℃ growth temperature and 50 sccm N_2 atmosphere. The hexagonal nanosheet is $SnSe_2$, showing different morphology from orthorhombic SnSe. (c) The obtained Raman spectra of mixture sample in Figure 3.5b.

3.3 Structure characterization

After the synthesis, the SnSe flakes were characterized using Raman spectroscopy, SEM, EDX, TEM, SAED, and SHG measurements to investigate their morphological and structural properties. The microscope images of the SnSe nanosheets are presented in Figure 3.6, showing predominantly square-shaped nanosheets. However, some nanosheets exhibited a square shape with a truncated corner, which can be attributed to differential growth rates on different surfaces. The (010) and (001) planes of the SnSe nanosheets vanished rapidly due to their large surface energy and rapid growth rate. As a result, only the (011) planes remained, leading to the characteristic square shape of the SnSe nanosheets.[117]

The Raman spectra depicted in Figure 3.7 exhibit four distinct peaks positioned at 32 cm^{-1}, 70 cm^{-1}, 105 cm^{-1} 127 cm^{-1} and 150 cm^{-1}. These peaks attribute to A_g^0 A_g^1, B_{2g}, A_g^2 and A_g^3, respectively, which are consistent with previous findings on SnSe

nanosheets.[118] No extra peaks appear in the Raman spectra, such as the peaks related to $SnSe_2$, proving that the as-prepared SnSe nanosheets exhibit pure α phase. Furthermore, the SEM image presented in Figure 3.8a indicates the surface uniformity and thickness consistency across the entire nanosheet. The corresponding elemental mapping images obtained through EDX analysis in Figure 3.8b-c reveal a homogeneous distribution of chemical elements and consistent composition within the SnSe layered nanosheets. The quantitative elemental analysis conducted on the EDX spectrum (Figure 3.8d) demonstrates an atomic ratio of Sn and Se that approximates 1:1, consistent with the stoichiometric composition of SnSe.

In order to confirm the non-centrosymmetric structure, SHG measurement was performed. Figure 3.9a displays a typical SHG spectra of SnSe flake on mica substrate under excitation of 900 nm. Notably, a distinct SHG peak at 450 nm indicates the intrinsic non-centrosymmetric nature of SnSe, suggesting its potential for applications in piezoelectric devices. The uniform SHG mapping exhibited in Figure 3.9b further confirms the high quality and uniform crystalline structure of the SnSe nanosheets.

To corroborate the microscopic structural properties of the SnSe nanosheets, HRTEM and SAED were employed, as shown in Figure 3.10. The resulting images reveal clear orthogonal lattice fringes, affirming that the single crystalline structures with high crystalline quality in layered SnSe nanosheets. The lattice spacing along the (011) and $(0\,\bar{1}\,1)$ directions measures to be approximately 3.0 Å. The measured intersection angle is approximately 93°.[117, 119] Based on these findings, the

morphological and structural analyses unequivocally demonstrate the uniform morphology and single-crystalline nature of SnSe nanosheets synthesized through the vapor transport deposition technique, facilitating further exploration of their physical characteristics and applications.

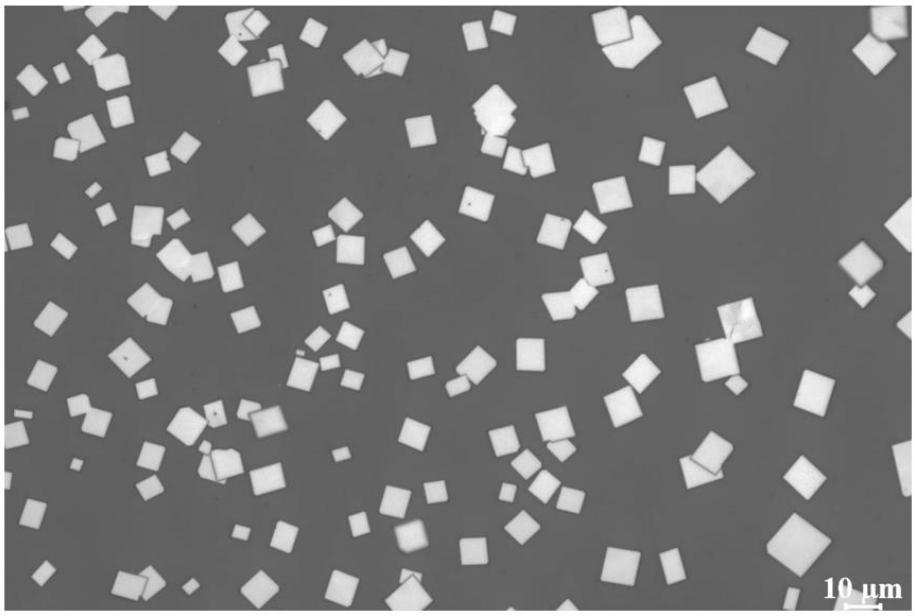

Figure 3.6 Optical image of SnSe nanosheets grown on mica.

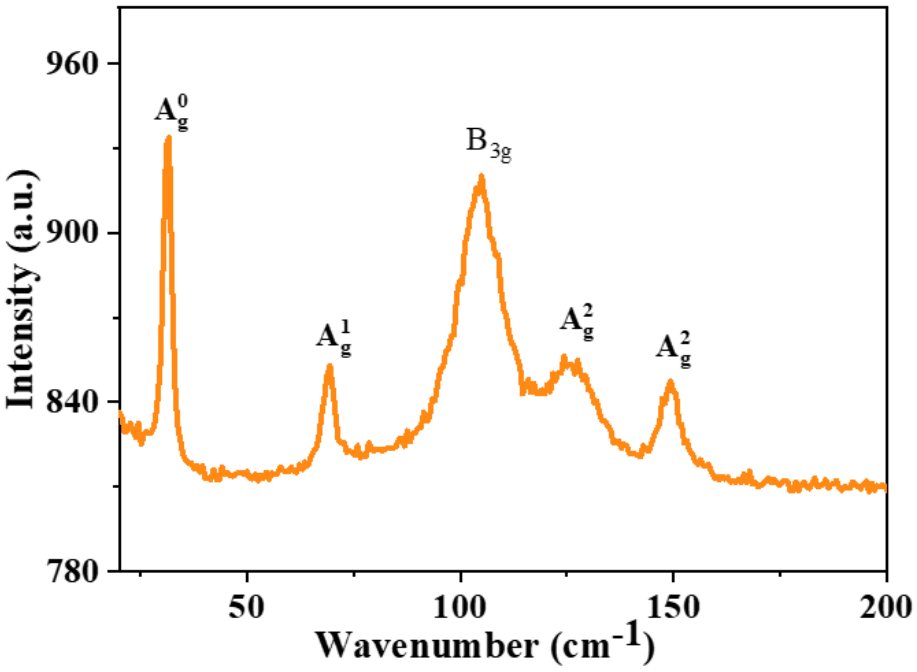

Figure 3.7 Raman spectra of SnSe nanosheets at 532 nm excitation.

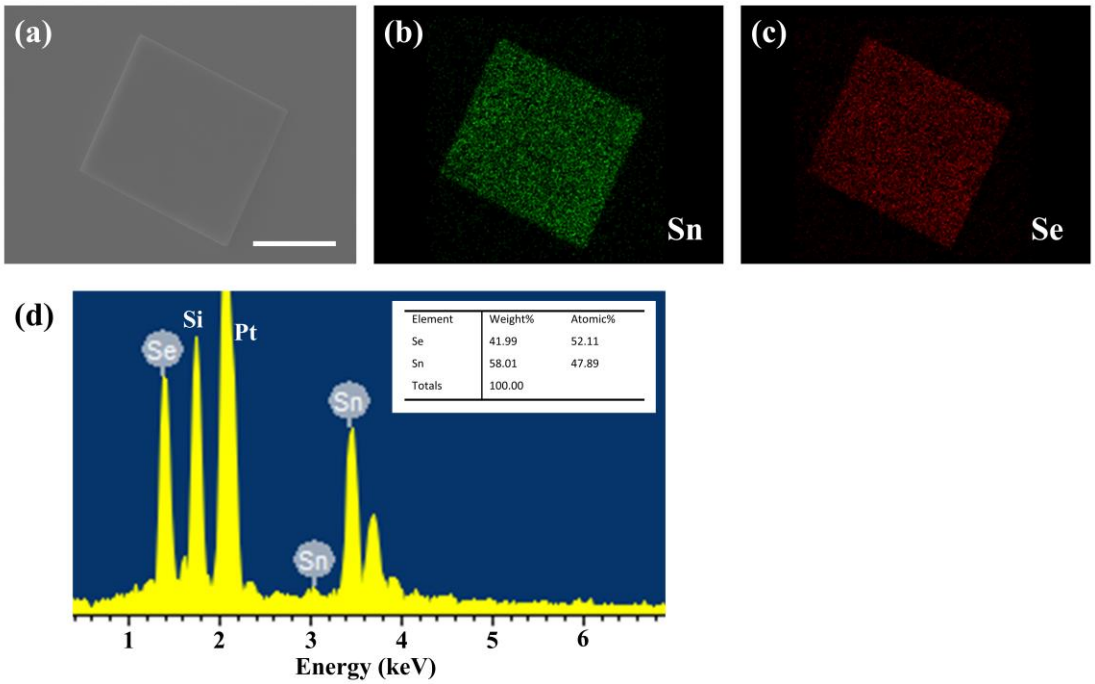

Figure 3.8 (a) SEM images of SnSe nanosheet. The corresponding EDX elemental mapping (b: Sn, c: Se) and EDX spectra (d) of the SnSe nanosheet.

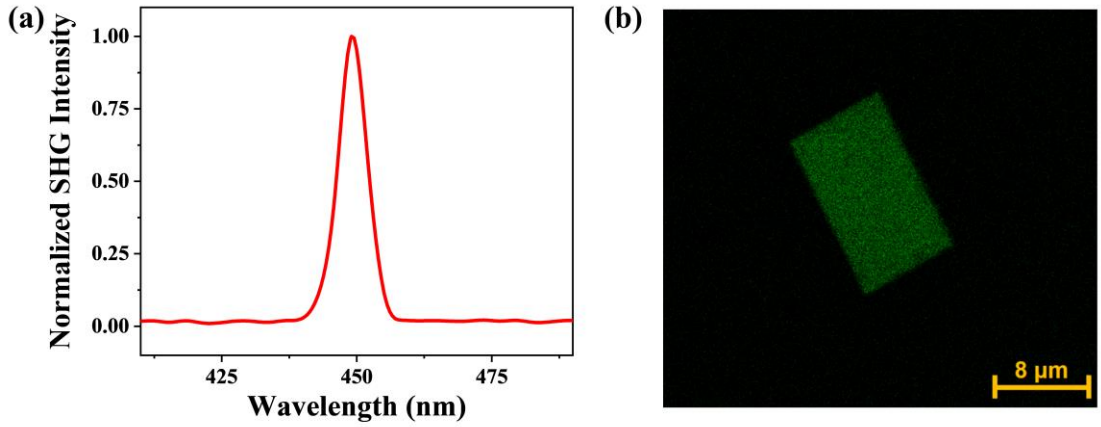

Figure 3.9 SHG spectra (a) and SHG mapping (b) from SnSe nanosheet.

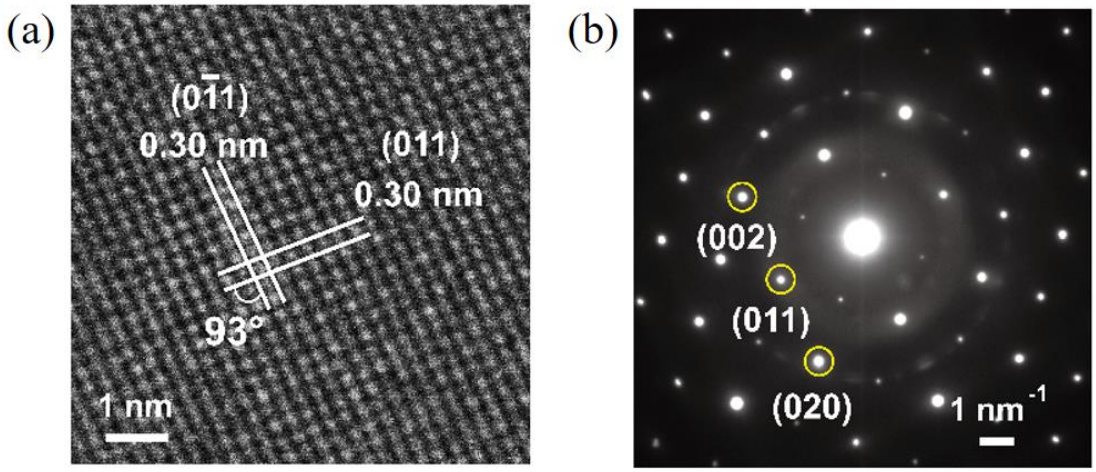

Figure 3.10 (a) HRTEM image and (b) The corresponding SAED pattern of SnSe nanosheets.

3.4 Summary

In summary, the synthesis and characterization of SnSe nanosheets using vapor transport deposition method was discussed. We established a growth system with SnSe powders as precursors, nitrogen gas as the carrier gas and mica as substrates, respectively. The growth parameters affecting the lateral dimensions and thickness of the nanosheets, such as growth temperature, time, distance, and the introduction of H_2 gas, are investigated. The structural characterizations of the synthesized SnSe nanosheets demonstrate their non-centrosymmetric and single-crystalline structure, facilitating novel possibilities for photonic and electromechanical coupling device design.

Chapter 4 Piezoelectric properties of SnSe nanosheets

4.1 Introduction

Due to the environmentally unfriendly nature of traditional energy sources, the demand for renewable energy continues increasing to meet the requirements of rapid urbanization and industrial growth. Alternative energy sources, such as solar, wind, tidal and nuclear energy, have emerged as substitutes for traditional fossil fuels. Furthermore, with technological advancements, there has been a rise in the popularity of portable smart devices. Harvesting energy from the surrounding environment is emerging as an efficient solution to address energy challenges. The emergence of piezoelectric materials, enabling to achieve the conversion between mechanical energy and electrical energy, has become significant and ubiquitous in the exploration of novel energy sources.[120]

Piezoelectric materials possessing polarization domains or non-centrosymmetric structures find extensive applications with electromechanical coupling, such as actuators, transducers and sensors. The discovery of piezoelectricity in quartz by Jacques Curie and Pierre Curie in 1880 laid the foundation for subsequent advancements.[121] Since then, a range of conventional piezoelectric ceramics (i.e. PZT and $BaTiO_3$) and semiconductors (i.e. ZnO and GaN) have exhibited remarkable piezoelectric performance, characterized by large charge constants, excellent mechanical durability, and suitability for industrial applications.[122] Nevertheless, in

certain application scenarios, such as wearable devices or bio-implantable electronics, piezoelectric materials must fulfill specific requirements, such as thinness, flexibility, and ambient stability. Conventional piezoelectric materials typically consist of brittle ceramics or certain polymers with low thermal stability, thereby impeding their innovative applications.

Recently, layered nanomaterials have arisen as a novel generation of piezoelectric materials, exhibiting distinct piezoelectric properties compared to their bulk counterparts. These layered materials offer numerous surprising advantages, encompassing their structure and electronic properties. For instance, molybdenum disulfide (MoS_2) demonstrates a direct band gap in its atomic layers, while it is indirect in its bulk form.[123] Moreover, the atomic thinness of layered materials facilitates their fabrication and simulation for practical device applications. By harnessing the strong piezoelectric effect and excellent electronic properties of these materials, they exhibit enhanced compatibility and ease of integration with integrated circuits and micro-electromechanical systems, surpassing the capabilities of conventional piezoelectric materials.

Among these various layered piezoelectric materials, group IV-VI monochalcogenides have been recognized for their significant intrinsic in-plane piezoelectric properties, making them highly promising for achieving efficient energy conversion in practical piezotronic applications. They could be expressed as MX, here M denotes Sn or Ge, X represents Se or S. Their unique piezoelectric coefficient d_{11}

(ranging from 75.43 to 250.58 pm/V) originates from their distinctive puckered C_{2v} symmetry due to the repulsion of lone pair electrons.[42] Within this group, SnSe stands out because of its exceptional electrical and mechanical properties, which make it particularly well-suited for electromechanical coupling systems.

Recent advancements have been made in utilizing SnSe flakes obtained through mechanical exfoliation as piezoelectric nanogenerators to drive MoS_2 multi-functional sensors.[124] Additionally, SnSe nanowall/microspheres synthesized by a solution-mediated process have demonstrated a large in-plane piezoelectric coefficient of 19.9 pm/V.[125] However, this synthesis method faces challenges in obtaining defect-free single-crystalline structures, which can impede carrier transport in piezotronic devices.

In contrast, the vapor transport deposition technique offers multiple advantages, including scalability, controllability, and mass production capability, facilitating the synthesis of high-quality, large-area single-crystalline layered materials. These advantages make it a highly favored technique for industrial-scale production and the development of practical devices.[80] In this chapter, SnSe nanosheets have been investigated for their intrinsic piezoelectric properties at the nanoscale using piezoresponse force microscopy (PFM) techniques. These layered SnSe nanosheets have been successfully fabricated into piezoelectric nanogenerators for energy harvesting and human-motion monitoring.

4.2 Piezoelectric properties

The thickness-dependence in-plane piezoelectric properties of layered SnSe

nanosheets were investigated by PFM techniques, providing insights into the electromechanical coupling properties of piezoelectric and ferroelectric materials. The lateral piezoresponse signals were collected in Vector mode. In order to quantitatively obtain the piezoelectric coefficient d_{11}, a calibration step was performed using monolayer MoS_2, which was synthesized on the SiO_2/Si substrate by a conventional atmospheric pressure vapor transport deposition process.[126] Before PFM measurement, we characterize the as-prepared MoS_2 nanosheets first. As demonstrated in Figure 4.1a, the height of the as-prepared MoS_2 sample is estimated to be 0.9 nm, which consistent to theoretical value of single-layer MoS_2.[127] Additionally, the Raman spectra (Figure 4.1b) demonstrates two distinguishing peaks located at 384 cm^{-1} and 403cm^{-1}, corresponding to the in-plane vibration of Mo with respect to S atoms (E^1_{2g}) and the out-of-plane vibration of S atoms (A_{1g}), respectively. The frequency difference between these vibration modes confirmed the presence of a single layer of MoS_2.[128] After confirmation of thickness and single-crystalline of MoS_2, PFM measurements were conducted as demonstrated in Figure 4.1c-d. It could be seen that the piezoresponse behavior of the monolayer MoS_2 revealed a significantly stronger response compared to the substrate. The lateral piezoelectric amplitude increases linearly with the applied drive voltages. The slope obtained for the monolayer MoS_2 is approximately 14.70×10^6 arbitrary units V^{-1}. According to a previous report, the effective piezoelectric coefficient d_{11} for monolayer MoS_2 is 3.78 pm V^{-1}.[69] Consequently, the effective d_{11} of SnSe with various thicknesses can be calculated by dividing the slope by the d_{11} value

of the monolayer MoS_2.

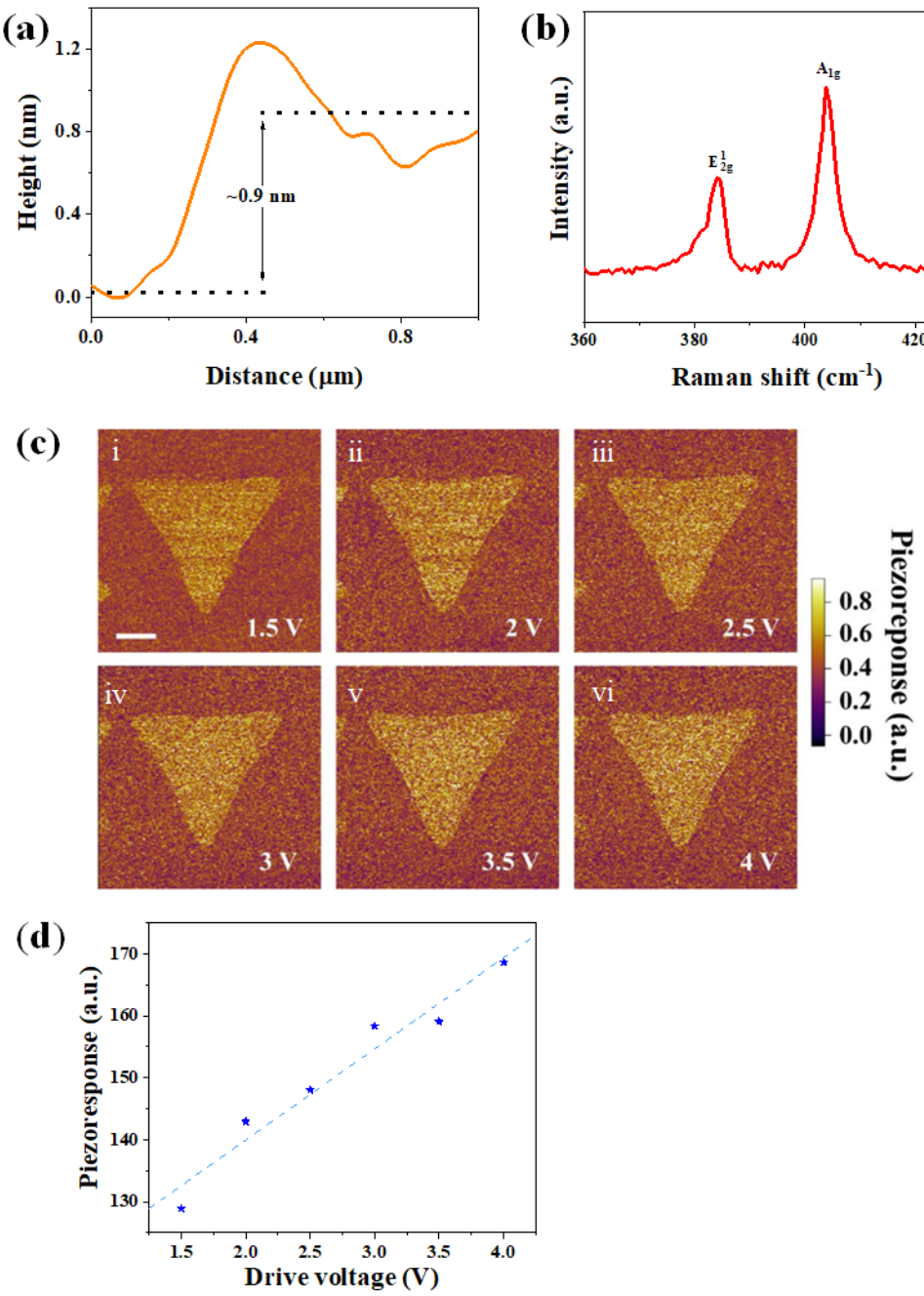

Figure 4.1 Characterization of CVD-grown monolayer MoS_2 for PFM calibration. (a) The height profile. (b) Raman spectra. (c) Piezoresponse amplitude images obtained at various voltages ranging from 1.5 V to 4 V. (d) The lateral piezoelectric amplitude as a function of drive voltage. The lateral piezoelectric amplitudes were extracted by the

difference between the amplitudes of MoS_2 and substrate. The dashed line represents the fitted linear curve from these amplitude results accordingly.

The lateral amplitude signals exhibited by SnSe nanosheets (ranging from 10 nm to 120 nm) under driving voltages from 1.5 V to 3 V, are depicted in Figure 4.2 to Figure 4.4, respectively. Clearly, these SnSe nanosheets display high lateral amplitudes, confirming that the observed piezoresponse originates primarily from the SnSe layered nanosheets instead of the substrate with negligible response. The distinct difference in piezoresponse between the SnSe layered nanosheets and the substrate underscores intrinsic in-plane piezoelectricity displayed by the as-prepared SnSe samples. Besides, the effective amplitude could be extracted by the amplitude signals difference between those of the SnSe samples and substrates. Based on the amplitude-voltage curve, the lateral PFM amplitudes of SnSe nanosheets exhibit a linear dependence on the applied drive voltages. As a result, the effective d_{11} of SnSe layered nanosheets with varying thicknesses can be inferred from the slope of these linear curves. The d_{11} outcomes for SnSe with different thicknesses are illustrated in Figure 4.5a. Notably, for thinner SnSe nanosheets, the d_{11} value progressively rises with increasing thickness, suggesting a gradual improvement in piezoresponse as the SnSe thickness increases. This trend aligns with previously-reported phenomena in other layered piezoelectric/ferroelectric materials like PZT films, α-In_2Se_3 and $CuInP_2S_6$ nanoflakes.[72, 129, 130] This behavior can be attributed to decreasing constraint arising from substrate clamping effect, which becomes negligible for thicker nanosheets.

A comparative analysis of experimental-derived in-plane piezoelectric coefficients across different layered piezoelectric materials was also conducted, as summarized in Figure 4.5b. Remarkably, the d_{11} value of the 10 nm SnSe nanosheet (~45.82 pm/V) is nearly double that of single-layer SnS within the group IV-VI monochalcogenides, and exceeds those of monolayer MoS_2 and WSe_2 by an order of magnitude.[57, 69] It reveals that multilayer SnSe exhibit a greater sensitivity to mechanical deformations, allowing for various applications, such as sensors that detect pressure, strain, or vibrations. The piezoelectric improvement in SnSe layers derives from the essential C_{2v} symmetry, which shows smaller elastic stiffness of both clamp-ion and relax-ion compared to the D_{3h} symmetry piezoelectric materials whose covalence bonds are much stronger.[42] Moreover, SnSe nanosheets grown by vapor transport deposition exhibit good crystalline quality and low defect density, providing efficient carrier transportation with less scattering. Consequently, it could be seen that the in-plane piezoresponse of SnSe nanosheets is at least two times stronger than those of mechanically exfoliated SnSe films as well as $Sn_{(1-x)}Se_x$ nanowall/μ-spheres.[124, 125] The robust piezoresponse observed in SnSe nanosheets highlights their significant potential for practical piezoelectronic applications.

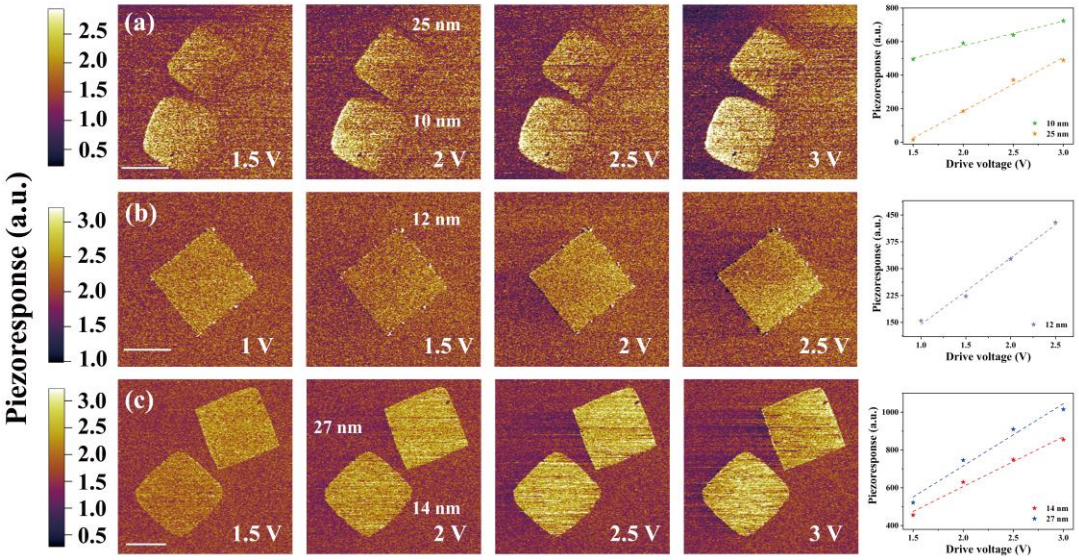

Figure 4.2 The piezoresponse of relatively thin SnSe nanosheets. (a) 10 and 25 nm. (b) 12 nm and (c) 14 nm and 27 nm. Scale bar: 5 μm.

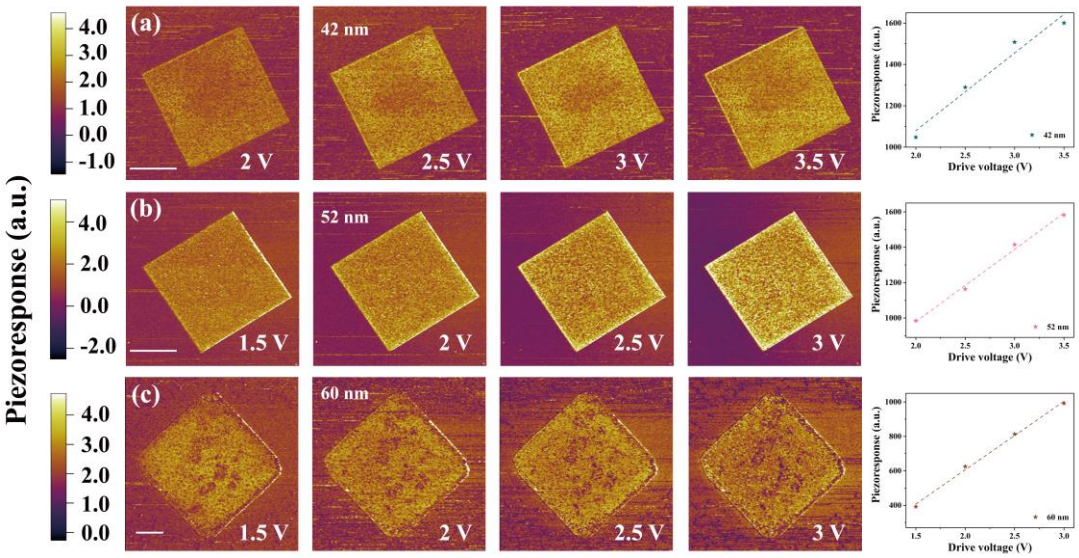

Figure 4.3 The piezoresponse of SnSe nanosheets with moderate thickness. (a) 42 nm, (b) 52 nm, and 60 nm. Scale bar: 5 μm.

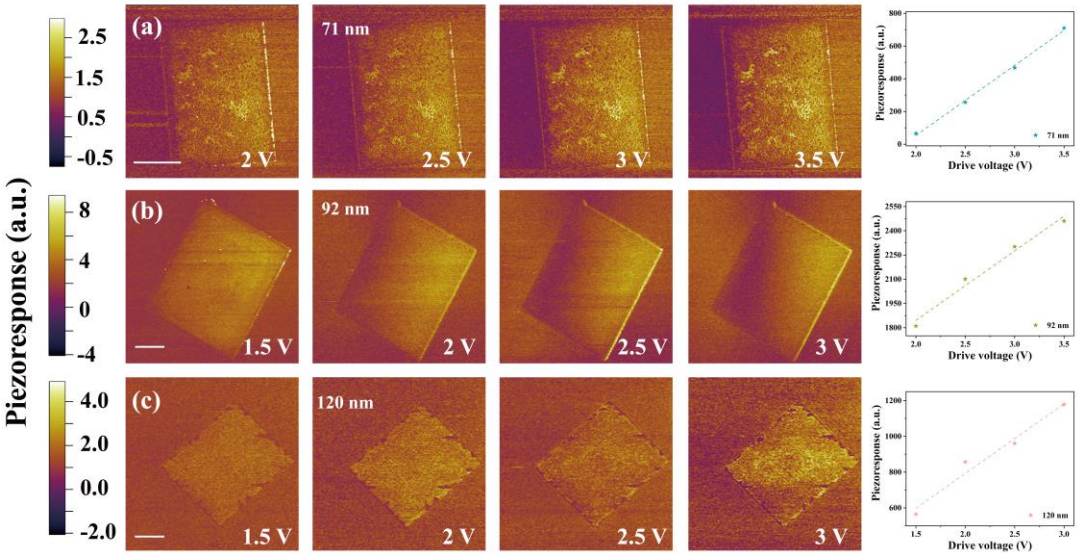

Figure 4.4 The piezoresponse of relatively thick SnSe nanosheets. (a) 71 nm, 92 nm, and 120 nm. Scale bar: 5 μm.

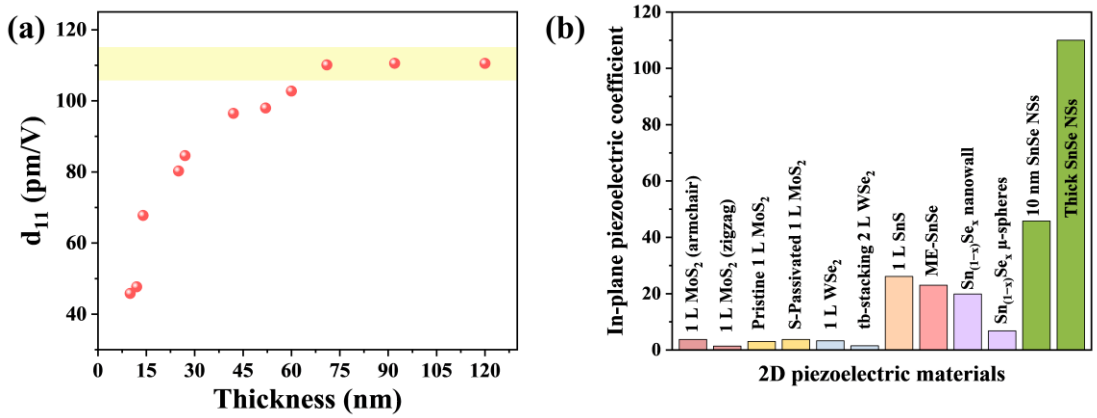

Figure 4.5 (a) d_{11} of SnSe layered nanosheets with different thicknesses. (b) Summary of experimental-confirmed in-plane piezoelectric coefficients.[54, 57, 68, 69, 124, 125]

4.3 Piezotronic effect

In order to perform the direct-current electrical characterization and measure the piezoelectric output performance, the SnSe layered nanosheet was integrated into flexible piezoelectric nanogenerator (SnSe-PENG). The structure of the SnSe-PENG is illustrated in Figure 4.6a. Ti/Au electrodes (5/50 nm) were prepared on 125 μm-thick

flexible PI substrate by standard photolithography and metallization. SnSe was transferred to the electrodes by dry-transfer method. The electrodes were linked to two copper wires with sliver paste. As shown in Figure 4.6b, ~60 nm SnSe nanosheet was transferred onto the device. During the direct-current electrical characterization, a holder (Figure 2.14a) was used to apply different uniaxial strains onto SnSe sample.

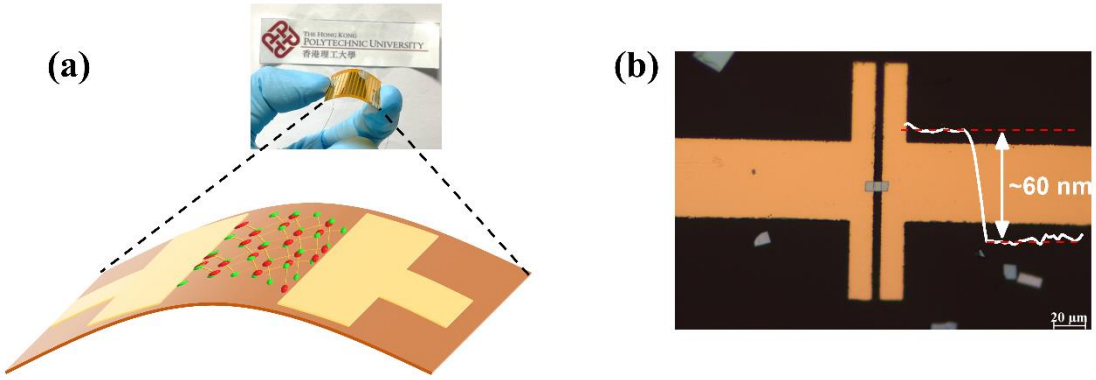

Figure 4.6 (a) Structure of SnSe-PENG device. (b) The optical image of SnSe-PENG. Inset: the height profile of SnSe between the electrodes.

The obtained I-V curves are demonstrated in Figure 4.7. The nonlinear curves reveal the Schottky contacts in the metal-semiconductor junctions. With increasing strain, the I-V curves demonstrate upward and downward shifts under compressive and tensile strains, respectively. The distinct asymmetric change in current at -1 V and 1 V under uniaxial strains is ascribed to the piezotronic effect in SnSe. Upon the application of uniaxial strain, the elongation of Sn-Se bonds transpires due to the inherent non-centrosymmetric distortion of SnSe. This elongation leads to the generation of a piezoelectric dipole and field. When it comes to multilayer structures, the distinct piezoelectricity exhibits in both odd and even layers of SnSe, disregarding possible

cancellation between two adjacent layers. This behavior is analogous to BP with the similar puckered structure.[131] These intriguing symmetries of SnSe render it more flexibilities compared to D_{3h} symmetry piezoelectric materials (such as MoS_2 and WS_2), whose piezoelectricity only exists in the odd layers.

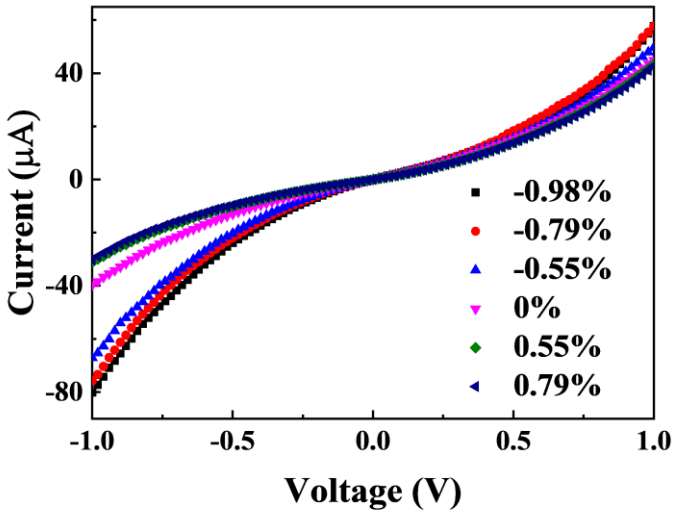

Figure 4.7 The I-V curves under different strains.

The band diagrams in Figure 4.8 provide a clear illustration of how the Schottky barrier height (ΔE_p) varies under different stress conditions in SnSe. When the SnSe lattice experiences deformation in response to mechanical stimuli, piezoelectric polarization charges will be accumulated at the Schottky interfaces. Specifically, the positive polarization charges attract electrons towards the interface, effectively reducing the depletion region and consequently decreasing the Schottky barrier height. Conversely, the negative polarization charges repel electrons from the interface, causing additional depletion at the interface and an elevation in the Schottky barrier height. The asymmetric accumulation of piezoelectric polarization charges at the source

and drain of the SnSe device gives rise to an asymmetric Schottky barrier height, which in turn leads to an asymmetrical variation in current. This asymmetric control over carrier transport resembles a transistor-like behavior, with the SnSe nanosheet serving as a control gate.[53, 132] The piezoelectric potential produced by the strain can be utilized to differentially modulate carrier transport. The high current observed in these devices indicates a favorable contact between the SnSe flakes and the electrodes, ensuring efficient charge transport. The distinct piezotronic behavior exhibited by SnSe nanosheets highlights their promising potential for application in practical flexible piezotronic devices.

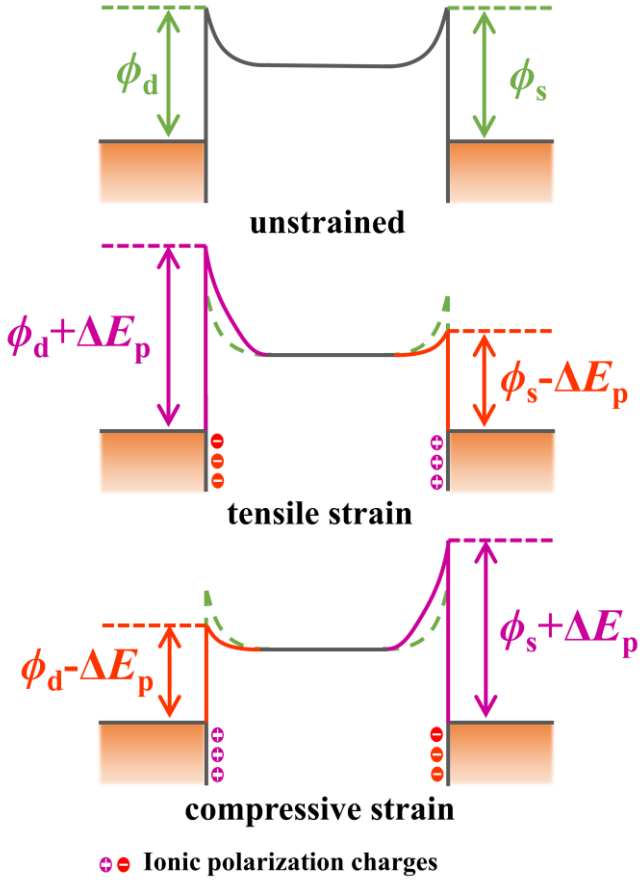

Figure 4.8 Band diagrams of piezotronic effect in SnSe nanosheets under tensile strain and compressive strain. The symbols ϕ_d and ϕ_s is the Schottky barrier heights at the

drain and source, respectively. ΔE_p represents the change in the Schottky barrier height caused by the presence of piezoelectric polarization charges.

4.5 Electrical properties

To further investigate the electrical properties of SnSe layered nanosheets, field-effect-gating devices were developed based on SnSe nanosheets. The as-prepared SnSe nanosheets were first transferred onto 300 nm SiO_2/Si substrate by wet transfer method. Then the 50 nm Au electrodes and h-BN were then transferred by dry transfer method respectively. The optical image of SnSe-based field-effect-gating devices is shown in Figure 4.9. The Raman spectra showing clear characteristic peaks in Figure 4.10 confirms the co-existence of SnSe and h-BN in the device structure. The thickness of SnSe and h-BN is measured to be ~33 and 25 nm, respectively, as demonstrated in Figure 4.11.

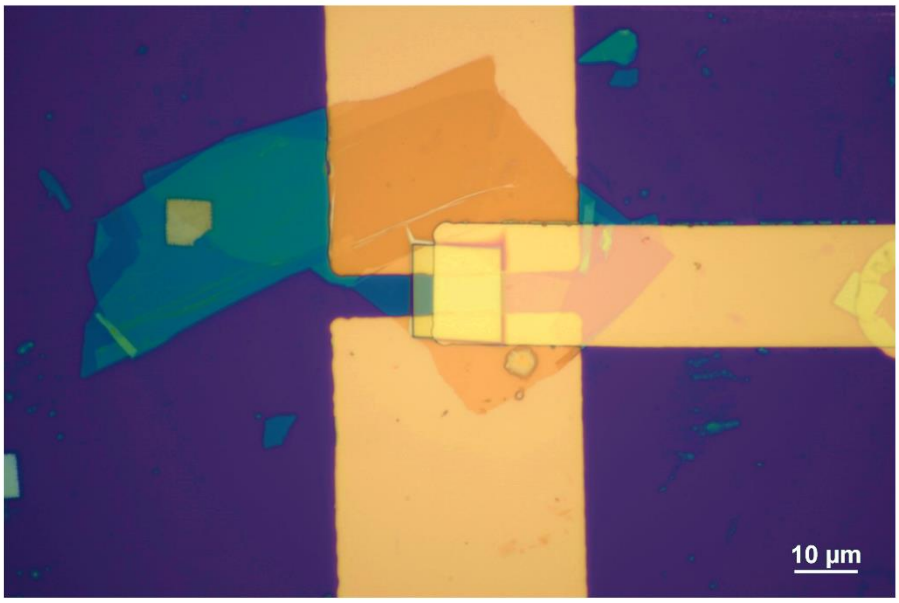

Figure 4.9 The optical image of SnSe-based field-effect-gating devices.

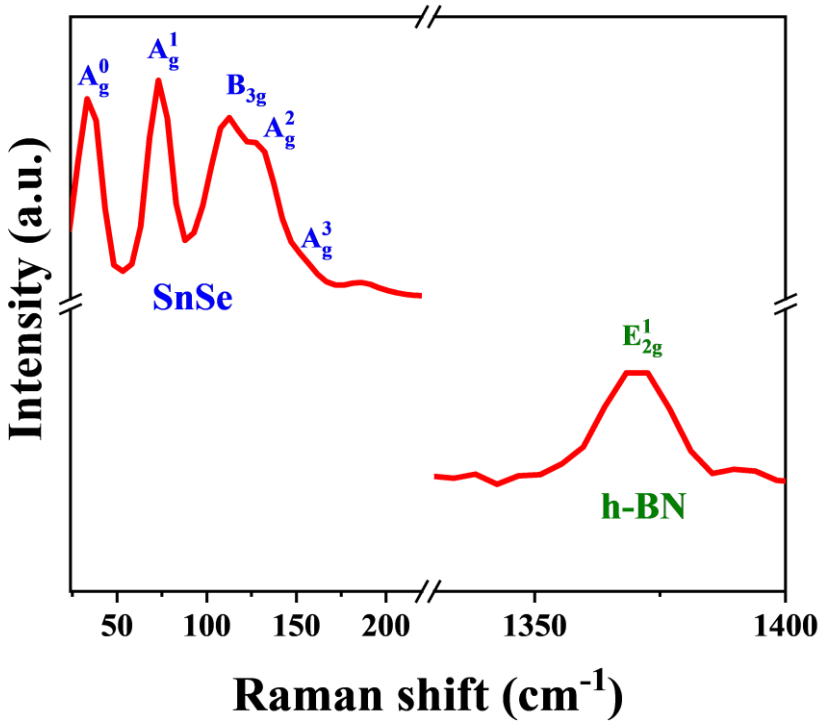

Figure 4.10 Raman spectra of the SnSe (left) and h-BN (right).

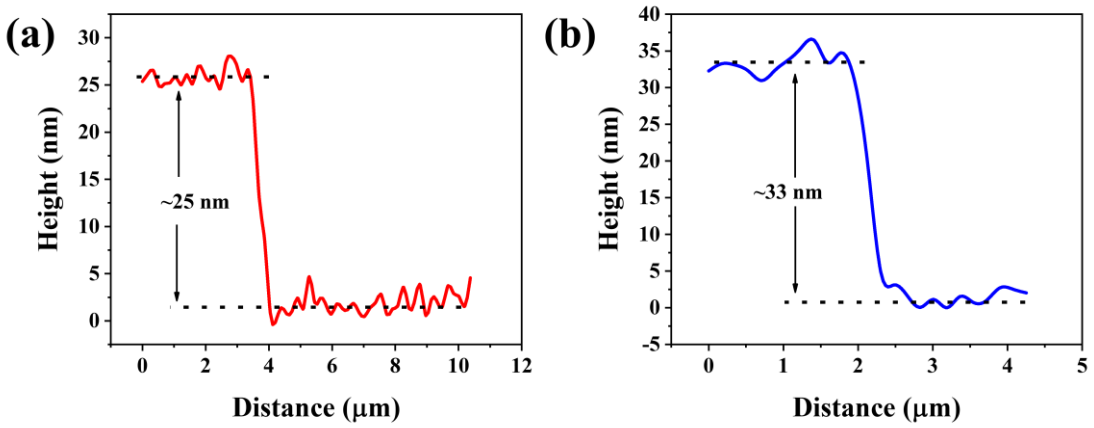

Figure 4.11 The AFM height profiles of h-BN (a) and SnSe nanosheet in the field-effect-gating devices.

The electrical transport properties were measured with a semiconductor parameter analyzer (Keithley 4200). As for the back-gate field-effect-gating device, linear output curves (I_{ds}–V_{ds}) in Figure 4.12 reveal that Ohmic contacts are formed between SnSe

and metal electrodes. In the transfer characteristic curve, the drain current falls during a positive V_g scan, presenting the clear p-type transfer characteristics. The carrier mobility could be measured to be ~19.35 $cm^2 V^{-1} S^{-1}$, using the equation

$$\mu = \frac{dI_{ds}}{dV_g} \times \frac{L}{WC_g V_{ds}} \quad (4\text{-}1)$$

where W = 10.47 μm is the channel width, L = 6 μm is the channel length and C_g is the capacitance between the channel and the gate per unit area ($C_g = \varepsilon_0 \times \varepsilon_r / d$; $\varepsilon_0 = 8.85 \times 10{-}^{12}$ $F \cdot m^{-1}$, $\varepsilon_{SiO2} = 3.9$; d = ~300 nm). The obtained mobility is higher than that of bottom-gate CVD-grown SnSe FET on SiO_2/Si substrates.[113, 133]

The interface between layered nanosheets and typical dielectric materials, such as SiO_2 and Al_2O_3, poses challenges to device performance. Specially, the absence of dangling bonds on the surface of layered nanosheets hinders conformal coatings and leads to multiple defects at the interface, which will increase the leakage currents in gate, hysteresis effects, subthreshold swing as well as threshold voltage fluctuation. One possible solution to this issue is to use the appropriate gate dielectric, for example h-BN. By forming a defect-free van der Waals interface with the layered nanosheets, layered h-BN can enhance device performance, particularly by increasing channel mobility.[15] In addition, h-BN offers advantages such as low leakage currents (less than 10 A/cm^2 at 0.6 V for a 1.3 nm thick stack) and high dielectric strength (~ 21 MV/cm for 3 nm-thick).[134, 135]

Therefore, the output performance of top-gate field-effect-gating device with h-BN as dielectric was also investigated. From Figure 4.13, it could be found that the output

behavior of the top-gate field-effect-gating device is similar to that of the back-gate device, showing clear p-type transfer behavior. The hole mobility in the top-gate field-effect-gating device is measured to be ~ 9.08 cm^2 V^{-1} S^{-1} (here, $\varepsilon_{h\text{-}BN}$ = 3.5[15]). These two devices demonstrated low leakage current (small I_{gs}) during the V_g scanning, which is crucial for low-power applications.

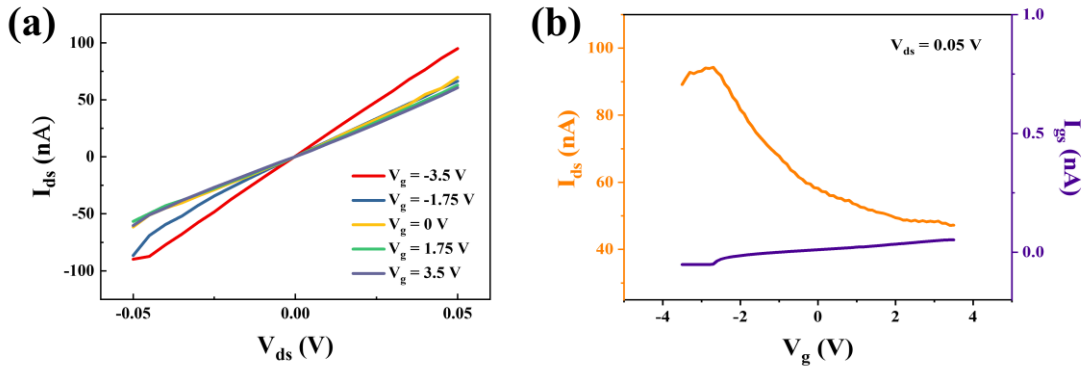

Figure 4.12 Electrical properties of back-gate field-effect-gating device based on SnSe nanosheets. (a) The output curves (I_{ds}–V_{ds}) of the SnSe FET device measured at different gate voltages with a step of 1.75 V. (b) Transfer characteristic curve of the device at V_{ds} = 0.05 V, while the I_{gs} was also recorded.

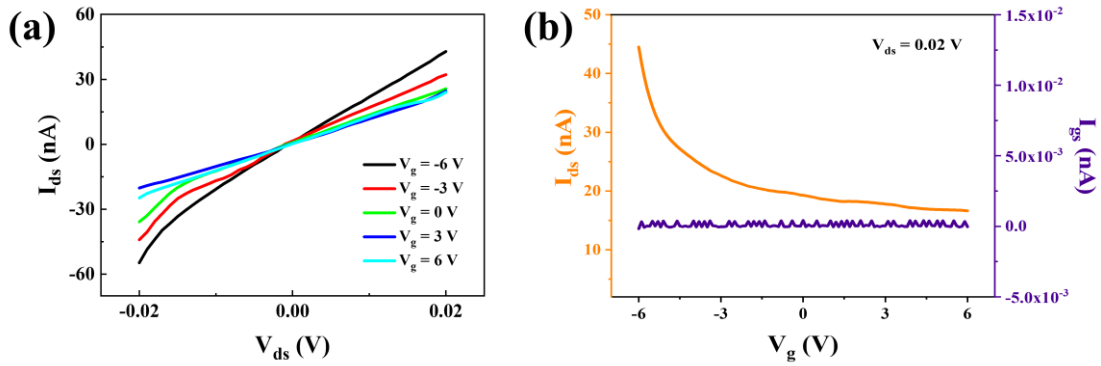

Figure 4.13 Electrical properties of top-gate field-effect-gating device based on SnSe nanosheets. (a) The output curves (I_{ds}–V_{ds}) of the SnSe FET device measured at

different gate voltages with a step of 3 V. (b) Transfer characteristic curve of the device at V_{ds} = 0.02 V, while the I_{gs} was also recorded.

4.6 SnSe-PENG performance

Owing to the intriguing flexibility, electrical and piezoelectric properties, SnSe nanosheets have the potential to be utilized in developing flexible nanogenerators for energy harvesting and motion monitoring. To further evaluate the output performance, the SnSe-PENG was developed with the same structure as that mentioned in Section 4.3. A linear mechanical system (Figure 2.15) was used to apply periodic strains to SnSe-PENG for measuring the piezoelectric output signals. The SnSe-based PENG in this work is designed for low-frequency operation (<10 Hz), targeting applications such as biomechanical energy harvesting. Thus, we employed impulsive mechanical excitation rather than harmonic vibration in our characterization. Nevertheless, during PFM measurements, cantilever tuning (resonating at ~180 kHz) was performed to identify the resonance behavior of the SnSe flake, indicating the intrinsic mechanical resonance of the SnSe nanosheet at the nanoscale. This suggests that the piezoelectric response of SnSe can be further amplified under resonance conditions, although this resonance is far beyond our operational frequency range. These observations provide valuable insight into the dynamic response of the material and suggest the possibility of resonance-enhanced performance in future device designs aimed at high-frequency applications.

Figure 4.14a-b illustrate the piezoelectric output signals generated by the flexible

nanogenerators. Positive output signals were collected under tensile strain, while the release of strain resulted in corresponding negative output voltage and current. At a strain of 1.03%, the open-circuit voltage and short-circuit current of the flexible nanogenerators were around 270 mV and 297 pA, respectively. It is worth noting that the observed open-circuit voltage (~270 mV) corresponds to a SnSe flake thickness of approximately 60 nm. While this might suggest a seemingly high piezoelectric potential at such a small thickness, the output voltage of a PENG does not scale linearly with material thickness. This is due to several contributing factors, including the device capacitance, internal impedance, charge screening, and non-uniform stress distribution across the film. Moreover, the Schottky interface between the SnSe and Au electrode also influences the effective carrier separation and voltage output. In thicker samples, the mechanical strain may not be efficiently transferred throughout the entire bulk material, leading to a lower strain-induced potential per unit thickness. Therefore, extrapolating the voltage to much thicker SnSe layers would not yield proportionally higher voltages, and the current output level is consistent with known behavior of nanoscale piezoelectric devices.

To evaluate the durability of the SnSe-based PENG under repeated mechanical deformation, we conducted a fatigue test by applying impulsive excitation using a linear motor for 1,600 consecutive cycles at 1.03% strain. As shown in Figure 4.14c, the output voltage remained consistent throughout the test with negligible degradation, indicating excellent mechanical and electrical stability. This suggests that the SnSe

nanosheet can sustain repeated elastic deformation without significant fatigue-induced performance loss. The result is consistent with the known mechanical resilience of two-dimensional layered materials, which can tolerate moderate strain due to their high flexibility and atomically thin nature.[53, 124] Although direct stress–strain hysteresis measurements were not performed, the consistent and reversible voltage output strongly implies minimal energy dissipation and limited mechanical hysteresis under the working conditions. These findings demonstrate the promising fatigue resistance of the device, which is essential for long-term applications in mechanical energy harvesting.

Besides, various external load resistances were incorporated into the circuit to evaluate the output power. As shown in Figure 4.14d, the voltage was initially small at small load resistances, and it started to rise as the load resistance was higher than 12 kΩ. On the contrary, the output current gradually decreased as the load resistance increased (Figure 4.14e). Consequently, the maximum output power was achieved with a load resistance of 10 MΩ under a strain of 1.03%, reaching approximately 21 pW (Figure 4.14f). The energy conversion efficiency (η)of SnSe-PENG could be calculated by the ratio of output electrical energy (W_E) and the applied mechanical energy (W_M). It is given as

$$\eta = W_E/W_M \tag{4-1}$$

Assuming the output power increases linearly with the applied strain to reach the maximum value, the output electrical energy could be expressed as[57]

$$W_E = (P_m \times s)/2 \quad (4\text{-}2)$$

where P_m is the maximum power, s is the working time (here s is 0.05 s). The applied mechanical energy could be presented as[136]

$$W_M = 1/2 \times EA(L - L_0)^2/L_0 = EAL_0\varepsilon^2/2 \quad (4\text{-}3)$$

where E is the elastic modulus of SnSe (E is 20-40 GPa for 2D SnSe[137]), A is the cross-sectional area of SnSe, L_0 and L represent the length before and after straining, respectively. The maximum power reached ~21 pW at 10 ΩM with the applied strain of 1.03%. As a result, the output electrical energy and the applied mechanical energy are found to be ~0.525 and ~5.642 pJ, respectively. Then the energy convesion efficiency is about 9.3%.

Moreover, a switched polarity test confirmed that the output signals originated from SnSe nanosheet rather than noise from background environment, as shown in Figure 4.15a-b. As the applied strains increase from 0.66% to 1.03%, the output signals exhibit a rising trend, indicating the good mechanical properties of the SnSe-PENG device (Figure 4.15c-d).

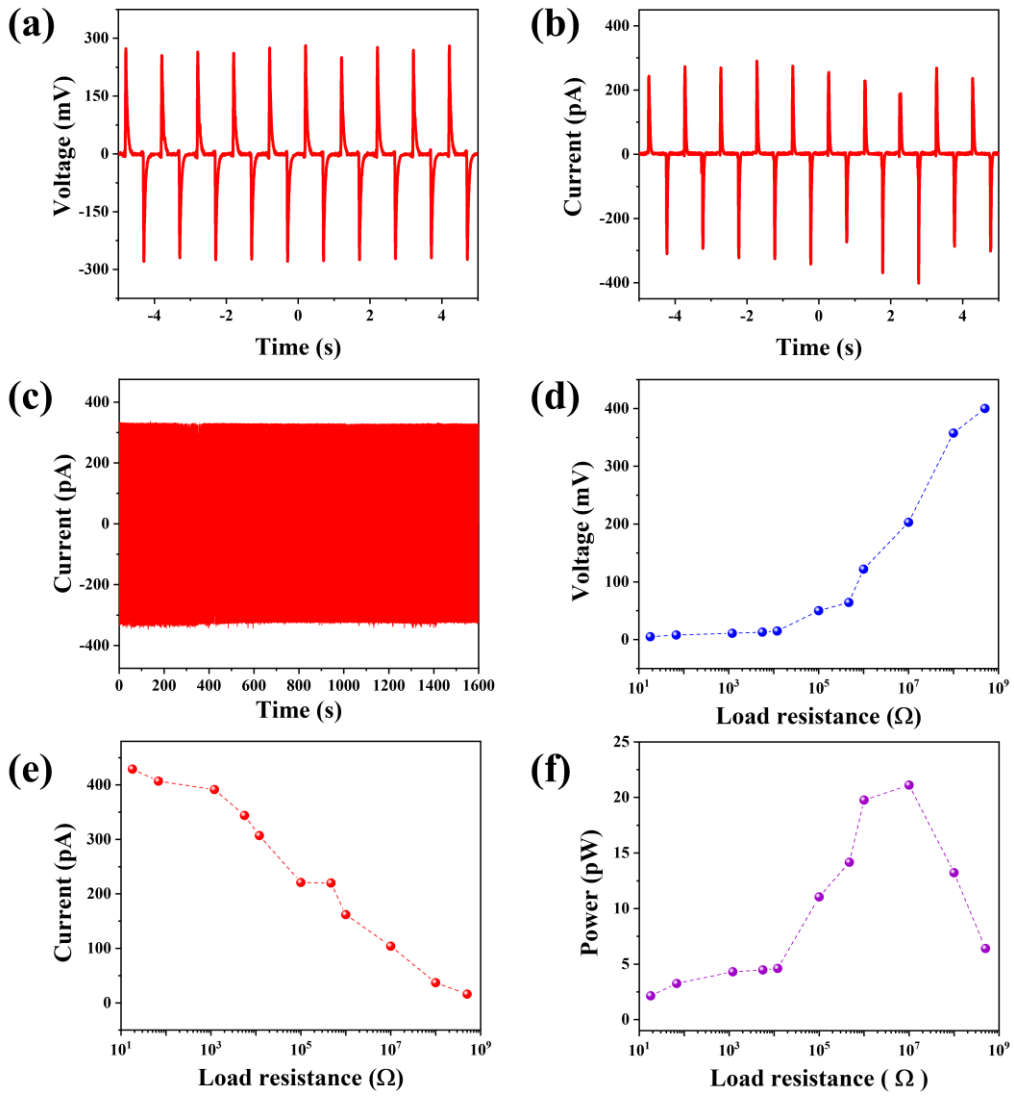

Figure 4.14 Output performance of SnSe-PENG at 1.03% strain. (a) Open-circuit output voltage. (b) Short-circuit output current. (c) Cyclic durability test, showing good stability. (d-f) Dependence of the peak output voltage, current, and the corresponding power as a function of external load resistance, respectively.

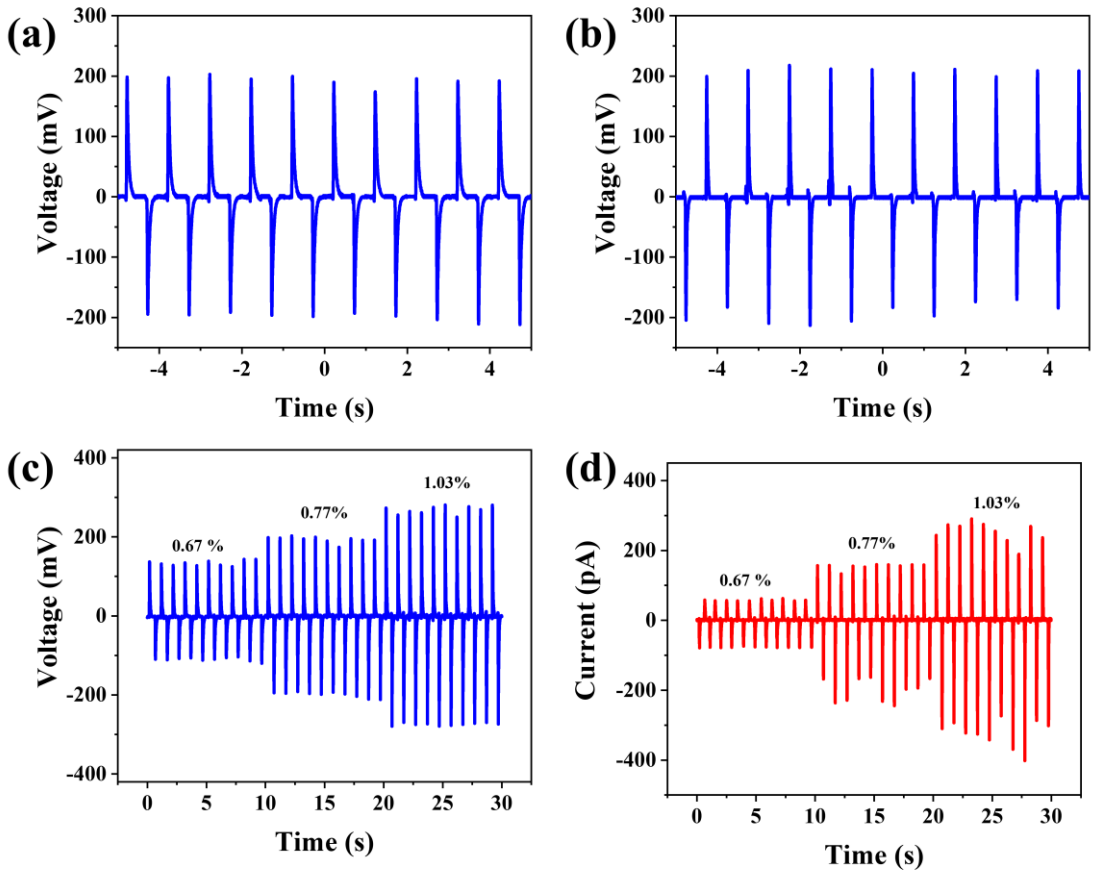

Figure 4.15 (a-b) Switched polarity of SnSe-PENG at 0.77% with forward and reverse connection, respectively. (c-d) Output voltage current signals at increasing strains ranging from 0.67% to 1.03%, respectively.

Furthermore, due to the flexibility of SnSe-PENG, this wearable nanogenerator device was attached to the finger and wrist of the tester, for sensing motion monitoring, as shown in Figure 4.16. We successfully recorded distinct piezoelectric output signals without the need for an external power during the bending and releasing movements, respectively. These signals indicate that the device could work in a self-powered mode. When the finger was bent, the voltage and current signals measured approximately 0.5 mV and 2.5 pA, respectively (Figure 4.16b-c). Similarly, the obtained output voltage

and current during wrist bending reached approximately 1 mV and 4 pA, respectively (Figure 4.16d-e). These piezoelectric output signals indicate that the SnSe sensor effectively converted mechanical energy from mechanically bending motions into electrical signals without the requirement of an external power supply. This underscores its remarkable self-powered sensing capability for monitoring human motion.

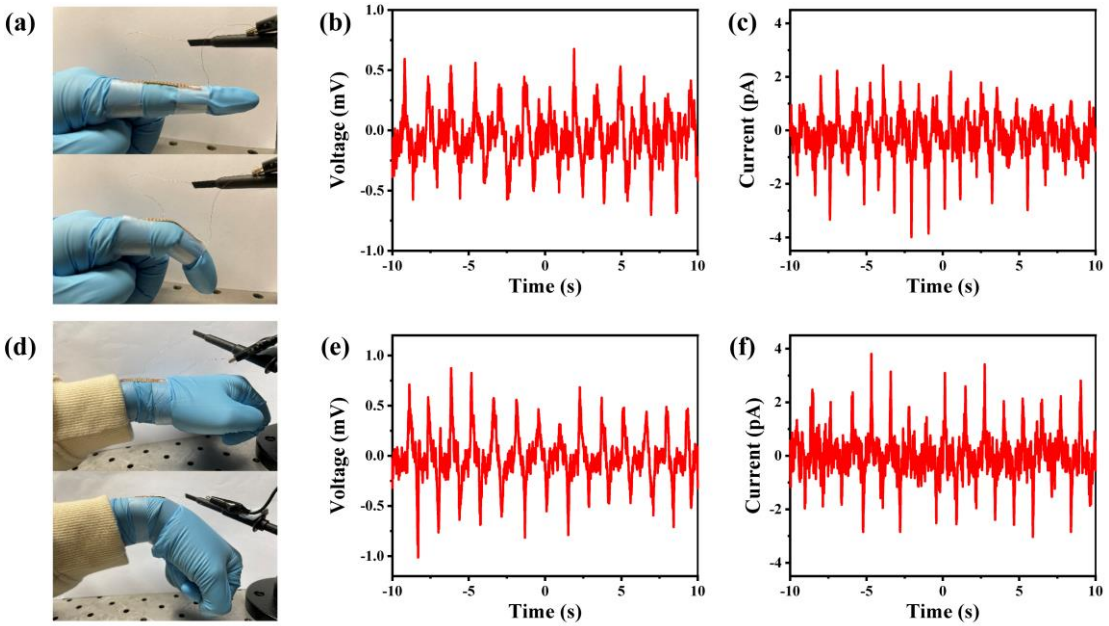

Figure 4.16 Output performance of self-powered piezoelectric sensor. (a) Finger motion monitoring during release (top) and bending (bottom). (b-c) Output voltage and current signals corresponding to finger motion. (d) Wrist motion monitoring during release (top) and bending (bottom). (e-f) Output voltage and current signals corresponding to wrist motion.

In order to make a comparison to other PENGs based on different layered materials, the performance in several aspects was summarized in Table 4.1. By comparing the parameters of PENGs based on different layered materials, we can clearly see that

SnSe-PENG shows significant excellence. Among these materials, SnSe nanosheets could sustain at a high strain of 1.03%, indicating that under the same conditions, it can withstand mechanical deformation better than other materials without losing functionality. In addition, the high output voltage and current signals reveals its excellent output capability and efficient charge transport performance. It is particularly worth mentioning that the maximum power density of SnSe nanosheets reaches up to 538 mW m^{-2}, which is the highest value among all materials in the table, which highlights its huge potential as a piezoelectric nanogenerator material. Furthermore, the conversion efficiency of SnSe nanosheets reached 9.3%, highlighting significant potential for future practical applications. These findings imply that the SnSe-PENG could function effectively as a motion sensor in self-powered wearable devices tailored for health tracking applications. By harnessing the piezoelectric output generated during motion, the SnSe-PENG can provide a reliable and self-sustainable energy source for healthcare in monitoring and tracking human movements.

Table 4.1 Comparison of piezoelectric output performance of PENGs based on layered materials. V_{oc} denotes the peak open-circuit voltage. I_{sc} is the peak short-circuit current; P_{max} represents the maximum power. PD is the power density. And η stands for conversion efficiency. †Some values were obtained from the graph from the references.

Layered material	**Strain**	**V_{oc}**	**I_{sc}**	**P_{max}**	**PD**	**η**
Monolayer MoS_2[53]	0.53%	15 mV	20 pA	5.53 × 10^{-2} pW	2 mW m^{-2}	~5.08%

Layered material	**Strain**	**V_{oc}**	**I_{sc}**	**P_{max}**	**PD**	**η**
				at~220 MΩ		
Monolayer MoS_2[69]	0.48%	20 mV (armchair) < 10 mV (zigzag)	> 30 pA (armchair) < 20 pA (zigzag)	2.89×10^{-1} pW at~220 MΩ†	N/A	N/A
Pristine monolayer MoS_2[54]	0.48%	22 mV	100 pA	0.07 pW at 500 MΩ	7.3 μW m^{-2}	N/A
Passivated monolayer MoS_2[54]	0.48%	10 mV	~30 pA	0.73 pW at 500 MΩ	73 μW m^{-2}	N/A
Monolayer WSe_2	0.39%	45 mV	100 pA	2.54 pW at 500 MΩ	N/A	2.41%
turbostratic stacking Bilayer WSe_2[57]	0.89%	~70 mV†		4.05 pW at 500 MΩ	N/A	1.69 %
Monolayer WS_2[70]	1.56%	65 mV	325 pA	N/A	6 mW m^{-2} at 500 MΩ	N/A
SnS[68]	0.70%	~150 mV	160 pA	24 pW at 1 GΩ	24 mW m^{-2}	N/A

Layered material	**Strain**	**V_{oc}**	**I_{sc}**	**P_{max}**	**PD**	**η**
Multilayer BP[131]	0.56%	~7.5 mV	~2.7 pA	N/A	N/A	N/A
7L In_2Se_3[72]	1%	363 mV	598.1 ± 19.4 pA	N/A	N/A	N/A
In_2Se_3[66]	0.76%	35.7 mV	47.3 pA	N/A	N/A	N/A
PbI_2[138]	0.339%	29.4 mV	20 pA	0.12 pW at 1 GΩ		~3.2%
$Sn_{(1-x)}Se_x$ nanowall/μ-spheres (~ 35 nm)[125]	Finger bending	~1.5 V	~ 10 nA	20 nW at ~1.9 MΩ	N/A	N/A
Mechanical-exfoliated SnSe[124]	0.1%	~14 mV†	~400 pA†	5.6 pW at ~5 MΩ	28 mW m^{-2}	6.5%
48 nm 3R-MoS_2[58]	0.47%	~70 mV	~180 pA	11.8 pW at 200 MΩ	65 mW m^{-2}	N/A
SnSe nanosheets (this work)	1.03%	~270 mV	~297 pA	~21 pW at 10 MΩ	~538 mW m^{-2}	~9.3%

While scaling laws often provide useful insights into the performance trends of nanogenerators, it is important to recognize that physical behavior does not always scale linearly, especially when transitioning from the nanoscale to the microscale or macroscale. In our study, the SnSe flake thickness is within the tens-of-nanometers range, where surface effects, strain confinement, and interfacial charge interactions play a significant role. As device dimensions increase toward the micrometer scale, the influence of surface-to-volume ratio decreases, and certain macroscopic material properties (such as mechanical stiffness, fracture thresholds, and charge screening) begin to dominate. Therefore, while theoretical extrapolations are useful for understanding trends, the actual device performance at larger thicknesses or lateral dimensions may deviate significantly from nanoscale behavior. For 2D layered materials like SnSe, this transition is particularly complex due to the anisotropic bonding and the van der Waals interlayer coupling, which make their behavior at micro- and macro-scales fundamentally different from conventional 3D bulk materials. Further investigation into this scaling transition remains a promising direction for both theoretical and experimental research.

4.7 Summary

In summary, the SnSe layered nanosheets, grown through vapor transport deposition, exhibit robust piezoelectric properties and have been utilized to create flexible nanogenerators for energy harvesting and human motion monitoring. These large-scale, high-quality SnSe nanosheets demonstrate strong layer-dependent in-plane

piezoelectric characteristics. The electrical properties of SnSe nanosheets were explored through the fabrication of field-effect-gating devices, revealing distinct p-type transfer behavior with a significant mobility of 19.35 $cm^2 V^{-1} s^{-1}$. The enhanced piezoelectric performance of SnSe was evidenced by achieving a remarkable energy conversion efficiency of 9.3% and a peak power density of 538 $mW cm^{-2}$ at 1.03% strain. Moreover, a self-powered sensor for monitoring human motion was developed using the SnSe PENG, showcasing its potential applications in intelligent piezoelectric sensors and advanced microelectromechanical devices.

Chapter 5 High-entropy MXene for flexible nanogenerators

5.1 Introduction

MXene, as an emerging layered transition metal carbide/nitride, has garnered extensive attention from researchers worldwide due to its excellent conductivity, good hydrophilicity, large layered structure, tunable composition and so on, showing tremendous potential applications in fields such as electronics, energy storage, electromagnetic shielding and sensors.[139-142] So far, the primary method for synthesizing MXene is fluorine acid etching, with etchants such as HF,[143] LiF+HCl,[142] and $(NH_4)HF_2$.[144] This method selectively etches the 'A' layer of the MAX phase using fluoride-containing ion solutions to achieve etching, offering advantages such as easy operation, relatively mild etching conditions, large interlayer spacing and less defects. After etching, different functional groups (T_x, such as -O, -OH, -Cl, -F) are terminated to the surface, imparting MXene with advantages such as good hydrophilicity, electrical conductivity, and outstanding biocompatibility. However, these etchants not only exhibit high corrosiveness but also pose environmental pollution and safety hazards.[145] Additionally, terminal groups with fluoride ions would inhibit the reactivity of MXene. For instance, in electrochemical energy storage, the presence of fluoride ions can increase the diffusion barrier of lithium ions, inhibiting the reaction stability of the electrolyte and the MXene electrode interface.[146] Therefore, the preparation of HF-free MXene is particularly desirable and crucial to address these challenges. In recent years,

various methods have been reported for the fluoride-free etching preparation of MXene, including the alkaline hydrothermal treatment,[83] molten salt techniques,[147] sequential bridging with liquid metal [148]and fluoride-free electrochemical etching.[87] Given that these approaches are free of hazardous fluoride-based substances or severe etching environments, they present the attractive options for the efficient fabrication of innovative MXene materials.

Due to the symmetry breaking primarily originating from the multi-atomic structure and uneven distribution of functional groups, MXene exhibits intrinsic piezoelectricity and shows great potential for wearable electronics and sensors.[149, 150] Furthermore, high-entropy MXene with usually five or more elements have emerged as promising materials by virtue of the improved hardness, oxidation resistance and low thermal conductivity, allowing for application in some harsh environments.[151-153] Their unique structure endows with higher symmetry breaking in high and near equiatomic concentrations. As shown in Figure 5.1, the single-layer of high-entropy MXene $TiVCrMoC_3T_x$ nanosheet is combined with four metal layers with carbon interlayers in between.[153] The outermost metal atoms form active bonds with surface functional groups, whose asymmetric distribution breaks the inversion symmetry of the crystal lattice. [149, 153]. This structure complexity provides more possibilities for design tunable material properties for diverse applications.[154, 155] Therefore, the outstanding bio-compatibility, mechanical properties and high stability of high-entropy MXene make it promising for scalable applications in sensors, wearable electronics and beyond. Here,

high-entropy MXene $TiVCrMoC_3T_x$ nanosheets were synthesized by fluoride-free electrochemical etching technique and further developed into flexible nanogenerators based on MXene-PVA composite film.

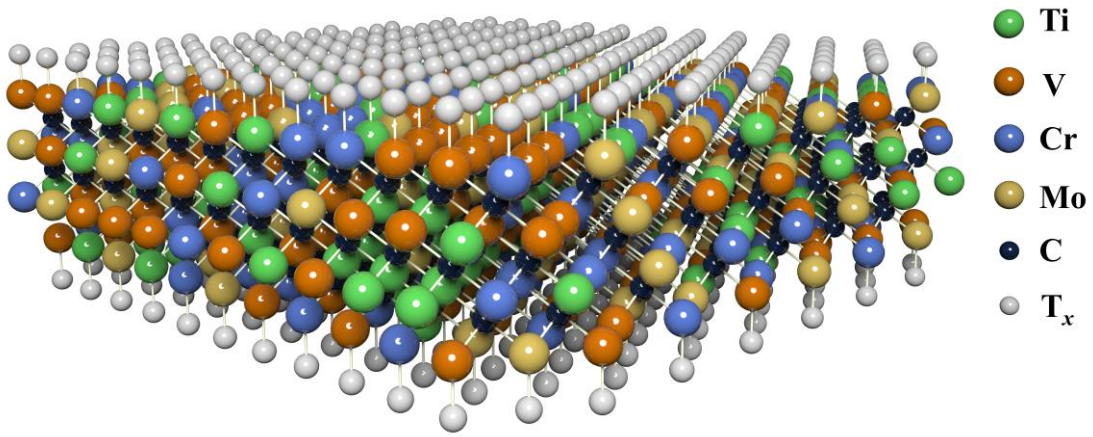

Figure 5.1 Structure of high-entropy MXene $TiVCrMoC_3T_x$.

5.2 Synthesis of high-entropy MXene nanosheets

The high-entropy MXene nanosheets ($TiVCrMoC_3T_x$) were synthesized by a thermal-assisted electrochemical HF-free etching procedure as the previously reported.[87, 156] The preparation of the high-entropy MXene involved a five-step synthesis process: initial substrate purification, electrochemical etching, sonication for delamination, separation of precursor and MXene, MXene purification. The details of each step will be introduced as below.

Step i: initial substrate purification. The carbon fiber cloths (W0S1002, CeTech) used as carbon source and conductive substrate was first cleaned in acetone and ethanol under sonication to remove the organic contaminant on the surface. Followed by surface modification with HNO_3 (63 wt. %, Sigma) for 6 hours under reflux at 125 °C, they

were neutralized with 1M NaOH solution. After that, the carbon fiber cloths were rinsed three times with deionized water and dried in the oven at 60 °C.

Step ii: electrochemical etching. The electrochemical etching worked in a standard three electrode configuration. The MAX precursor ($TiVCrMoAlC_3$, >99%, Laizhou Kai Ceramic Material Co., Ltd) was first mixed with carbon black in a 95:5 ratios, and then dispersed in 1% PVA as the adhesion agent, forming a composite electrode. Then the mixture was uniformly distributed on the carbon fiber cloths. The etching voltage was set to be 1 V, and the temperature was set at 55 °C to improve etching efficiency and yield. The 'A' layer in MAX precursor material was etched in the dilute HCl electrolyte. The etching process could be described as follows:

$$TiVCrMoAlC_3 + yCl^- + (2x+z)H_2O \rightarrow TiVCrMoC_3(OH)_{2x}Cl_yO_z + Al^{3+} + (x + z)H_2 + (y + 3)e^- \quad (5\text{-}1)$$

Step iii: sonication for delamination. The sample were first intercalated within tetrabutylammonium hydroxide (TBAOH) solvents. The mixture was stirred at room temperature for 24 hours and then subjected to bath sonication for 3 hours at 60 W and 40 Hz.

Step iv: separation of precursor and MXene. After the sonication, the MXene nanosheets were separated by the centrifuge at 3500 rpm for 15 min. The supernatant was collected after rest for 5 min.

Step v: MXene purification. The preliminary MXene nanosheets were further centrifuged at 9500 rpm for 10 min. Then the obtained MXene nanosheets were further

purified with sonication in ethanol for four times to remove any residual etchants or by-products.

Furthermore, a comparative summary of key parameters associated with various HF-free MXene synthesis methods is provided in Table 5.1. Operating under mild conditions (25–80 °C) with diluted HCl in ambient atmosphere, the proposed synthesis approach offers notable advantages in terms of safety and operational simplicity when compared to high-temperature techniques that require inert environments. With a reasonable yield and minimal equipment demands, this method provides a favorable balance between accessibility, safety, and environmental sustainability, while also broadening the range of accessible MXene compositions.

Table 5.1 The comparison of common MXene synthesis methods.

Method	**Temperature**	**Etching Agent**	**Processing Time**	**Yield**	**Safety concern**	**Scalability**
HF Etching [157, 158]	RT	HF	24-72 h in air	~40-98%	Hazardous HF handling required	Limited by safety concerns
LAMS (Lewis Acid Molten Salt) [159-161]	>550 °C	Lewis acidic salts ($ZnCl_2$,	4-24 h in inert gas (heating	~50-75%	High temperature, inert gas	Good - Scalable process

Method	**Temperature**	**Etching Agent**	**Processing Time**	**Yield**	**Safety concern**	**Scalability**
		$CuCl_2$, $FeCl_2$, etc.)	and cooling time excluded)		required	with few safety limitations
MS^3 (salt shielded) [162]	~700 °C	Molten salts	10-40 mins in air (heating and cooling time excluded)	Not reported	High temperature process	Moderate
Thermal-assisted electrochemical etching (this work and ref. [87])	25-80 °C (optimally at 50 °C)	Diluted HCl	3-9 h in air	~50% (up to ~75% with recycling)	Diluted HCl	Good - Simple setup, recyclable

Method	**Temperature**	**Etching Agent**	**Processing Time**	**Yield**	**Safety concern**	**Scalability**
MS-E-etching (Molten-salt-assisted electrochemical etching) [163]	450°C	LiCl-KCl melts	12 h in inert gas	~95%	High temperature, inert gas required	Good - One-pot process, reusable salts

5.3 Characterization of $TiVCrMoAlC_3$, $TiVCrMoC_3T_x$ and MXene-PVA composite film

The as-prepared high-entropy $TiVCrMoC_3T_x$ MXene nanosheets were first characterized to reveal their structural and morphological properties, as shown in Figure 5.2. The XRD patterns depicted in Figure 5.2a illustrate that the peaks of $TiVCrMoC_3T_x$ align well with previously reported findings.[153] The (00*l*) peaks of $TiVCrMoC_3T_x$ exhibit a leftward shift, with no apparent appearance of Al-Mo peaks in $TiVCrMoC_3T_x$, signifying successful delamination from the MAX phase. In the Raman spectra captured in Figure 5.2b, the augmentation and red shift of characteristic peaks (around 200 and 700 cm-1) in the resulting $TiVCrMoC_3T_x$ nanosheets validate the elimination of Al layers from their parent MAX phase.[139, 164-168] Furthermore, the broad peaks within the 1200-1700 cm^{-1} range correspond to the D and G bands of carbon.[169, 170] These findings provide confirmation of the efficient removal of Al layers from the

MAX phase and the successful formation of MXene nanosheets. Moreover, detailed insights into the morphology of MXene nanosheets were provided through SEM images in Figure 5.2d, showcasing uniform and layered nanosheets with an accordion-like texture post-etching from the bulk MAX precursor with smooth surfaces (Figure 5.2c). Notably, the synthetic strategy employed in this work deliberately yields multilayered MXene structures, rather than pursuing monolayer exfoliation, as the multilayered form is more suitable for integration with polymer matrices in the intended application. TEM (Figure 5.2g) and AFM characterizations (Figure 5.2h) confirm the successful fabrication of multilayered MXene with thicknesses appropriate for the electromechanical functionalities targeted in this study.

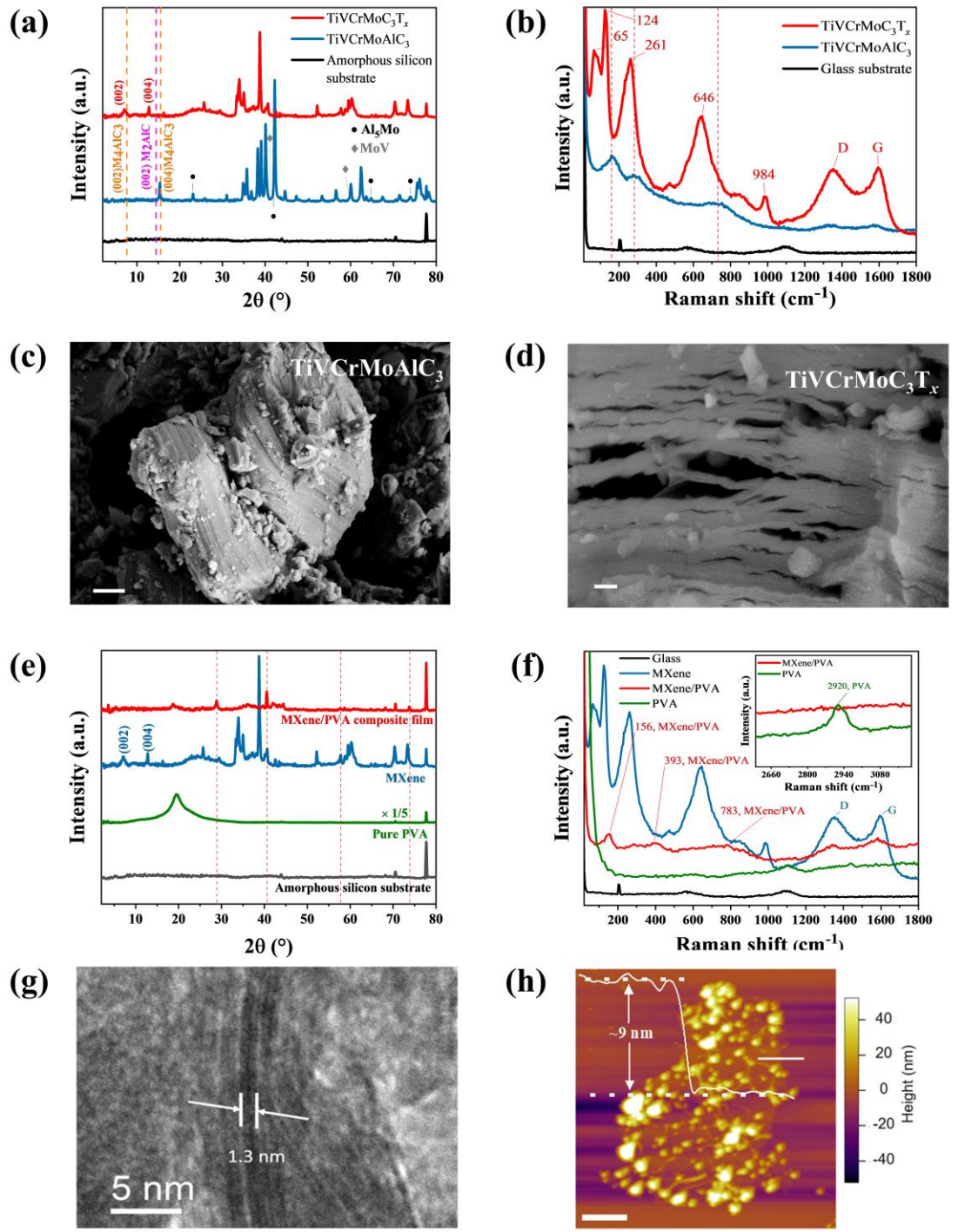

Figure 5.2 Characterization of $TiVCrMoAlC_3$ MAX precursor, the resulting $TiVCrMoC_3T_x$ layered MXene nanosheets and MXene-PVA composite film. (a&e) XRD patterns. (b&f) Raman spectra. (c-d) SEM images of $TiVCrMoAlC_3$ (scale bar: 2 μm) and layered $TiVCrMoC_3T_x$ MXene nanosheets (scale bar: 200 nm). (g) The TEM image of high-entropy MXene nanosheet. The TEM image confirms the predominantly

multilayered nature of our MXene nanosheets, with 3 layers and a single layer thickness of ~1.3 nm. (h) The AFM image and height profile of high-entropy MXene nanosheet. Scale bar: 1 μm.

In order to achieve the scalable application of layered MXene nanosheets, the high-entropy MXene nanosheets were further developed into flexible films by constructing composite films within PVA matrix by a direct self-assembly path. The PVA with flexibility, natural compatibility and degradability, is often used as the matrix material in composite structures, providing a flexible and durable matrix for embedding functional materials.[171] It can also improve the mechanical properties of the composite, making it more robust to mechanical stress and deformation, which is important for maintaining the structural integrity of the nanogenerators during operation. The –OH on PVA chains could guide material self-assemble stacking with strong hydrogen bonding.[171, 172]

As shown in Figure 5.3, the PVA was employed as a cross-linker to form a network with high-entropy MXene, showing the intermolecular interaction in the strong hydrogen bonding. Therefore, the MXene-PVA composite film exhibits good stability with the protection of PVA coat, and high piezoelectric response due to the intrinsic symmetry breaking structure in high-entropy MXene layer and the structural complexity by cross-linking with PVA polymer network. In addition, the MXene-PVA composite film also demonstrates the enhanced biocompatibility and scalability, endowing the functionality for practical applications.

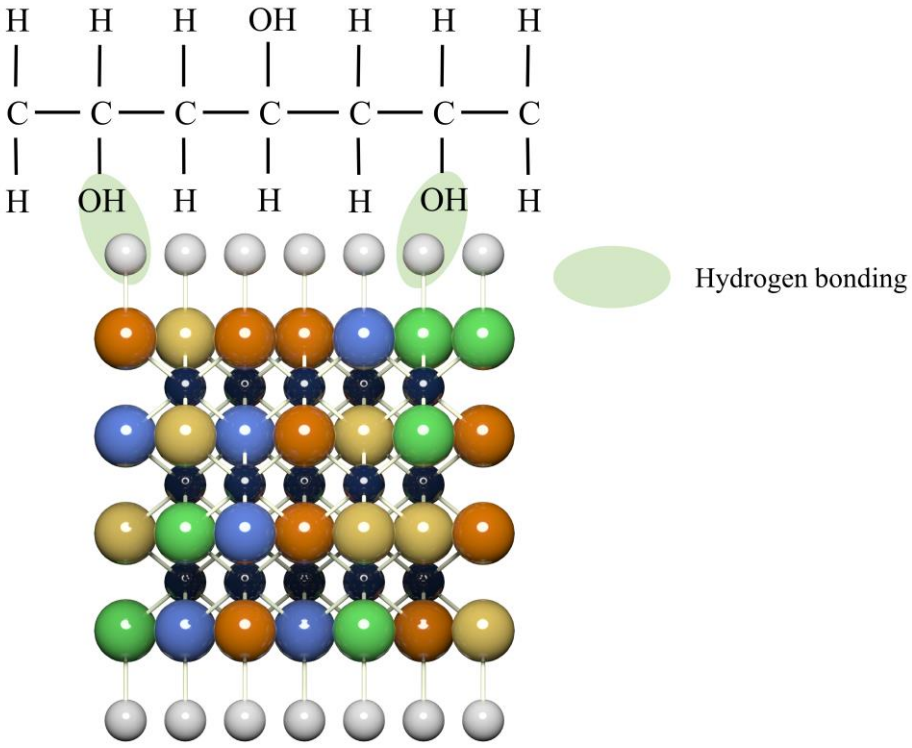

Figure 5.3 The schematic illustration of the MXene-PVA composite film with cross-linked structures.

The preparation of MXene/PVA film and its flexible nanogenerators are introduced as follows. Specifically, the as-prepared 5 mg/mL MXene solution was mixed with 10 % PVA aqueous solution with equal proportion and stirred completely by magnetic stirrer. The homogeneous dispersion was first degassed thoroughly and then poured into a mold and then dried overnight in drying cabinet to obtain a uniform and flexible MXene/PVA film (as shown in the inset of Figure 5.4), which was further developed into flexible nanogenerators device (MXene/PVA-PENG) by connecting to the conductive Ni tapes and attached onto PI substrate (as shown in the inset of Figure 5.4). A linear motor system (Figure 5.4) was employed to provide periodic strains to MXene/PVA nanogenerators for self-powered output measurements.

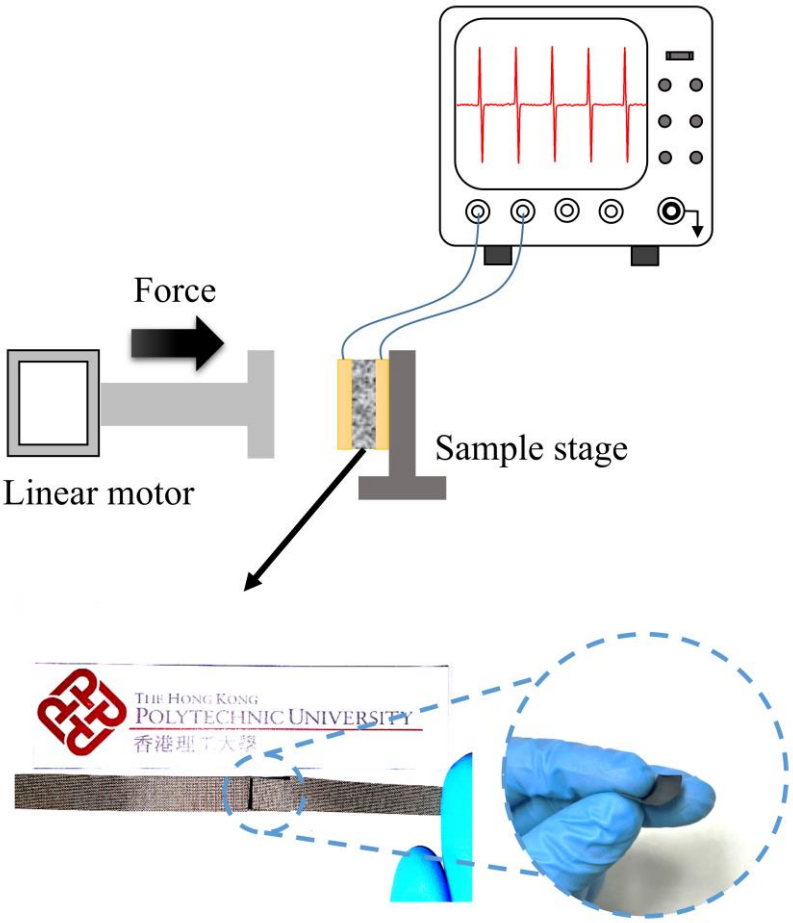

Figure 5.4 Experimental setup for output performance testing of MXene/PVA-PENG. Inset below left: The MXene/PVA-PENG device and the MXene-PVA composite film. Inset below right: Flexible MXene-PVA composite film.

Following the confirmation of the successful delamination of layered MXene nanosheets and the interaction between MXene and PVA, we delved deeper into characterizing the high-entropy MXene-PVA composite film. Comparative analysis with the XRD pattern of pristine high-entropy MXene revealed that the (002) peak of the MXene-PVA composite film shifted towards lower angles in Figure 5.2e, indicating an increase in *d*-spacing. This shift is attributed to the robust interaction between

MXene and PVA, facilitated by the formation of hydrogen bonding. In Figure 5.2f, three primary Raman peaks were identified, corresponding to Ti-C vibrations.[173, 174] Relative to the pristine materials, the Raman response of the MXene-PVA composite film decreased and exhibited a blue shift, a consequence of the distinct interaction of PVA chains. These characterizations underscore the high quality of the layered MXene nanosheets and the MXene-PVA composite film, holding significant promise for a diverse array of advanced technological applications.

The mechanical properties of the MXene–PVA composite film were evaluated using a dynamic mechanical analyzer (DMA1, Mettler Toledo) operating in tensile mode. From the stress–strain curve (Figure 5.5), the Young's modulus of the 40 μm-thick MXene–PVA film is determined to be 2 GPa, whereas that of the pure PVA film is 1 GPa. This enhancement in mechanical strength is attributed to strong hydrogen bonding between MXene sheets and PVA chains, indicating the suitability of the MXene–PVA composite film for practical applications.

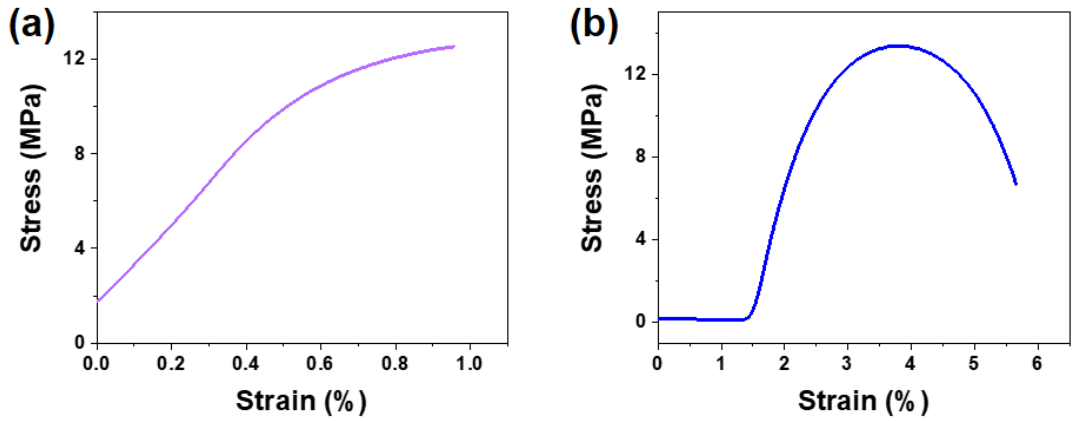

Figure 5.5 The stress-strain curve of MXene-PVA composite film (a) and pure PVA film (b). The MXene–PVA composite film has a rectangular geometry with dimensions of

19.28 mm in length, 10 mm in width, and 0.04 mm in thickness. In comparison, the pure PVA film measures 18 mm in length, 9 mm in width, and 0.02 mm in thickness.

The electrical properties of the films were further assessed via P–E hysteresis measurements (Figure 5.6) and dielectric analysis (Figure 5.7). The transition from lossy capacitor behavior in pure PVA to resistor-like characteristics in the MXene–PVA composite suggests enhanced conductivity and pronounced interfacial polarization, which contribute to improved piezoelectric charge generation. The incorporation of MXene slightly increases the dielectric constant, indicating enhanced polarizability favorable for piezoelectric performance. With increasing frequency, the dielectric loss initially decreases due to reduced interfacial leakage currents, attributed to suppressed interfacial polarization, and subsequently increases as a result of dipolar hysteresis within the polymer matrix.[173, 175]. Furthermore, the leakage current remains at the picoampere level, effectively minimizing charge dissipation and ensuring reliable signal output.

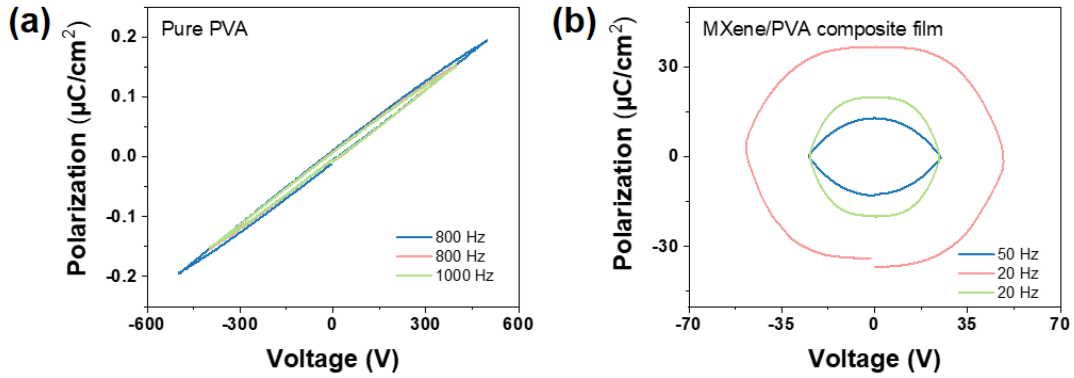

Figure 5.6 P-E loops of pure PVA (a) and MXene-PVA composite film (b).

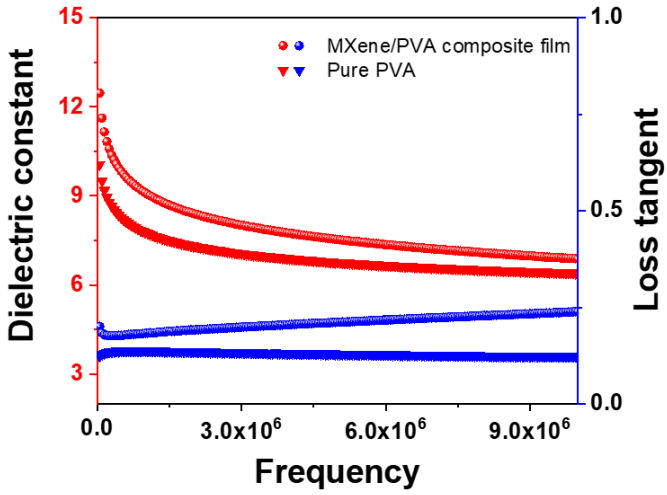

Figure 5.7 Dielectric constant and loss tangent of pure PVA and MXene-PVA composite film.

5.4 Flexible nanogenerators based on high-entropy MXene nanosheets

Based on the promising piezoelectric and mechanical properties, the MXene-PVA composite film was further developed into flexible nanogenerators by connecting Ni electrodes for self-powered electrical measurements. To analyze the piezoelectric behavior of high-entropy $TiVCrMoC_3T_x$ MXene, the polarization charge generation process under the external stress is schematically illustrated in Figure 5.8. The $TiVCrMoC_3T_x$ monolayer features a hexagonal lattice composed of four transition metals (Ti, V, Cr, Mo) and carbon atoms, terminated by surface functional groups.[153] The multi-element configuration and asymmetric surface terminations break inversion symmetry in the crystal structure, as previously reported.[176-178] In the equilibrium state, the dipole moments (P_1, P_2, P_3) within the metal–T_x units cancel out ($P_1 + P_2 + P_3 = 0$; Figure 5.8b, left inset). Upon application of strain, the redistribution of these dipole

moments—specifically, increased P_1 and decreased P_2 and P_3—shifts the charge centers, leading to net ionic polarization and the formation of a directional piezoelectric field (Figure 5.8, right inset). Additionally, stretching of the metal–C bonds perturb the dipole balance (P_4, P_5, P_6), generating secondary polarization; however, its contribution is minor compared to that of the metal–T_x bonds (Figure 5.8c). The primary piezoelectric response originates from non-centrosymmetric lattice distortions induced by both the terminal functional groups and the asymmetrically distributed metallic elements.[149, 155] Owing to its periodic metal–T_x and metal–C motifs and compositional asymmetry, $TiVCrMoC_3T_x$ exhibits robust piezoelectricity under mechanical deformation. The incorporation of multiple transition metals in $TiVCrMoC_3T_x$ MXene introduces substantial compositional disorder, leading to lattice distortions and symmetry breaking. This structural complexity, inherent to high-entropy systems, facilitates the stabilization of single-phase architectures, enhances local polar asymmetry, reduces elastic stiffness to strengthen electromechanical coupling, and fosters domain evolution favorable for polarization reorientation.[179] Similar phenomena have been observed in other high-entropy systems, such as high-entropy perovskites and $Mo_{1-x}W_xS_2$ alloys, where atomic-scale disorder has been shown to improve functional performance.[180, 181]

In addition, interfacial polarization at the heterogeneous boundaries between MXene nanosheets and the PVA matrix generates localized electric fields under mechanical stress. These fields promote dipole realignment within both the polymer

chains and the surface functional groups of MXene, thereby enhancing strain-induced polarization. This mechanically driven dipole alignment, facilitated by interfacial polarization, yields a more efficient and coordinated polarization response within the composite system.[172, 175] Although the MXene–PVA film does not exhibit ferroelectricity, its pronounced piezoelectric response is attributed to the combined effects of interfacial polarization at the MXene/PVA interface, high-entropy lattice distortion, surface functional groups on MXene, and strain-induced dipole alignment within the polymer matrix. These synergistic mechanisms collectively account for the observed piezoelectric behavior in the composite.[149, 182]

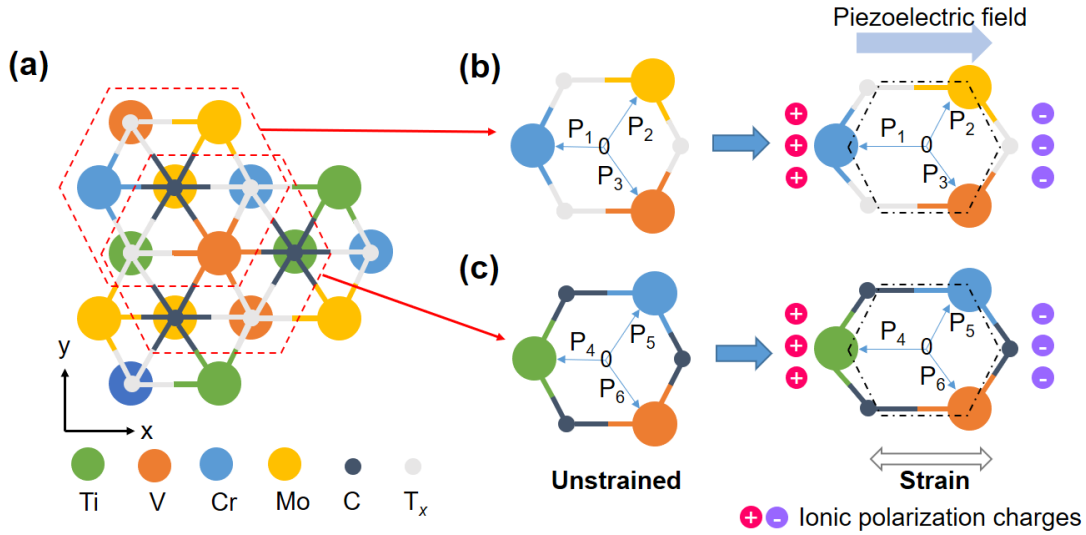

Figure 5.8 The generation of piezoelectric filed in $TiVCrMoC_3T_x$ by an external strain. (a) Top view of $TiVCrMoC_3T_x$ structure. (b) Simplified Metal-T_x hexagonal structure. (c) Metal-C hexagonal structure.

In the PENG output measurement, the applied uniaxial force on the MXene-PVA composite film was measured using an ergometer (in kgf, AIPU ZP-Series). The output

performance of MXene/PVA nanogenerator is demonstrated in Figure 5.9. At a compressive force of 3.47 N, the MXene/PVA-PENG exhibited output current and voltage signals of 790 pA and 500 mV, respectively (Figure 5.9a-b). Notably, a positive output piezoresponse was generated under the applied compressive strain, with the output voltage and current shifting towards negative values upon strain removal, as illustrated in the insets of Figure 5.9a-b. The output signals demonstrated an increase with the applied compressive force ranging from 1.96 to 3.47 N (Figure 5.9c-d), showing good mechanical properties. Furthermore, the peak output current remained stable over 1,500 cycles at 1.96 N (Figure 5.9e-f), which is comparable to those of the previously reported PENGs.[58, 66, 124, 176, 181, 183] These results affirm the remarkable mechanical durability and functionality of the MXene/PVA flexible nanogenerators, paving the way for their practical utilization in wearable electronics and self-powered sensors.

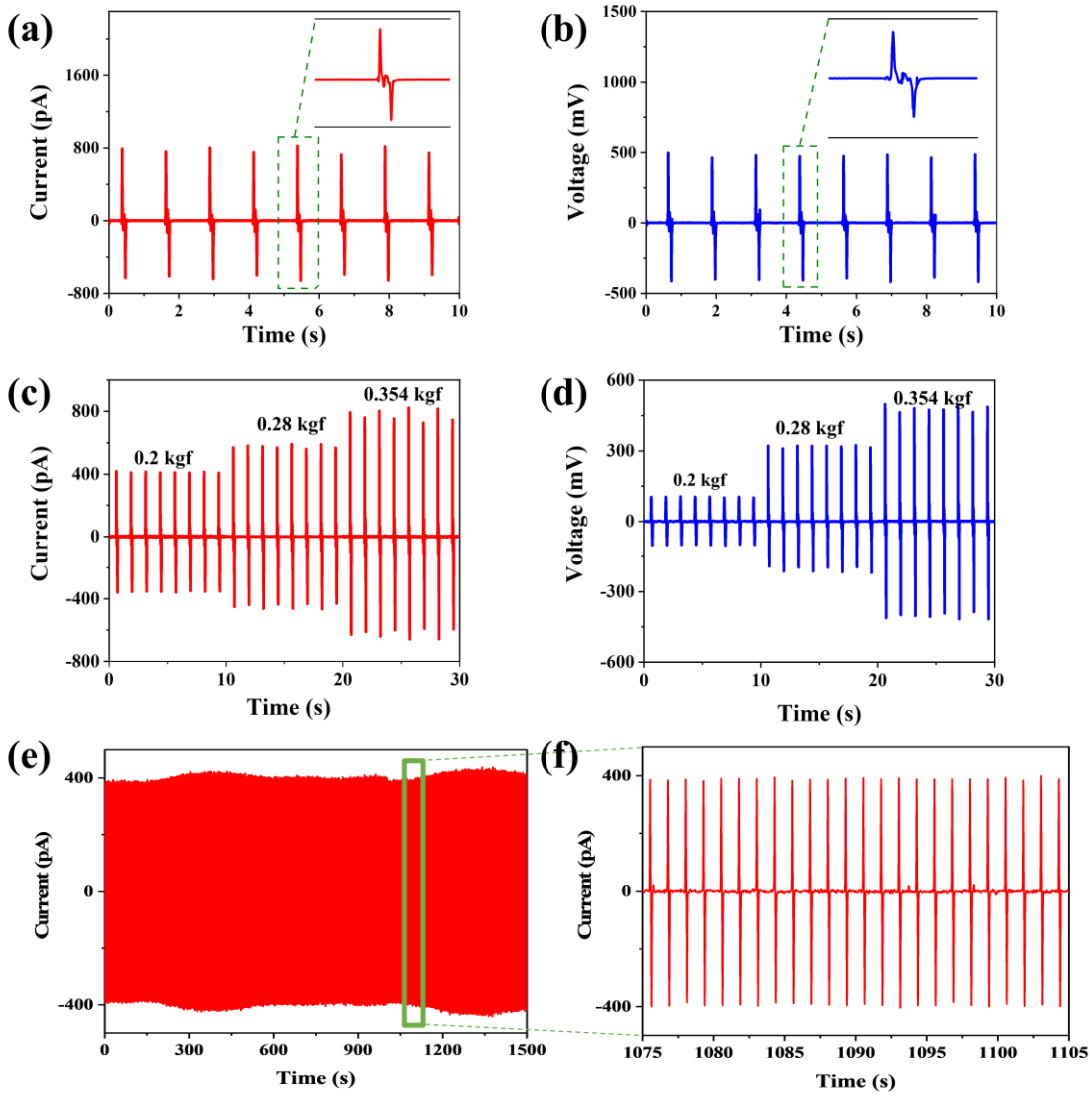

Figure 5.9 The output performance of MXene/PVA flexible nanogenerator. (a-b) The output current and voltage signals obtained at 3.47 N. (c-d) The output signals obtained at different applied forces. (e-f) Cyclic durability test for 1,500 cycles at 1.96 N and its corresponding enlarged image from the green box.

The switched polarity measurements on current and voltage signals were also performed, as shown in Figure 5.10, suggesting that the obtained signals originate from the MXene/PVA nanogenerator device. The voltage and current under different load resistances were also measured to observe how the PENG responds to varying loads,

as shown in Figure 5.11. The voltage increased with the increasing load resistors, while the current signals were opposite. The output power obtained from multiplying the voltage and current could reach up to 110.76 pW, allowing for practical applications for low-power systems.

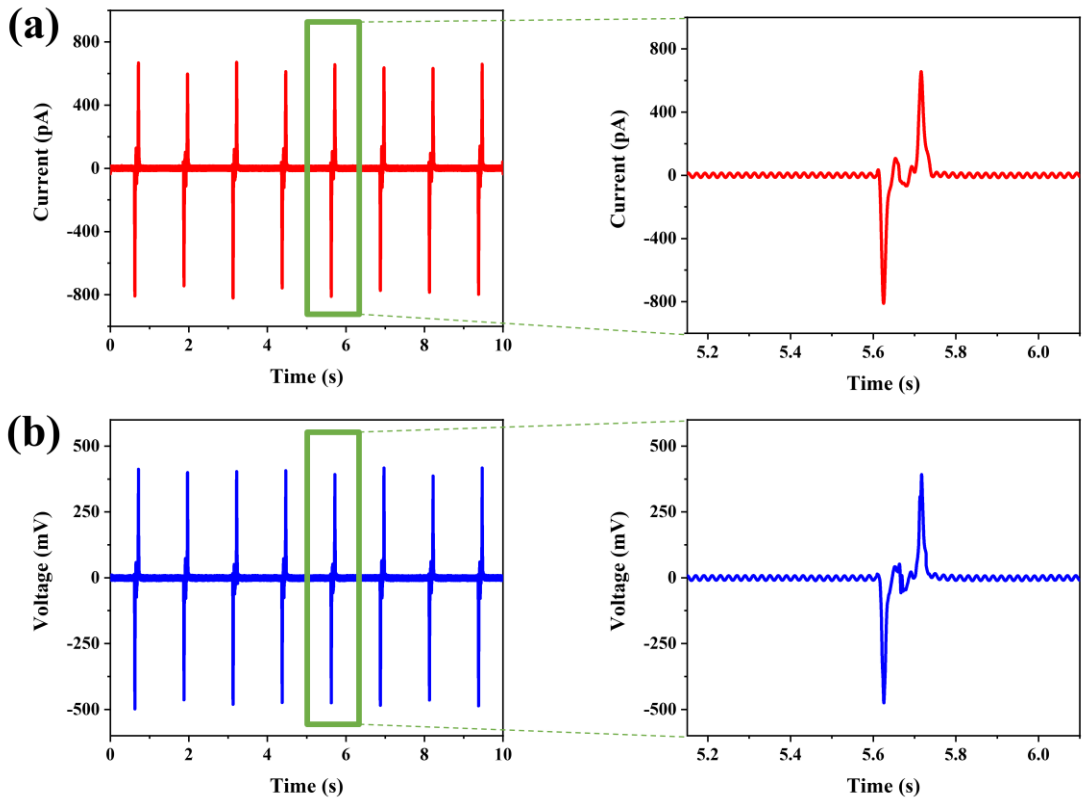

Figure 5.10 Switched polarity in current (a) and voltage (b) of MXene/PVA-PENG at 3.47 N with forward and reverse connection, respectively.

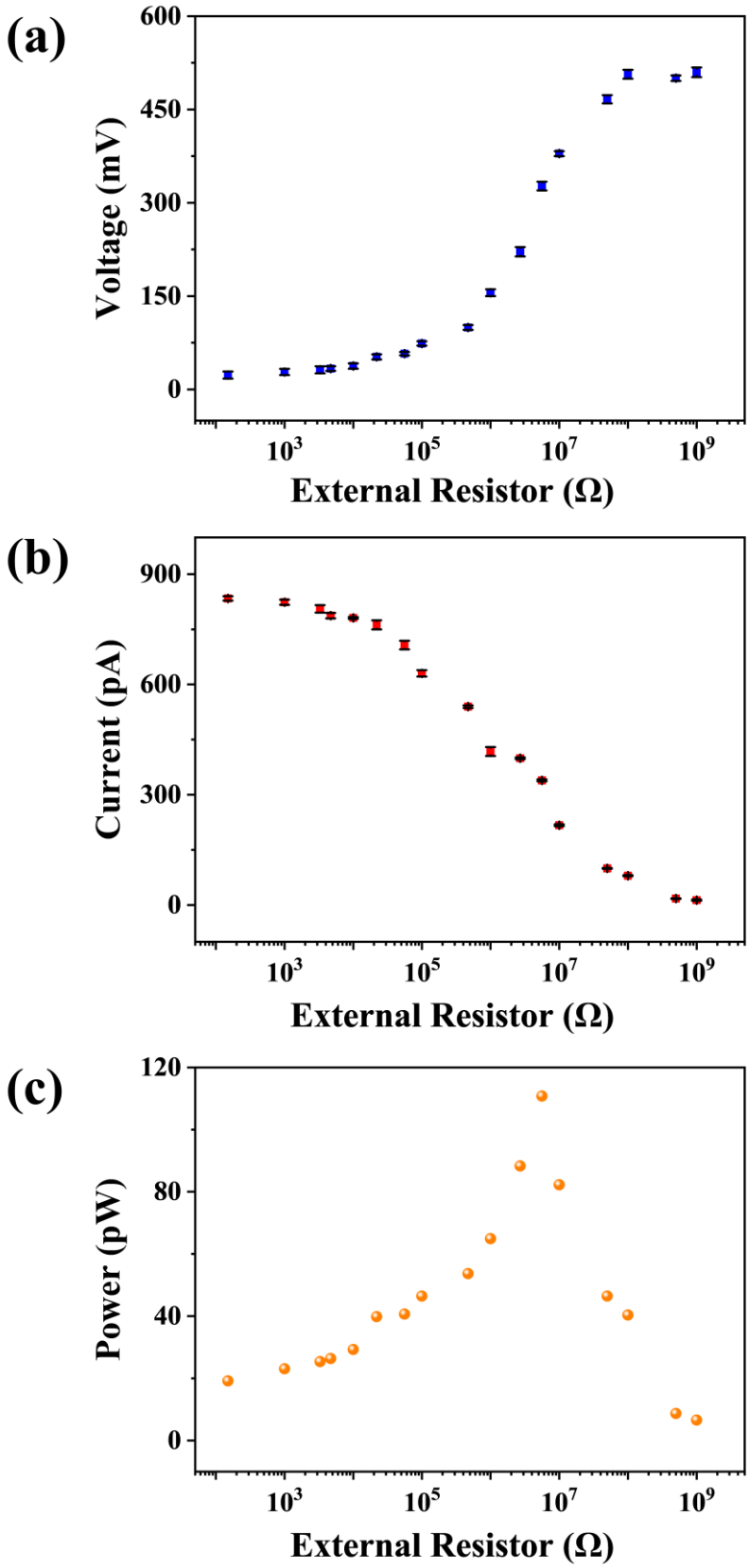

Figure 5.11 Output performance under different external load resistance. (a) Open-circuit voltages. (b) Short-circuit currents. (c) Output powers.

The multi-atomic structure and the surface functional groups of MXene nanosheets contribute to the generation of piezoelectric polarizations under mechanical stimuli.[149, 176] Moreover, while the outer metal layers in $TiVCrMoC_3T_x$ exhibit various segregation tendencies, a distinct asymmetric interlayer atom segregation could be observed within $TiVCrMoC_3T_x$.[155] This asymmetric behavior may affect the polarization and charge separation processes in $TiVCrMoC_3T_x$, revealing its ability to generate piezoelectric charges and respond to electric fields or mechanical stimulus. Figure 5.12 illustrates the fundamental principle of converting mechanical energy into electrical energy in the MXene/PVA nanogenerator. At the initial state, the charges in the nanogenerator maintain at an equilibrium state, as shown in Figure 5.12a. As a compressive force is applied to the device as depicted in Figure 5.12b, the opposite positive and negative charges in the MXene/PVA nanogenerators will go towards the electrodes respectively in response to the mechanical stimulus, which induces polarization charges by the piezoelectric properties of the high-entropy MXene nanosheets. This charges separation leads to an electric field generation in the internal circuit and then it will be transferred as the positive output signals (self-powered output without external bias). Once the force is released, the charges flow back and the negative output signals are obtained, as shown in Figure 5.12c. Therefore, the mechanical energy could be successfully converted into electrical energy in this MXene/PVA nanogenerators device. The whole process could work without the supply of external electrical fields, which confirms the self-powered capability.

To eliminate any possible electrical influences from the PVA polymer and substrates, a pure PVA-based device was also measured under the same condition (Figure 5.13). It could be found that no induced signals were detected, indicating that the output signals of the MXene/PVA nanogenerator originate from the high-entropy MXene nanosheets. On these bases, the flexible nanogenerators based on high-entropy MXene-PVA composite demonstrated their extensive potential in self-powered energy harvesting applications.

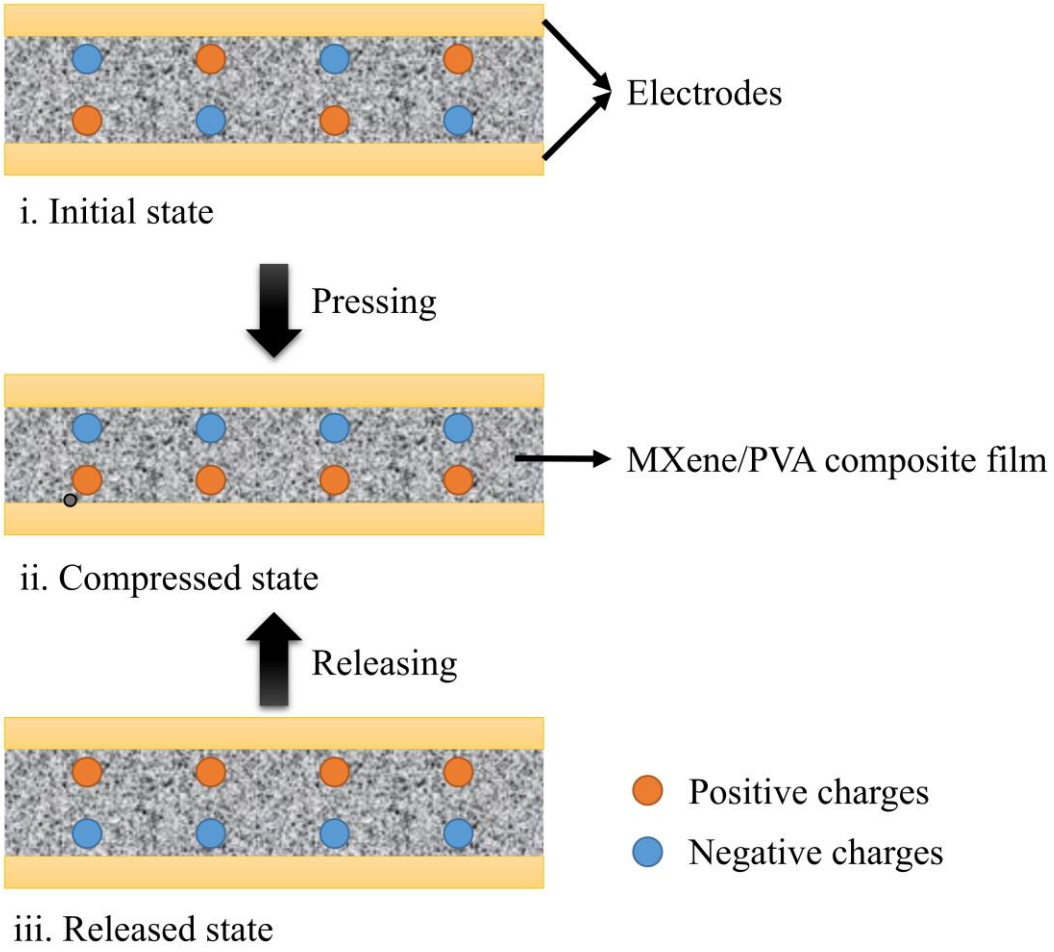

Figure 5.12 Schematic illustration for energy conversion process in MXene/PVA nanogenerators. (a) Initial state. (b) Compressed state and (c) Released state.

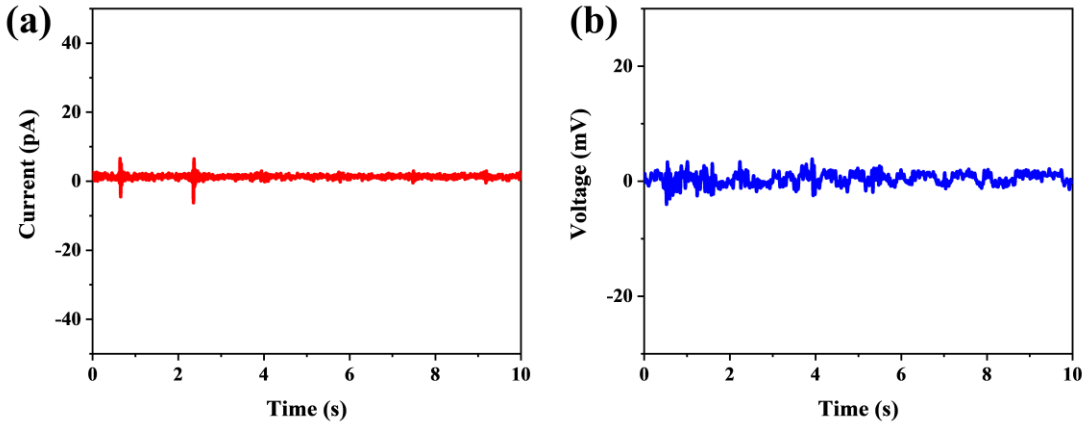

Figure 5.13 The output signals of pure PVA device. (a) Output current. (b) Output voltage.

In comparison with previously reported MXene-based PENGs (see Table 5.2),[149, 176] the MXene/PVA-PENG exhibits a higher output voltage while maintaining a comparable output current. Although the overall power density is somewhat reduced due to the relatively larger device dimensions, the significantly enhanced voltage output underscores the improved piezoelectric performance of the device. These findings demonstrate the considerable potential of the MXene/PVA-PENG for future applications in high-sensitivity self-powered sensing and mechanical energy harvesting.

Table 5.2 Comparison of output performance in MXene-based PENGs (small applied force conditions). V_{oc}: open-circuit voltage; I_{sc}: short-circuit current.

PENGs	**Applied strain/force**	**V_{oc} (mV)**	**I_{sc} (pA)**	**Power density (mW m^{-2})**
Monolayer $Ti_3C_2T_x$	1.08%	~0.27	300	6.5

PENGs	**Applied strain/force**	**V_{oc} (mV)**	**I_{sc} (pA)**	**Power density (mW m^{-2})**
MXene-PENG [149]				
Monolayer oxide $Ti_3C_2T_x$ MXene-PENG [176]	1.30%	~1.25	~1150 ± 200	~31.04
MXene/PVA-PENG (this work)	3.47 N	500	790	0.14

Leveraging its pronounced piezoelectric response, the flexible MXene/PVA-PENG was integrated onto a finger to serve as a self-powered motion-monitoring sensor. During finger bending and release (Figure 5.14a), distinct positive and negative output signals were generated in the absence of any external bias, confirming the self-powered operation of the device. The sensor delivered output currents and voltages of approximately 85 pA and 10 mV, respectively (Figure 5.14b-c), demonstrating high sensitivity and stable performance. These results underscore the promising potential of the MXene/PVA-PENG for applications in wearable electronics.

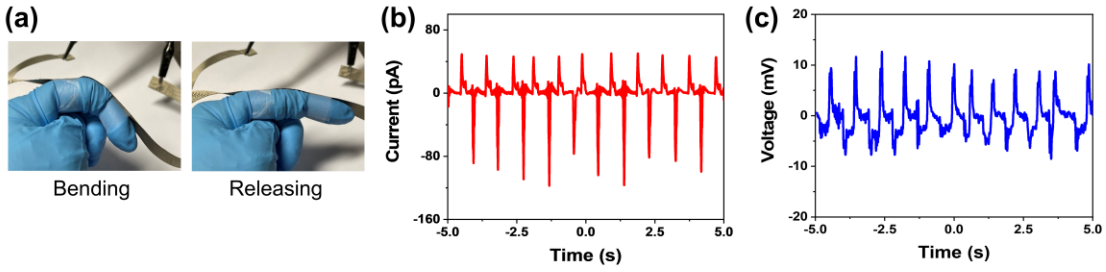

Figure 5.14 Output signals from the self-powered sensor based on the MXene–PVA

composite film. (a) Real-time monitoring of finger motion during bending and release. (b-c) Corresponding output current and voltage signals generated during finger motion.

5.5 Summary

In summary, high-entropy MXene layered nanosheets ($TiVCrMoC_3T_x$) were synthesized via the thermal-assisted electrochemical etching method and further developed into flexible nanogenerators. The as-prepared multilayered MXene nanosheets demonstrate high yield and highly crystalline structure. In the MXene/PVA flexible nanogenerators, the high and stable output signals showcase mechanical stability and practical application potential for self-powered electronics and wearable technologies.

Character 6 Conclusion and future prospects

6.1 Conclusion

Since the discovery of graphene, the layered materials have emerged as the promising candidates for flexible electronics by virtue of their ultrathin nature, desirable electrical and mechanical properties, and attractive biocompatibility. The smooth and flat surface of these layered materials offers advantages such as uniformity, enhanced electrical properties, ease of integration, improved electromechanical properties, and enhanced adhesion capabilities. This surface quality ensures consistent material properties, improved conductivity, and seamless integration into devices. Accordingly, the reliable and scalable synthesis strategies of layered nanosheets are highly desired for research investigation and practical applications. In this thesis, layered SnSe nanosheets grown by vapor transport deposition and high-entropy MXene synthesized by thermal-assisted electrochemical etching method are proposed to develop advanced flexible nanogenerators. The details of this thesis are summarized as follows.

Firstly, the SnSe nanosheets are synthesized via vapor transport deposition by carefully tailoring various growth conditions, including the precursors, growth temperature, growth time, carrier gas and substrate distance. The obtained SnSe nanosheets demonstrate uniform morphology, single-crystalline nature and non-centrosymmetric structure, suggesting the great potentials for advanced electronics and

electromechanical coupling devices. The intrinsic in-plane piezoelectricity of layered SnSe nanosheets is confirmed by PFM results, showing a layer-dependent characteristic in piezoresponse. The enhanced piezoresponse of SnSe nanosheets attributes to the unique puckered C_{2v} symmetry and less carrier scattering in the smooth surface. The effective piezoelectric coefficient in 10 nm SnSe nanosheet (d_{11} = ~ 45.82 pm/V) surpassed those in most investigated TMDs with odd-even effects, allowing for practical flexible-nanogenerator applications. Besides, the carrier mobility of SnSe nanosheets in the field-effect-gating device reach up to 19.35 $cm^2 V^{-1} s^{-1}$, highlighting the robust electrical properties of SnSe.

On these basis, flexible piezoelectric nanogenerators based on SnSe nanosheets are fabricated and demonstrate distinct piezotronic effect under mechanical stimuli. The output signals of SnSe-based flexible nanogenerators reach 270 mV in voltage and 297 pA in current at 1.03% strain, with a maximum power density of 538 mW m^{-2} and a conversion efficiency of 9.3 %, which reveals the strong piezoresponse and outstanding electromechanical properties of VTD-grown SnSe nanosheets. Besides, the stable working of the SnSe-based flexible nanogenerators further confirms the high stability and mechanical properties of SnSe. In addition to energy harvesting, the SnSe-based flexible nanogenerators were used for human-motion monitoring, suggesting the capability for smart wearable electronics and healthcare applications.

Lastly, high-entropy MXene $TiVCrMoC_3T_x$ nanosheets are prepared by thermal-assisted electrochemical etching technique. This HF-free etching method enables

scalable and high yield synthesis of MXene nanosheets, which demonstrates smooth surface texture in layered structure and high biocompatibility for practical applications. The layered MXene nanosheets are further developed into flexible nanogenerators based on a composite structure with PVA in a self-assembly path directly. The hydrogen bonding is formed between the functional groups of layered MXene nanosheets and the hydroxyl of PVA, which enables the flexibility and compatibility of the composite film. The output voltage and current of MXene/PVA flexible nanogenerators could achieve 500 mV and 790 pA respectively, which originates from the high piezoresponse of high-entropy MXene and the complexity enhancement of the composite film. In addition, the MXene/PVA flexible nanogenerators could also realize long-term working, showing promising in practical applications for wearable and bio-implantable electronics.

6.2 Future prospects

While the initial research on layered materials primarily focused on mechanically exfoliated nanosheets, the limitations of this method, such as low yield and poor controllability, have hindered their practical applications. In contrast, vapor transport deposition stands out as a promising avenue for producing high-quality and large-area layered nanosheets, aligning well with the demands of the current electronic industry. However, despite the promise of this technique, challenges persist in achieving the controlled growth of atomically thin layered materials, which underscores the need for continued research to upgrade the synthesis processes for producing high-quality, single-crystalline layered materials at scale, with a particular focus on in-situ growth of

vertical and lateral heterostructures to unlock novel physical properties. Furthermore, SnSe is a p-type semiconductor with several outstanding properties, including strong anisotropy, small electron mass and broadband absorption, promising for novel anisotropic and broadband optoelectric devices.

High-entropy MXene nanosheets exhibit remarkable thermal stability, corrosion resistance, and tunable electronic properties, making them promising candidates for a wide range of applications. Their high surface area and tailored surface chemistry provide opportunities for applications in energy storage, catalysis, sensors, and more. Their functional groups not only enhance reactivity but also allow for tunability of conductivity, band gaps, and optical responses, essential for optimizing performance in electronic and photonic devices. Moreover, the high entropy concept is also appropriate for other layered materials, such as $Mo_xW_{1-x}S_{2y}Se_{2(1-y)}$, showing high tunability of novel physics.

In terms of flexible nanogenerators, the piezoelectric output of layered materials in PENGs is typically at the levels of picoamperes and milliwatts based on current research findings, primarily utilized for detecting small signals such as human motion, pulses, and water flow. Therefore, it is imperative to broaden their application scope and explore additional possibilities. They could be integrated into the multifunctional system, while the signal interference issues need to be considered for system design. Alternatively, the array configuration could be constructed for performance improvement. Furthermore, it is feasible to design applications based on the

characteristics of layered nanosheets; for instance, some layered materials exhibit anisotropy, enabling the development of detection and signal collection in multiple directions.

In conclusion, layered nanosheets hold great promise for the future of flexible electronics, offering a versatile platform for the development of next-generation multifunctional devices with enhanced performance and functionality. Continued efforts in controlled synthesis, material engineering, and diversified applications are crucial in unlocking the full potential of these layered materials in shaping the future of technology.

References

(1) Novoselov, K. S.; Geim, A. K.; Morozov, S. V.; Jiang, D.; Zhang, Y.; Dubonos, S. V.; Grigorieva, I. V.; Firsov, A. A. Electric field effect in atomically thin carbon films. *Science* **2004**, *306* (5696), 666-669.

(2) Geim, A. K.; Novoselov, K. S. The rise of graphene. *Nat. Mater.* **2007**, *6* (3), 183-191.

(3) Novoselov, K. S.; Geim, A. K.; Morozov, S. V.; Jiang, D.; Katsnelson, M. I.; Grigorieva, I. V.; Dubonos, S. V.; Firsov, A. A. Two-dimensional gas of massless Dirac fermions in graphene. *Nature* **2005**, *438* (7065), 197-200.

(4) Wallace, P. R. The band theory of graphite. *Phys. Rev.* **1947**, *71* (9), 622-634.

(5) Morozov, S. V.; Novoselov, K. S.; Katsnelson, M. I.; Schedin, F.; Elias, D. C.; Jaszczak, J. A.; Geim, A. K. Giant intrinsic carrier mobilities in graphene and its bilayer. *Phys. Rev. Lett.* **2008**, *100* (1), 016602.

(6) Balandin, A. A.; Ghosh, S.; Bao, W.; Calizo, I.; Teweldebrhan, D.; Miao, F.; Lau, C. N. Superior thermal conductivity of single-layer graphene. *Nano Lett.* **2008**, *8* (3), 902-907.

(7) Blake, P.; Hill, E. W.; Castro Neto, A. H.; Novoselov, K. S.; Jiang, D.; Yang, R.; Booth, T. J.; Geim, A. K. Making graphene visible. *Appl. Phys. Lett.* **2007**, *91* (6), 063124.

(8) Kim, K. S.; Zhao, Y.; Jang, H.; Lee, S. Y.; Kim, J. M.; Kim, K. S.; Ahn, J. H.; Kim,

P.; Choi, J. Y.; Hong, B. H. Large-scale pattern growth of graphene films for stretchable transparent electrodes. *Nature* **2009**, *457* (7230), 706-710.

(9) Nair, R. R.; Blake, P.; Grigorenko, A. N.; Novoselov, K. S.; Booth, T. J.; Stauber, T.; Peres, N. M. R.; Geim, A. K. Fine structure constant defines visual transparency of graphene. *Science* **2008**, *320* (5881), 1308-1308.

(10) Lee, C.; Wei, X.; Kysar, J. W.; Hone, J. Measurement of the elastic properties and intrinsic strength of monolayer graphene. *Science* **2008**, *321* (5887), 385-388.

(11) Mele, E. J.; Kane, C. L. Chapter 7 Low-energy electronic structure of graphene and its Dirac theory. In Carbon Nanotubes: Quantum Cylinders of Graphene, Contemporary Concepts of Condensed Matter Science, 2008; pp 171-197.

(12) Zhan, D.; Yan, J.; Lai, L.; Ni, Z.; Liu, L.; Shen, Z. Engineering the electronic structure of graphene. *Adv. Mater.* **2012**, *24* (30), 4055-4069.

(13) Cassabois, G.; Valvin, P.; Gil, B. Hexagonal boron nitride is an indirect bandgap semiconductor. *Nat. Photonics* **2016**, *10* (4), 262-266.

(14) Watanabe, K.; Taniguchi, T.; Kanda, H. Direct-bandgap properties and evidence for ultraviolet lasing of hexagonal boron nitride single crystal. *Nat. Mater.* **2004**, *3* (6), 404-409.

(15) Dean, C. R.; Young, A. F.; Meric, I.; Lee, C.; Wang, L.; Sorgenfrei, S.; Watanabe, K.; Taniguchi, T.; Kim, P.; Shepard, K. L.; et al. Boron nitride substrates for high-quality graphene electronics. *Nat. Nanotechnol.* **2010**, *5* (10), 722-726.

(16) Britnell, L.; Gorbachev, R. V.; Jalil, R.; Belle, B. D.; Schedin, F.; Mishchenko, A.;

Georgiou, T.; Katsnelson, M. I.; Eaves, L.; Morozov, S. V.; et al. Field-effect tunneling transistor based on vertical graphene heterostructures. *Science* **2012**, *335* (6071), 947-950.

(17) Chaves, A.; Azadani, J. G.; Alsalman, H.; da Costa, D. R.; Frisenda, R.; Chaves, A. J.; Song, S. H.; Kim, Y. D.; He, D.; Zhou, J.; et al. Bandgap engineering of two-dimensional semiconductor materials. *npj 2D Mater. Appl.* **2020**, *4* (1).

(18) Tran, V.; Soklaski, R.; Liang, Y.; Yang, L. Layer-controlled band gap and anisotropic excitons in few-layer black phosphorus. *Phys. Rev. B* **2014**, *89* (23), 235319.

(19) Qiao, J.; Kong, X.; Hu, Z. X.; Yang, F.; Ji, W. High-mobility transport anisotropy and linear dichroism in few-layer black phosphorus. *Nat. Commun.* **2014**, *5*, 4475.

(20) Wang, X.; Jones, A. M.; Seyler, K. L.; Tran, V.; Jia, Y.; Zhao, H.; Wang, H.; Yang, L.; Xu, X.; Xia, F. Highly anisotropic and robust excitons in monolayer black phosphorus. *Nat. Nanotechnol.* **2015**, *10* (6), 517-521.

(21) Abate, Y.; Akinwande, D.; Gamage, S.; Wang, H.; Snure, M.; Poudel, N.; Cronin, S. B. Recent progress on stability and passivation of black phosphorus. *Adv. Mater.* **2018**, e1704749.

(22) Zhang, S.; Xie, M.; Li, F.; Yan, Z.; Li, Y.; Kan, E.; Liu, W.; Chen, Z.; Zeng, H. Semiconducting group 15 Monolayers: A broad range of band gaps and high carrier mobilities. *Angew. Chem. Int. Ed. Engl.* **2016**, *55* (5), 1666-1669.

(23) Manzeli, S.; Ovchinnikov, D.; Pasquier, D.; Yazyev, O. V.; Kis, A. 2D transition metal dichalcogenides. *Nat. Rev. Mater.* **2017**, *2* (8), 1-15.

(24) Chhowalla, M.; Shin, H. S.; Eda, G.; Li, L. J.; Loh, K. P.; Zhang, H. The chemistry of two-dimensional layered transition metal dichalcogenide nanosheets. *Nat. Chem.* **2013**, *5* (4), 263-275.

(25) Splendiani, A.; Sun, L.; Zhang, Y.; Li, T.; Kim, J.; Chim, C. Y.; Galli, G.; Wang, F. Emerging photoluminescence in monolayer MoS_2. *Nano Lett.* **2010**, *10* (4), 1271-1275.

(26) Hill, H. M.; Rigosi, A. F.; Rim, K. T.; Flynn, G. W.; Heinz, T. F. Band alignment in MoS_2/WS_2 transition metal dichalcogenide heterostructures probed by scanning tunneling microscopy and spectroscopy. *Nano Lett.* **2016**, *16* (8), 4831-4837.

(27) VahidMohammadi, A.; Rosen, J.; Gogotsi, Y. The world of two-dimensional carbides and nitrides (MXenes). *Science* **2021**, *372* (6547), eabf1581.

(28) Naguib, M.; Halim, J.; Lu, J.; Cook, K. M.; Hultman, L.; Gogotsi, Y.; Barsoum, M. W. New two-dimensional niobium and vanadium carbides as promising materials for Li-ion batteries. *J. Am. Chem. Soc.* **2013**, *135* (43), 15966-15969.

(29) Anasori, B.; Lukatskaya, M. R.; Gogotsi, Y. 2D metal carbides and nitrides (MXenes) for energy storage. *Nat. Rev. Mater.* **2017**, *2* (2), 16098.

(30) Gao, G.; O'Mullane, A. P.; Du, A. 2D MXenes: A new family of promising catalysts for the hydrogen evolution reaction. *ACS Catal.* **2016**, *7* (1), 494-500.

(31) Ma, C.; Ma, M. G.; Si, C.; Ji, X. X.; Wan, P. Flexible MXene-based composites for wearable devices. *Adv. Funct. Mater.* **2021**, *31* (22), 2009524.

(32) Xu, K.; Yin, L.; Huang, Y.; Shifa, T. A.; Chu, J.; Wang, F.; Cheng, R.; Wang, Z.; He, J. Synthesis, properties and applications of 2D layered M(III)X(VI) (M = Ga, In; X

= S, Se, Te) materials. *Nanoscale* **2016**, *8* (38), 16802-16818.

(33) Cai, H.; Gu, Y.; Lin, Y.-C.; Yu, Y.; Geohegan, D. B.; Xiao, K. Synthesis and emerging properties of 2D layered III–VI metal chalcogenides. *Appl. Phys. Rev.* **2019**, *6* (4).

(34) Zheng, C.; Yu, L.; Zhu, L.; Collins, J. L.; Kim, D.; Lou, Y.; Xu, C.; Li, M.; Wei, Z.; Zhang, Y.; et al. Room temperature in-plane ferroelectricity in van der Waals In_2Se_3. *Sci. Adv.* **2018**, *4* (7), eaar7720.

(35) Han, W.; Zheng, X.; Yang, K.; Tsang, C. S.; Zheng, F.; Wong, L. W.; Lai, K. H.; Yang, T.; Wei, Q.; Li, M.; et al. Phase-controllable large-area two-dimensional In_2Se_3 and ferroelectric heterophase junction. *Nat. Nanotechnol.* **2023**, *18* (1), 55-63.

(36) Brotons-Gisbert, M.; Andres-Penares, D.; Suh, J.; Hidalgo, F.; Abargues, R.; Rodriguez-Canto, P. J.; Segura, A.; Cros, A.; Tobias, G.; Canadell, E.; et al. Nanotexturing to enhance photoluminescent response of atomically thin indium selenide with highly tunable band gap. *Nano Lett.* **2016**, *16* (5), 3221-3229.

(37) Srour, J.; Badawi, M.; El Haj Hassan, F.; Postnikov, A. Comparative study of structural and electronic properties of GaSe and InSe polytypes. *J. Chem. Phys.* **2018**, *149* (5), 054106.

(38) Burton, L. A.; Walsh, A. Band alignment in SnS thin-film solar cells: Possible origin of the low conversion efficiency. *Appl. Phys. Lett.* **2013**, *102* (13), 132111.

(39) Suh, J.; Park, T. E.; Lin, D. Y.; Fu, D.; Park, J.; Jung, H. J.; Chen, Y.; Ko, C.; Jang, C.; Sun, Y.; et al. Doping against the native propensity of MoS_2: Degenerate hole doping

by cation substitution. *Nano Lett.* **2014**, *14* (12), 6976-6982.

(40) Chuang, S.; Battaglia, C.; Azcatl, A.; McDonnell, S.; Kang, J. S.; Yin, X.; Tosun, M.; Kapadia, R.; Fang, H.; Wallace, R. M.; et al. MoS_2 P-type transistors and diodes enabled by high work function MoO_x contacts. *Nano Lett.* **2014**, *14* (3), 1337-1342.

(41) Zhou, X.; Zhang, Q.; Gan, L.; Li, H.; Xiong, J.; Zhai, T. Booming development of group IV-VI semiconductors: Fresh blood of 2D family. *Adv Sci (Weinh)* **2016**, *3* (12), 1600177.

(42) Fei, R.; Li, W.; Li, J.; Yang, L. Giant piezoelectricity of monolayer group IV monochalcogenides: SnSe, SnS, GeSe, and GeS. *Appl. Phys. Lett.* **2015**, *107* (17), 173104.

(43) Shi, G.; Kioupakis, E. Anisotropic spin transport and strong visible-light absorbance in few-layer SnSe and GeSe. *Nano Lett.* **2015**, *15* (10), 6926-6931.

(44) Zhu, H.; Wang, Y.; Xiao, J.; Liu, M.; Xiong, S.; Wong, Z. J.; Ye, Z.; Ye, Y.; Yin, X.; Zhang, X. Observation of piezoelectricity in free-standing monolayer MoS_2. *Nat. Nanotechnol.* **2015**, *10* (2), 151-155.

(45) Ong, M. T.; Duerloo, K.-A. N.; Reed, E. J. The effect of hydrogen and fluorine coadsorption on the piezoelectric properties of graphene. *J. Phys. Chem. C* **2013**, *117* (7), 3615-3620.

(46) Blonsky, M. N.; Zhuang, H. L.; Singh, A. K.; Hennig, R. G. Ab Initio prediction of piezoelectricity in two-dimensional materials. *ACS Nano* **2015**, *9* (10), 9885-9891.

(47) Duerloo, K.-A. N.; Ong, M. T.; Reed, E. J. Intrinsic piezoelectricity in two-

dimensional materials. *J. Phys. Chem. Lett.* **2012**, *3* (19), 2871-2876.

(48) Alyörük, M. M.; Aierken, Y.; Çakır, D.; Peeters, F. M.; Sevik, C. Promising piezoelectric performance of single layer transition-metal dichalcogenides and dioxides. *J. Phys. Chem. C* **2015**, *119* (40), 23231-23237.

(49) Wang, Y. W.; Liu, S.; Zeng, B. W.; Huang, H.; Xiao, J.; Li, J. B.; Long, M. Q.; Xiao, S.; Yu, X. F.; Gao, Y. L.; et al. Ultraviolet saturable absorption and ultrafast carrier dynamics in ultrasmall black phosphorus quantum dots. *Nanoscale* **2017**, *9* (14), 4683-4690.

(50) Guo, Y.; Zhou, S.; Bai, Y.; Zhao, J. Enhanced piezoelectric effect in Janus group-III chalcogenide monolayers. *Appl. Phys. Lett.* **2017**, *110* (16).

(51) Hu, T.; Dong, J. Two new phases of monolayer group-IV monochalcogenides and their piezoelectric properties. *Phys. Chem. Chem. Phys.* **2016**, *18* (47), 32514-32520.

(52) Hinchet, R.; Khan, U.; Falconi, C.; Kim, S.-W. Piezoelectric properties in two-dimensional materials: Simulations and experiments. *Mater. Today* **2018**, *21* (6), 611-630.

(53) Wu, W.; Wang, L.; Li, Y.; Zhang, F.; Lin, L.; Niu, S.; Chenet, D.; Zhang, X.; Hao, Y.; Heinz, T. F.; et al. Piezoelectricity of single-atomic-layer MoS_2 for energy conversion and piezotronics. *Nature* **2014**, *514* (7523), 470-474.

(54) Han, S. A.; Kim, T. H.; Kim, S. K.; Lee, K. H.; Park, H. J.; Lee, J. H.; Kim, S. W. Point-defect-passivated MoS_2 nanosheet-based high performance piezoelectric nanogenerator. *Adv. Mater.* **2018**, *30* (21), 1800342.

(55) Lin, P.; Zhu, L. P.; Li, D.; Wang, Z. L. Defect repair for enhanced piezo-phototronic MoS_2 flexible phototransistors. *J Mater Chem C* **2019**, *7* (46), 14731-14738.

(56) Dai, M. J.; Zheng, W.; Zhang, X.; Wang, S. M.; Lin, J. H.; Li, K.; Hu, Y. X.; Sun, E. W.; Qiu, Y. F.; Fu, Y. Q.; et al. Enhanced piezoelectric effect derived from grain boundary in MoS_2 monolayers. *Nano Lett.* **2020**, *20* (1), 201-207.

(57) Lee, J. H.; Park, J. Y.; Cho, E. B.; Kim, T. Y.; Han, S. A.; Kim, T. H.; Liu, Y.; Kim, S. K.; Roh, C. J.; Yoon, H. J.; et al. Reliable piezoelectricity in bilayer WSe_2 for piezoelectric nanogenerators. *Adv. Mater.* **2017**, *29* (29), 1606667.

(58) Hallil, H.; Cai, W.; Zhang, K.; Yu, P.; Liu, S.; Xu, R.; Zhu, C.; Xiong, Q.; Liu, Z.; Zhang, Q. Strong piezoelectricity in 3R-MoS_2 flakes. *Adv. Electron. Mater.* **2022**, 2101131.

(59) Lu, A. Y.; Zhu, H.; Xiao, J.; Chuu, C. P.; Han, Y.; Chiu, M. H.; Cheng, C. C.; Yang, C. W.; Wei, K. H.; Yang, Y.; et al. Janus monolayers of transition metal dichalcogenides. *Nat. Nanotechnol.* **2017**, *12* (8), 744-749.

(60) Kim, J.; Lee, E.; Bhoyate, S.; An, T. K. Stable and high-performance piezoelectric sensor via CVD grown WS_2. *Nanotechnology* **2020**, *31* (44), 445203.

(61) Yu, J. B.; Liu, C. X. Piezoelectricity and topological quantum phase transitions in two-dimensional spin-orbit coupled crystals with time-reversal symmetry. *Nat. Commun.* **2020**, *11* (1), 2290.

(62) Yu, S.; Rice, Q.; Tabibi, B.; Li, Q.; Seo, F. J. Piezoelectricity in WSe-/MoS_2-heterostructure atomic layers. *Nanoscale* **2018**, *10* (26), 12472-12479.

(63) Kang, S.; Jeon, S.; Kim, S.; Seol, D.; Yang, H.; Lee, J.; Kim, Y. Tunable out-of-plane piezoelectricity in thin-layered $MoTe_2$ by surface corrugation-mediated flexoelectricity. *ACS Appl. Mater. Interfaces* **2018**, *10* (32), 27424-27431.

(64) Kang, S.; Kim, S.; Jeon, S.; Jang, W.-S.; Seol, D.; Kim, Y.-M.; Lee, J.; Yang, H.; Kim, Y. Atomic-scale symmetry breaking for out-of-plane piezoelectricity in two-dimensional transition metal dichalcogenides. *Nano Energy* **2019**, *58*, 57-62.

(65) Ong, M. T.; Reed, E. J. Engineered piezoelectricity in graphene. *ACS Nano* **2012**, *6* (2), 1387-1394.

(66) Dai, M. J.; Wang, Z. G.; Wang, F. K.; Qiu, Y. F.; Zhang, J.; Xu, C. Y.; Zhai, T. Y.; Cao, W. W.; Fu, Y. Q.; Jia, D. C.; et al. Two-dimensional van der Waals materials with aligned in-pane polarization and large piezoelectric effect for self-powered piezoelectric sensors. *Nano Lett.* **2019**, *19* (8), 5410-5416.

(67) Yang, P. K.; Chou, S. A.; Hsu, C. H.; Mathew, R. J.; Chiang, K. H.; Yang, J. Y.; Chen, Y. T. Tin disulfide piezoelectric nanogenerators for biomechanical energy harvesting and intelligent human-robot interface applications. *Nano Energy* **2020**, *75*.

(68) Khan, H.; Mahmood, N.; Zavabeti, A.; Elbourne, A.; Rahman, M. A.; Zhang, B. Y.; Krishnamurthi, V.; Atkin, P.; Ghasemian, M. B.; Yang, J.; et al. Liquid metal-based synthesis of high performance monolayer SnS piezoelectric nanogenerators. *Nat. Commun.* **2020**, *11* (1), 3449.

(69) Kim, S. K.; Bhatia, R.; Kim, T. H.; Seol, D.; Kim, J. H.; Kim, H.; Seung, W.; Kim, Y.; Lee, Y. H.; Kim, S. W. Directional dependent piezoelectric effect in CVD grown

monolayer MoS_2 for flexible piezoelectric nanogenerators. *Nano Energy* **2016**, *22*, 483-489.

(70) Zhou, Y.-X.; Lin, Y.-T.; Huang, S.-M.; Chen, G.-T.; Chen, S.-W.; Wu, H.-S.; Ni, I. C.; Pan, W.-P.; Tsai, M.-L.; Wu, C.-I.; et al. Tungsten disulfide nanosheets for piezoelectric nanogenerator and human-machine interface applications. *Nano Energy* **2022**, *97*, 107172.

(71) Li, P.; Zhang, Z. Self-powered 2D material-based pH sensor and photodetector driven by monolayer $MoSe_2$ piezoelectric nanogenerator. *ACS Appl. Mater. Interfaces* **2020**, 58132–58139.

(72) Xue, F.; Zhang, J. W.; Hu, W. J.; Hsu, W. T.; Han, A.; Leung, S. F.; Huang, J. K.; Wan, Y.; Liu, S. H.; Zhang, J. L.; et al. Multidirection piezoelectricity in mono- and multilayered hexagonal α-In_2Se_3. *ACS Nano* **2018**, *12* (5), 4976-4983.

(73) Apte, A.; Mozaffari, K.; Samghabadi, F. S.; Hachtel, J. A.; Chang, L.; Susarla, S.; Idrobo, J. C.; Moore, D. C.; Glavin, N. R.; Litvinov, D.; et al. 2D electrets of ultrathin MoO_2 with apparent piezoelectricity. *Adv. Mater.* **2020**, *32* (24), 2000006.

(74) Apte, A.; Kouser, S.; Safi Samghabadi, F.; Chang, L.; Sassi, L. M.; Litvinov, D.; Yakobson, B. I.; Puthirath, A. B.; Ajayan, P. M. Piezo-response in two-dimensional α-Tellurene films. *Mater. Today* **2020**, 40-47.

(75) Yang, S.; Liu, Y.; Wu, M.; Zhao, L.-D.; Lin, Z.; Cheng, H.-c.; Wang, Y.; Jiang, C.; Wei, S.-H.; Huang, L.; et al. Highly-anisotropic optical and electrical properties in layered SnSe. *Nano Research* **2017**, *11* (1), 554-564.

(76) Huang, Y.; Li, L.; Lin, Y.-H.; Nan, C.-W. Liquid exfoliation few-layer SnSe nanosheets with tunable band gap. *J. Phys. Chem. C* **2017**, *121* (32), 17530-17537.

(77) Das, L.; Guleria, A.; Adhikari, S. Aqueous phase one-pot green synthesis of SnSe nanosheets in a protein matrix: negligible cytotoxicity and room temperature emission in the visible region. *RSC Adv.* **2015**, *5* (75), 61390-61397.

(78) Shao, G.; Xue, X.-X.; Yang, M.; Yang, J.; Liu, X.; Lu, H.; Jiang, Y.; Jin, Y.; Yuan, Q.; Sun, J.; et al. Modulated anisotropic growth of 2D SnSe based on the difference in *a*/*b*/*c*-axis edge atomic structures. *Chem. Mater.* **2021**, *33* (11), 4231-4239.

(79) Sun, L.; Yuan, G.; Gao, L.; Yang, J.; Chhowalla, M.; Gharahcheshmeh, M. H.; Gleason, K. K.; Choi, Y. S.; Hong, B. H.; Liu, Z. Chemical vapour deposition. *Nat. Rev. Methods Primers* **2021**, *1* (1), 5.

(80) Cai, Z.; Liu, B.; Zou, X.; Cheng, H. M. Chemical vapor deposition growth and applications of two-dimensional materials and their heterostructures. *Chem. Rev.* **2018**, *118* (13), 6091-6133.

(81) Lim, K. R. G.; Shekhirev, M.; Wyatt, B. C.; Anasori, B.; Gogotsi, Y.; Seh, Z. W. Fundamentals of MXene synthesis. *Nat. Synth.* **2022**, *1* (8), 601-614.

(82) Ghidiu, M.; Lukatskaya, M. R.; Zhao, M.-Q.; Gogotsi, Y.; Barsoum, M. W. Conductive two-dimensional titanium carbide 'clay' with high volumetric capacitance. In MXenes, *Jenny Stanford Publishing*, 2023; pp 379-399.

(83) Li, T.; Yao, L.; Liu, Q.; Gu, J.; Luo, R.; Li, J.; Yan, X.; Wang, W.; Liu, P.; Chen, B.; et al. Fluorine-free synthesis of high-purity Ti_3C_2T (T = OH, O) via alkali treatment.

Angew. Chem. Int. Ed. **2018**, *57* (21), 6115-6119.

(84) Li, G.; Tan, L.; Zhang, Y.; Wu, B.; Li, L. Highly efficiently delaminated single-layered MXene nanosheets with large lateral size. *Langmuir* **2017**, *33* (36), 9000-9006.

(85) Urbankowski, P.; Anasori, B.; Makaryan, T.; Er, D.; Kota, S.; Walsh, P. L.; Zhao, M.; Shenoy, V. B.; Barsoum, M. W.; Gogotsi, Y. Synthesis of two-dimensional titanium nitride Ti_4N_3 (MXene). *Nanoscale* **2016**, *8* (22), 11385-11391.

(86) Yang, S.; Zhang, P.; Wang, F.; Ricciardulli, A. G.; Lohe, M. R.; Blom, P. W. M.; Feng, X. Fluoride-free synthesis of two-dimensional titanium carbide (MXene) using a binary aqueous system. *Angew. Chem. Int. Ed. Engl.* **2018**, *57* (47), 15491-15495.

(87) Pang, S. Y.; Wong, Y. T.; Yuan, S.; Liu, Y.; Tsang, M. K.; Yang, Z.; Huang, H.; Wong, W. T.; Hao, J. Universal strategy for HF-free facile and rapid synthesis of two-dimensional MXenes as multifunctional energy materials. *J. Am. Chem. Soc.* **2019**, *141* (24), 9610-9616.

(88) Xu, C.; Wang, L.; Liu, Z.; Chen, L.; Guo, J.; Kang, N.; Ma, X. L.; Cheng, H. M.; Ren, W. Large-area high-quality 2D ultrathin Mo_2C superconducting crystals. *Nat. Mater.* **2015**, *14* (11), 1135-1141.

(89) Ledain, O.; Woelffel, W.; Roger, J.; Vignoles, G.; Maillé, L.; Jacques, S. Reactive chemical vapour deposition of titanium carbide from H_2-$TiCl_4$ gas mixture on pyrocarbon: A comprehensive study. *Phys. Procedia* **2013**, *46*, 79-87.

(90) Hong, Y.-L.; Liu, Z.; Wang, L.; Zhou, T.; Ma, W.; Xu, C.; Feng, S.; Chen, L.; Chen, M.-L.; Sun, D.-M.; et al. Chemical vapor deposition of layered two-dimensional

$MoSi_2N_4$ materials. *Science* **2020**, *369* (6504), 670-674.

(91) Wang, D.; Zhou, C.; Filatov, A. S.; Cho, W.; Lagunas, F.; Wang, M.; Vaikuntanathan, S.; Liu, C.; Klie, R. F.; Talapin, D. V. Direct synthesis and chemical vapor deposition of 2D carbide and nitride MXenes. *Science* **2023**, *379* (6638), 1242-1247.

(92) Popp, J.; Mayerhöfer, T. Micro-Raman Spectroscopy: Theory and Application; *Walter de Gruyter GmbH & Co KG*, 2020.

(93) Bragg, W.; Thomson, J.; Friedrich, H. The diffraction of short electromagnetic waves by a crystal. *Proc. Camb. Philos. Soc.* **1913**, *17*, 43-57.

(94) Spieß, L.; Behnken, H.; Genzel, C.; Schwarzer, R.; Teichert, G. Moderne röntgenbeugung; *Springer*, 2009.

(95) Abd Mutalib, M.; Rahman, M. A.; Othman, M. H. D.; Ismail, A. F.; Jaafar, J. Chapter 9-Scanning electron microscopy (SEM) and energy-dispersive X-Ray (EDX) spectroscopy. In Membrane Characterization, Hilal, N., Ismail, A. F., Matsuura, T., Oatley-Radcliffe, D. Eds.; *Elsevier*, 2017; pp 161-179.

(96) Tanaka, N. Scanning transmission electron microscopy of nanomaterials: basics of imaging and analysis; *World Scientific*, 2014.

(97) Pletincx, S. Study of the encapsulation of healing agents for autonomous self-healing coatings. 2014.

(98) Ma, H.; Liang, J.; Hong, H.; Liu, K.; Zou, D.; Wu, M.; Liu, K. Rich information on 2D materials revealed by optical second harmonic generation. *Nanoscale* **2020**, *12*

(45), 22891-22903.

(99) Li, Y.; Rao, Y.; Mak, K. F.; You, Y.; Wang, S.; Dean, C. R.; Heinz, T. F. Probing symmetry properties of few-layer MoS_2 and h-BN by optical second-harmonic generation. *Nano Lett.* **2013**, *13* (7), 3329-3333.

(100) Aghigh, A.; Bancelin, S.; Rivard, M.; Pinsard, M.; Ibrahim, H.; Legare, F. Second harmonic generation microscopy: A powerful tool for bio-imaging. *Biophys Rev* **2023**, *15* (1), 43-70.

(101) Transmission electron microscopy. In Materials Characterization, 2008; pp 79-119.

(102) Das, P. Optical properties of low dimensional structures using cathodoluminescence in a high resolution scanning electron microscope. 2014.

(103) Cui, C.; Xue, F.; Hu, W.-J.; Li, L.-J. Two-dimensional materials with piezoelectric and ferroelectric functionalities. *npj 2D Mater. Appl.* **2018**, *2* (1), 18.

(104) Soergel, E. Piezoresponse force microscopy (PFM). *J. Phys. D: Appl. Phys.* **2011**, *44* (46), 464003.

(105) Zhang, J. X. J.; Hoshino, K. Fundamentals of nano/microfabrication and scale effect. In Molecular Sensors and Nanodevices, 2019; pp 43-111.

(106) Lee, J. S.; Choi, S. H.; Yun, S. J.; Kim, Y. I.; Boandoh, S.; Park, J.-H.; Shin, B. G.; Ko, H.; Lee, S. H.; Kim, Y.-M.; et al. Wafer-scale single-crystal hexagonal boron nitride film via self-collimated grain formation. *Science* **2018**, *362* (6416), 817-821.

(107) Tacx, J. C. J. F.; Schoffeleers, H. M.; Brands, A. G. M.; Teuwen, L. Dissolution

behavior and solution properties of polyvinylalcohol as determined by viscometry and light scattering in DMSO, ethyleneglycol and water. *Polymer* **2000**, *41* (3), 947-957.

(108) Zhao, L. D.; Lo, S. H.; Zhang, Y.; Sun, H.; Tan, G.; Uher, C.; Wolverton, C.; Dravid, V. P.; Kanatzidis, M. G. Ultralow thermal conductivity and high thermoelectric figure of merit in SnSe crystals. *Nature* **2014**, *508* (7496), 373-377.

(109) Li, C. W.; Hong, J.; May, A. F.; Bansal, D.; Chi, S.; Hong, T.; Ehlers, G.; Delaire, O. Orbitally driven giant phonon anharmonicity in SnSe. *Nat. Phys.* **2015**, *11* (12), 1063-1069.

(110) Wang, Z.; Wang, J.; Zang, Y.; Zhang, Q.; Shi, J.-A.; Jiang, T.; Gong, Y.; Song, C.-L.; Ji, S.-H.; Wang, L.-L.; et al. Molecular beam epitaxy-grown SnSe in the rock-salt structure: An artificial topological crystalline insulator material. *Adv. Mater.* **2015**, *27* (28), 4150-4154.

(111) Xu, H.; Hao, L.; Liu, H.; Dong, S.; Wu, Y.; Liu, Y.; Cao, B.; Wang, Z.; Ling, C.; Li, S.; et al. Flexible SnSe photodetectors with ultrabroad spectral response up to 10.6 μm enabled by photobolometric effect. *ACS Appl. Mater. Interfaces.* **2020**, *12* (31), 35250-35258.

(112) Li, L.; Chen, Z.; Hu, Y.; Wang, X.; Zhang, T.; Chen, W.; Wang, Q. Single-layer single-crystalline SnSe nanosheets. *J. Am. Chem. Soc.* **2013**, *135* (4), 1213-1216.

(113) Zhao, S.; Wang, H.; Zhou, Y.; Liao, L.; Jiang, Y.; Yang, X.; Chen, G.; Lin, M.; Wang, Y.; Peng, H.; et al. Controlled synthesis of single-crystal SnSe nanoplates. *Nano Research* **2015**, *8* (1), 288-295.

(114) Sharma, R. C.; Chang, Y. A. The Se−Sn (Selenium-Tin) system. *Bull. Alloy Phase Diagrams* **1986**, *7* (1), 68-72.

(115) Huang, Y.; Xu, K.; Wang, Z.; Shifa, T. A.; Wang, Q.; Wang, F.; Jiang, C.; He, J. Designing the shape evolution of $SnSe_2$ nanosheets and their optoelectronic properties. *Nanoscale* **2015**, *7* (41), 17375-17380.

(116) Chiu, M. H.; Ji, X.; Zhang, T.; Mao, N.; Luo, Y.; Shi, C.; Zheng, X.; Liu, H.; Han, Y.; Wilson, W. L.; et al. Growth of large-sized 2D ultrathin SnSe crystals with in-plane ferroelectricity. *Adv. Electron. Mater.* **2023**, 2201031.

(117) Ma, X.-H.; Cho, K.-H.; Sung, Y.-M. Growth mechanism of vertically aligned SnSe nanosheets via physical vapour deposition. *CrystEngComm* **2014**, *16* (23), 5080-5086.

(118) Liu, F.; Parajuli, P.; Rao, R.; Wei, P. C.; Karunarathne, A.; Bhattacharya, S.; Podila, R.; He, J.; Maruyama, B.; Priyadarshan, G.; et al. Phonon anharmonicity in single-crystalline SnSe. *Phys. Rev. B* **2018**, *98* (22), 224309.

(119) Vaughn, D. D.; In, S.-I.; Schaak, R. E. A Precursor-limited nanoparticle coalescence pathway for tuning the thickness of laterally-uniform colloidal nanosheets: The case of SnSe. *ACS Nano* **2011**, *5* (11), 8852-8860.

(120) Hu, D.; Yao, M.; Fan, Y.; Ma, C.; Fan, M.; Liu, M. Strategies to achieve high performance piezoelectric nanogenerators. *Nano Energy* **2019**, *55*, 288-304.

(121) Curie, J.; Curie, P. Développement par compression de l'électricité polaire dans les cristaux hémièdres à faces inclinées. *Bulletin de minéralogie* **1880**, *3* (4), 90-93.

(122) Briscoe, J.; Dunn, S. Piezoelectric nanogenerators–A review of nanostructured piezoelectric energy harvesters. *Nano Energy* **2015**, *14*, 15-29.

(123) Wang, Q. H.; Kalantar-Zadeh, K.; Kis, A.; Coleman, J. N.; Strano, M. S. Electronics and optoelectronics of two-dimensional transition metal dichalcogenides. *Nat. Nanotechnol.* **2012**, *7* (11), 699-712.

(124) Li, P.; Zhang, Z.; Shen, W.; Hu, C.; Shen, W.; Zhang, D. A self-powered 2D-material sensor unit driven by a SnSe piezoelectric nanogenerator. *J. Mater. Chem. A* **2021**, *9*, 4716-4723.

(125) Alluri, N. R.; Raj, N. P. M. J.; Khandelwal, G.; Kim, S.-J. Shape-dependent in-plane piezoelectric response of SnSe nanowall/microspheres. *Nano Energy* **2021**, *88*.

(126) Zhou, J.; Lin, J.; Huang, X.; Zhou, Y.; Chen, Y.; Xia, J.; Wang, H.; Xie, Y.; Yu, H.; Lei, J.; et al. A library of atomically thin metal chalcogenides. *Nature* **2018**, *556* (7701), 355-359.

(127) Frindt, R. F. Single crystals of MoS_2 several molecular layers thick. *J. Appl. Phys.* **1966**, *37* (4), 1928-1929.

(128) Li, H.; Zhang, Q.; Yap, C. C. R.; Tay, B. K.; Edwin, T. H. T.; Olivier, A.; Baillargeat, D. From bulk to monolayer MoS_2: Evolution of Raman scattering. *Adv. Funct. Mater.* **2012**, *22* (7), 1385-1390.

(129) Kim, D. M.; Eom, C. B.; Nagarajan, V.; Ouyang, J.; Ramesh, R.; Vaithyanathan, V.; Schlom, D. G. Thickness dependence of structural and piezoelectric properties of epitaxial $Pb(Zr_{0.52}Ti_{0.48})O_3$ films on Si and $SrTiO_3$ substrates. *Appl. Phys. Lett.* **2006**,

88 (14), 142904.

(130) Liu, F.; You, L.; Seyler, K. L.; Li, X.; Yu, P.; Lin, J.; Wang, X.; Zhou, J.; Wang, H.; He, H.; et al. Room-temperature ferroelectricity in $CuInP_2S_6$ ultrathin flakes. *Nat. Commun.* **2016**, *7*, 12357.

(131) Ma, W.; Lu, J.; Wan, B.; Peng, D.; Xu, Q.; Hu, G.; Peng, Y.; Pan, C.; Wang, Z. L. Piezoelectricity in multilayer black phosphorus for piezotronics and nanogenerators. *Adv. Mater.* **2020**, *32* (7), e1905795.

(132) Wu, W.; Wang, Z. L. Piezotronics and piezo-phototronics for adaptive electronics and optoelectronics. *Nat. Rev. Mater.* **2016**, *1* (7), 1-17.

(133) Jiang, J.; Wong, C. P. Y.; Zou, J.; Li, S.; Wang, Q.; Chen, J.; Qi, D.; Wang, H.; Eda, G.; Chua, D. H. C.; et al. Two-step fabrication of single-layer rectangular SnSe flakes. *2D Mater.* **2017**, *4* (2), 021026.

(134) Jang, A. R.; Hong, S.; Hyun, C.; Yoon, S. I.; Kim, G.; Jeong, H. Y.; Shin, T. J.; Park, S. O.; Wong, K.; Kwak, S. K.; et al. Wafer-scale and wrinkle-free epitaxial growth of single-orientated multilayer hexagonal boron nitride on sapphire. *Nano Lett.* **2016**, *16* (5), 3360-3366.

(135) Ranjan, A.; Raghavan, N.; Holwill, M.; Watanabe, K.; Taniguchi, T.; Novoselov, K. S.; Pey, K. L.; O'Shea, S. J. Dielectric breakdown in dingle-crystal hexagonal boron nitride. *ACS Appl. Electron. Mater.* **2021**, *3* (8), 3547-3554.

(136) Yang, R.; Qin, Y.; Dai, L.; Wang, Z. L. Power generation with laterally packaged piezoelectric fine wires. *Nat. Nanotechnol.* **2009**, *4* (1), 34-39.

(137) Zhang, L. C.; Qin, G.; Fang, W. Z.; Cui, H. J.; Zheng, Q. R.; Yan, Q. B.; Su, G. Tinselenidene: a Two-dimensional Auxetic Material with Ultralow Lattice Thermal Conductivity and Ultrahigh Hole Mobility. *Sci Rep* **2016**, *6*, 19830.

(138) Song, H. B.; Karakurt, I.; Wei, M. S.; Liu, N.; Chu, Y.; Zhong, J. W.; Lin, L. W. Lead iodide nanosheets for piezoelectric energy conversion and strain sensing. *Nano Energy* **2018**, *49*, 7-13.

(139) Naguib, M.; Kurtoglu, M.; Presser, V.; Lu, J.; Niu, J.; Heon, M.; Hultman, L.; Gogotsi, Y.; Barsoum, M. W. Two-dimensional nanocrystals produced by exfoliation of Ti_3AlC_2. *Adv. Mater.* **2011**, *23* (37), 4248-4253.

(140) Yang, Z.; Liu, A.; Wang, C.; Liu, F.; He, J.; Li, S.; Wang, J.; You, R.; Yan, X.; Sun, P.; et al. Improvement of gas and humidity sensing properties of organ-like MXene by alkaline treatment. *ACS Sens.* **2019**, *4* (5), 1261-1269.

(141) Lukatskaya, M. R.; Mashtalir, O.; Ren, C. E.; Dall'Agnese, Y.; Rozier, P.; Taberna, P. L.; Naguib, M.; Simon, P.; Barsoum, M. W.; Gogotsi, Y. Cation intercalation and high volumetric capacitance of two-dimensional titanium carbide. *Science* **2013**, *341* (6153), 1502-1505.

(142) Han, M.; Shuck, C. E.; Rakhmanov, R.; Parchment, D.; Anasori, B.; Koo, C. M.; Friedman, G.; Gogotsi, Y. Beyond $Ti_3C_2T_x$: MXenes for electromagnetic interference shielding. *ACS Nano* **2020**, *14* (4), 5008-5016.

(143) Alhabeb, M.; Maleski, K.; Anasori, B.; Lelyukh, P.; Clark, L.; Sin, S.; Gogotsi, Y. Guidelines for synthesis and processing of two-dimensional titanium carbide ($Ti_3C_2T_x$

MXene). *Chem. Mater.* **2017**, *29* (18), 7633-7644.

(144) Halim, J.; Lukatskaya, M. R.; Cook, K. M.; Lu, J.; Smith, C. R.; Näslund, L.-Å.; May, S. J.; Hultman, L.; Gogotsi, Y.; Eklund, P.; et al. Transparent conductive two-dimensional titanium carbide epitaxial thin films. *Chem. Mater.* **2014**, *26* (7), 2374-2381.

(145) Kumar, S. Fluorine-free MXenes: Recent advances, synthesis strategies, and mechanisms. *Small* **2024**, *20* (16), 2308225.

(146) Naguib, M.; Barsoum, M. W.; Gogotsi, Y. Ten years of progress in the synthesis and development of MXenes. *Adv. Mater.* **2021**, *33* (39), 2103393.

(147) Bai, Y.; Liu, C.; Chen, T.; Li, W.; Zheng, S.; Pi, Y.; Luo, Y.; Pang, H. MXene-copper/cobalt hybrids via Lewis acidic molten salts etching for high performance symmetric supercapacitors. *Angew. Chem. Int. Ed. Engl.* **2021**, *60* (48), 25318-25322.

(148) Li, W.; Zhou, T.; Zhang, Z.; Li, L.; Lian, W.; Wang, Y.; Lu, J.; Yan, J.; Wang, H.; Wei, L.; et al. Ultrastrong MXene film induced by sequential bridging with liquid metal. *Science* **2024**, *385* (6704), 62-68.

(149) Tan, D.; Jiang, C.; Sun, N.; Huang, J.; Zhang, Z.; Zhang, Q.; Bu, J.; Bi, S.; Guo, Q.; Song, J. Piezoelectricity in monolayer MXene for nanogenerators and piezotronics. *Nano Energy* **2021**, *90*, 106528.

(150) Tan, J.; Wang, Y.; Wang, Z.; He, X.; Liu, Y.; Wang, B.; Katsnelson, M. I.; Yuan, S. Large out-of-plane piezoelectricity of oxygen functionalized MXenes for ultrathin piezoelectric cantilevers and diaphragms. *Nano Energy* **2019**, *65*, 104058.

(151) Castle, E.; Csanádi, T.; Grasso, S.; Dusza, J.; Reece, M. Processing and properties of high-entropy ultra-high temperature carbides. *Sci. Rep.* **2018**, *8* (1), 8609.

(152) Wang, K.; Chen, L.; Xu, C.; Zhang, W.; Liu, Z.; Wang, Y.; Ouyang, J.; Zhang, X.; Fu, Y.; Zhou, Y. Microstructure and mechanical properties of (TiZrNbTaMo)C high-entropy ceramic. *J. Mater. Sci. Technol.* **2020**, *39*, 99-105.

(153) Nemani, S. K.; Zhang, B.; Wyatt, B. C.; Hood, Z. D.; Manna, S.; Khaledialidusti, R.; Hong, W.; Sternberg, M. G.; Sankaranarayanan, S.; Anasori, B. High-entropy 2D carbide MXenes: $TiVNbMoC_3$ and $TiVCrMoC_3$. *ACS Nano* **2021**, *15* (8), 12815-12825.

(154) Tan, T. L.; Jin, H. M.; Sullivan, M. B.; Anasori, B.; Gogotsi, Y. High-throughput survey of ordering configurations in MXene alloys across compositions and temperatures. *ACS Nano* **2017**, *11* (5), 4407-4418.

(155) Leong, Z.; Jin, H.; Wong, Z. M.; Nemani, K.; Anasori, B.; Tan, T. L. Elucidating the chemical order and disorder in high-entropy MXenes: A high-throughput survey of the atomic configurations in $TiVNbMoC_3$ and $TiVCrMoC_3$. *Chem. Mater.* **2022**, *34* (20), 9062-9071.

(156) Pang, S.-Y.; Io, W.-F.; Wong, L.-W.; Zhao, J.; Hao, J. Direct and *in situ* growth of 1T′ MoS_2 and 1T $MoSe_2$ on electrochemically synthesized MXene as an electrocatalyst for hydrogen generation. *Nano Energy* **2022**, *103*, 107835.

(157) Naguib, M.; Halim, J.; Lu, J.; Cook, K. M.; Hultman, L.; Gogotsi, Y.; Barsoum, M. W. New two-dimensional niobium and vanadium carbides as promising materials for Li-ion batteries. *J. Am. Chem. Soc.* **2013**, *135* (43), 15966-15969.

(158) Lim, K. R. G.; Shekhirev, M.; Wyatt, B. C.; Anasori, B.; Gogotsi, Y.; Seh, Z. W. Fundamentals of MXene synthesis. *Nature Synthesis* **2022**, *1* (8), 601-614.

(159) Li, Y.; Shao, H.; Lin, Z.; Lu, J.; Liu, L.; Duployer, B.; Persson, P. O. A.; Eklund, P.; Hultman, L.; Li, M.; et al. A general Lewis acidic etching route for preparing MXenes with enhanced electrochemical performance in non-aqueous electrolyte. *Nat. Mater.* **2020**, *19* (8), 894-899.

(160) Li, M.; Lu, J.; Luo, K.; Li, Y.; Chang, K.; Chen, K.; Zhou, J.; Rosen, J.; Hultman, L.; Eklund, P.; et al. Element replacement approach by reaction with Lewis acidic molten salts to synthesize nanolaminated MAX phases and MXenes. *J. Am. Chem. Soc.* **2019**, *141* (11), 4730-4737.

(161) Zhang, T.; Shevchuk, K.; Wang, R. J.; Kim, H.; Hourani, J.; Gogotsi, Y. Delamination of chlorine-terminated MXene produced using molten salt etching. *Chem. Mater.* **2024**, *36* (4), 1998-2006.

(162) Chen, J.; Jin, Q.; Li, Y.; Shao, H.; Liu, P.; Liu, Y.; Taberna, P.-L.; Huang, Q.; Lin, Z.; Simon, P. Molten salt-shielded synthesis (MS^3) of MXenes in air. *Energy Environ. Mater.* **2023**, *6* (2), e12328.

(163) Shen, M.; Jiang, W.; Liang, K.; Zhao, S.; Tang, R.; Zhang, L.; Wang, J. Q. One-pot green process to synthesize MXene with controllable surface terminations using molten salts. *Angew. Chem.* **2021**, *133* (52), 27219-27224.

(164) Cheng, L.; Chen, Q.; Li, J.; Liu, H. Boosting the photocatalytic activity of $CdLa_2S_4$ for hydrogen production using Ti_3C_2 MXene as a co-catalyst. *Appl. Catal. B:*

Environ. **2020**, *267*, 118379.

(165) Cao, S.; Shen, B.; Tong, T.; Fu, J.; Yu, J. 2D/2D heterojunction of ultrathin MXene/Bi_2WO_6 nanosheets for improved photocatalytic CO_2 reduction. *Adv. Funct. Mater.* **2018**, *28* (21), 1800136.

(166) Spanier, J. E.; Gupta, S.; Amer, M.; Barsoum, M. W. Vibrational behavior of the $M_{n+1}AX_n$ phases from first-order Raman scattering(M=Ti, V, Cr, A = Si, X = C, N). *Phys. Rev. B* **2005**, *71* (1), 012103.

(167) Lai, S.; Jeon, J.; Jang, S. K.; Xu, J.; Choi, Y. J.; Park, J. H.; Hwang, E.; Lee, S. Surface group modification and carrier transport properties of layered transition metal carbides (Ti_2CT_x, T: -OH, -F and -O). *Nanoscale* **2015**, *7* (46), 19390–19396.

(168) Dixit, P.; Maiti, T. A facile pot synthesis of (Ti_3AlC_2) MAX phase and its derived MXene ($Ti_3C_2T_x$). *Ceram. Int.* **2022**, *48* (24), 36156-36165.

(169) Liu, F.; Zhou, A.; Chen, J.; Zhang, H.; Cao, J.; Wang, L.; Hu, Q. Preparation and methane adsorption of two-dimensional carbide Ti_2C. *Adsorption* **2016**, *22* (7), 915-922.

(170) Ferrari, A. C.; Robertson, J. Raman spectroscopy of amorphous, nanostructured, diamond–like carbon, and nanodiamond. *Philos. Transact. A Math. Phys. Eng. Sci.* **2004**, *362* (1824), 2477-2512.

(171) Yang, F.; Li, J.; Long, Y.; Zhang, Z.; Wang, L.; Sui, J.; Dong, Y.; Wang, Y.; Taylor, R.; Ni, D.; et al. Wafer-scale heterostructured piezoelectric bio-organic thin films. *Science* **2021**, *373* (6552), 337-342.

(172) Zhao, L.; Wang, L.; Zheng, Y.; Zhao, S.; Wei, W.; Zhang, D.; Fu, X.; Jiang, K.; Shen, G.; Han, W. Highly-stable polymer-crosslinked 2D MXene-based flexible biocompatible electronic skins for in vivo biomonitoring. *Nano Energy* **2021**, *84*, 105921.

(173) Xie, Y.; Jiang, W.; Fu, T.; Liu, J.; Zhang, Z.; Wang, S. Achieving high energy density and low loss in PVDF/BST nanodielectrics with enhanced structural homogeneity. *ACS Appl. Mater. Interfaces* **2018**, *10* (34), 29038-29047.

(174) Wan, Y.-J.; Li, X.-M.; Zhu, P.-L.; Sun, R.; Wong, C.-P.; Liao, W.-H. Lightweight, flexible MXene/polymer film with simultaneously excellent mechanical property and high-performance electromagnetic interference shielding. *Composites Part A: Applied Science and Manufacturing* **2020**, *130*, 105764.

(175) Mirkhani, S. A.; Shayesteh Zeraati, A.; Aliabadian, E.; Naguib, M.; Sundararaj, U. High dielectric constant and low dielectric loss via Poly(vinyl alcohol)/$Ti_3C_2T_x$ MXene nanocomposites. *ACS Appl Mater Interfaces* **2019**, *11* (20), 18599-18608.

(176) Jiang, C.; Zeng, L.; Tan, D.; Yan, P.; Sun, N.; Guo, Q.; Zhang, Z.; Tao, Z.; Fang, C.; Ji, R.; et al. Piezoelectric behavior of single-layer oxidized-MXene for nanogenerators and piezotronics. *Nano Energy* **2023**, *114*, 108670.

(177) Tan, D.; Sun, N.; Chen, L.; Bu, J.; Jiang, C. Piezoelectricity in monolayer and multilayer $Ti_3C_2T_x$ MXenes: Implications for piezoelectric devices. *ACS Appl. Nano Mater.* **2022**, *5* (1), 1034-1046.

(178) Li, X.; Qiu, J.; Cui, H.; Chen, X.; Yu, J.; Zheng, K. Machine learning accelerated

discovery of functional MXenes with giant piezoelectric coefficients. *ACS Appl. Mater. Interfaces* **2024**, *16* (10), 12731-12743.

(179) Yang, B.; Liu, Y.; Lan, S.; Dou, L.; Nan, C.-W.; Lin, Y.-H. High-entropy design for dielectric materials: Status, challenges, and beyond. *J. Appl. Phys.* **2023**, *133* (11), 110904.

(180) Wu, J.; Ma, X.; Zhou, D.; Qi, H.; Zhang, R.; Huo, C.; Chen, L.; Li, H.; Deng, S.; Fan, L.; et al. High-entropy high-temperature high-piezoelectricity ceramics. *Adv. Mater.* **2025**, *37* (17), 2419134.

(181) Chen, Y.; Tian, Z.; Wang, X.; Ran, N.; Wang, C.; Cui, A.; Lu, H.; Zhang, M.; Xue, Z.; Mei, Y.; et al. 2D transition metal dichalcogenide with increased entropy for piezoelectric electronics. *Adv. Mater.* **2022**, e2201630.

(182) Deng, Q.; Zhou, F.; Qin, B.; Feng, Y.; Xu, Z. Eco-friendly poly(vinyl alcohol)/delaminated V_2C MXene high-*k* nanocomposites with low dielectric loss enabled by moderate polarization and charge density at the interface. *Ceram. Int.* **2020**, *46* (17), 27326-27335.

(183) Io, W. F.; Wong, M.-C.; Pang, S.-Y.; Zhao, Y.; Ding, R.; Guo, F.; Hao, J. Strong piezoelectric response in layered $CuInP_2S_6$ nanosheets for piezoelectric nanogenerators. *Nano Energy* **2022**, *99*, 107371.